UNIVERSITÀ
DEGLI STUDI
FIRENZE

DOTTORATO DI RICERCA IN FISICA E ASTRONOMIA

CICLO XXXII

COORDINATORE Prof. Raffaello D'Alessandro

Realization of a beat-note optical lattice for interferometry with Bose-Einstein condensates

Settore scientifico-disciplinare: FIS/03 Fisica della materia

Dottorando:
Leonardo Masi

Tutor:
Prof. Marco Fattori

Coordinatore:
Prof. Raffaello d'Alessandro

Anni 2016/2019

Some people want it to happen, some wish it would happen, and others make it happen.

Michael Jordan

Contents

Chapter 1

Introduction

Atom interferometry [1] is one of the most common techniques in the scientific community used to provide precision measurements of the gravitational force. It exploits the wave-like nature of particles and their sensitivity to the gravitational field. Like in optical interferometry, matter waves are first splitted in two separated paths and then recombined, in a sort of double slit experiment. Depending on the difference in the phase accumulated along the two paths, the interference pattern at the output can provide information about forces and fields that the wave have experienced during the interrogation time.
Some of the most sensitive and precise measurements of gravity have been performed with devices that are based on free falling atomic samples [2]. This type of sensors are exploited for a lot of different applications, such as the precise determination of fundamental constants [3, 4], the test of the equivalence principle [5, 6], and the detection of gravitationl waves.
In these interferometers laser cooled atomic samples are splitted and then recombined exploiting two-photon transitions. At the end of the sequence, the interferometric phase scales like $\phi \propto \Delta k \cdot s$, where Δk is the two photon momentum and $s = (F/2m)t^2$ the space traveled by the atom due to the external force.
Since the interferometric precision scales linearly with the momentum transfer and quadratically with the interrogation time, in the last decade a lot of efforts in the scientific community have been focused in the engineering of new experimental schemes to enhance these two quantities. In order to increase the interrogation time, atomic fouintains several meters high have been exploited [6] and for the future there are some projects that aim to bring atom interferometry in space [7]. Other experiments have been trying to enhance the momentum trasfert Δk using high order Raman transitions [8] or multiple Bragg diffraction [9].
However, the size of the sensors and the finite interrogation time still pose limitations to the sensitivity and the spatial resolution. Bose-Einstein condensates trapped in optical or magnetic trap offer instead the possibility to create very compact platforms. A Bose-Einstein condensate represents the matter analogue of a coherent laser because it shows a macroscopic coherence length [10]. In this framework, the goal of our experiments is to

study Bose-Einstein condensates optically trapped in a double-well potential with tunable interatomic interactions. The double-well scheme represents the ideal configuration for the realization of a Mach-Zender interferometry with trapped BECs [11]. The main limitation in experiments that use condensed clouds is the interaction induced decoherence, that limits the interrogation time up to tens of ms [11]. We have already demonstrated [12, 13] that the properly tuning of the interaction strength to negligible values by means of Feshbach resonances can help to overcome this limitation.
For interferometric applications, the small sizes of the system can allow precision measurements of forces on micrometric scales and it can be exploited for fundamental studies like the investigation of Casimir effects [14] near surfaces or deviations of the gravitational law at short distances. Moreover, the geometry of the system together with the capability to tune the inter-atomic interaction provide a versatile platform for the investigation of many-body phenomena, like the collapse and revival of the coherence between two interacting condensate [15] or the Josephson effect [13, 16, 17, 18] in bosonic systems. Finally, this system allows the creation and the control of quantum entangled states splitting adiabatically a condensate in presence of interactions [19]. The production of quantum entangled states is extremely important in the contest of quantum interferometry for the operation of interferometric sensors with sub shot noise sensitivity [20, 21, 22].
In previous experiments [13, 18] we create an array of double well potentials, i.e. an optical superlattice, exploiting two couples of laser beams crossed at a small angle and forming optical lattices with a large spacing. A large lattice constant is required to load a macroscopic number of atoms in a single well. However, this configuration was affected by uncotrollable mechanical noise, that led to a fast loss of coherence. Indeed, smaller is the angle and larger is the sensitivity of the lattice spacing to its fluctuactions. A more reliable configuration is the one that exploits retro-reflected beams by a single mirror, where the position of the minima of the potential depends only on the relative frequency of the lasers and the vibrational noise of the retro-reflecting mirror. With the current technologies, it is possible, for example, to stabilize the frequency below the Hz level with an ultra-stable cavity or a frequency comb and the vibration of the mirror can be reduced with anti-vibrational platforms. In this configuration the lattice spacing is fixed to $\lambda/2$, with λ the wavelength of the radiation. The insufficient number of laser sources with λ larger than 1 μm makes really difficult to realize large spacing optical lattices with this scheme.
In this thesis I report the realization of a large spacing optical lattice making use of an innovative technique that exploits the beating note between two lattices with slightly different wavelengths. The resulting potential is characterized by two modulations, one fast and one slow, relative to the sum and the difference of the starting. For not too high optical intensity, it is the slower one that provides the potential felt by the atoms with a large periodicity. We refer to this particular geometry of the potential as a "beat-note" lattice (BL). In the configuration that we have developed we use two wavelengths of 1064 nm and 1013 nm that allow to create a lattice with an effective periodicity of 10 μm, but

exploiting retro-reflected beams.
In order to prove the complete equivalence between a beat note lattice and a large spacing single wavelength optical lattice we study the tunneling dynamics between neighbouring sites in presence of an external force. Starting from a single site, we observe the coherent evolution of the in-situ populations. The same kind of measurement has already been performed with a single atom in a standard 1/2 μm spacing optical lattice [23]. The observed dynamics exhibits a coherence up to 1 s that correponds to a sensitivity of the order of $5 \cdot 10^{-}5$ g with a spatial resolution of ten microns. We characterized experimentally the frequency and the amplitude of the oscillations for different values of the force and the results show a very good agreement with theoretical simulations.
Finally, the interferometric scheme based on Bloch oscillations in a large spacing optical lattice can be exploited to measure weak force in the same way it has been already exploited to measure gravity [24, 25] with high precision. The advantage of this scheme is its simplicity, because only an optical lattice and an external force are present and splitting and recombination are not needed. With a larger lattice constant, the Bloch frequency increases under the same force, enhancing the sensitivity of the sensor. The amplitude of the oscillations instead decreases to few lattice sites, providing an higher spatial resolution. To our knowledge, the sensitivity acquired in this work is the higher reported in litterature in the measurement of small forces ($<< g$) using a trapped atom interferometer. Currently, the interrogation time is mainly limited by the instability of the external force.

The thesis is organized as follows.
In Chapter 2 I present a brief overview about atoms in optical lattices, describing the theory of a single particle in a periodic potential. Then I discuss theoretically the problem of an optical lattice with a constant force that leads to Bloch oscillations. Finally, I explain our idea to realize a large spacing optical lattice exploiting the beating of two slighlty different wavelengths, investigating its properties by the help of numerical simulations.
In Chapter 3 I decribe our experimental platform for the realization of Bose-Einstein condensates with tunable interaction in the beat-note optical lattice. I start with an introduction of the main parts of the experimental setup and then I focus the attention on the new laser system that I have designed and assembled for the control of the intensity and the frequency of the lasers. In particular, I focus on the technique that we exploit to lock the two frequencies at the same optical cavity.
In Chapter 4 the main results of this work are reported. I show the characterization of the novel optical lattice and the observation of Bloch oscillations. Perfroming measurement of the on-site trapping frequencies we manage to calibrate the optical depth of the BL. After a measurement of the forces acting on the system, we observe the evolution of the population of each site in presence of an external controlled force. I compare the frequency and the amplitude of the oscillations with theoretical predictions provided by numerical simulations. Finally, I discuss some future improvements for our experimental

apparatus.
In Chapter 5 I conclude with a discussion of the results that we have obtained and the future perspectives offered by our system.

In the first part of my PhD I have participated to a different project: we have studied the behaviour of an ultracold mixture of two different internal states of potassium. In particular regimes of interaction the cloud tends to collapse but, at high density, many-body effects occur and stabilize the mixture to a fixed volume. In free space it does not collapse or expand and it behaves like a liquid droplet. Even if almost half of my PhD has been dedicated to the experimental study of quantum droplets, I have preferred to focus on the project about the novel type of optical lattice, i.e. the beat-note optical lattice. Nevertheless, in Chapter 6 I report a summary of our experimental results on quantum droplets. In particular, I show our experimental characterization of the time evolution and the equilibrium properties of quantum droplets in free space [26]. Then I describe the experimental study that we have performed on the collisional dynamics between two droplets [27] that can provide informations about the excitation spectrum and the energy scales of this new phase of matter.

Chapter 2

Theory

In this chapter I present an overview on the main theoretical tools usefull to understand the physical properties of atoms in optical lattices. First I give a brief description of the theory of a single particle in a periodic potential, introducing the concepts of energy bands and energy gaps. I derive the analytic expression of the energy spectrum in the two different approximations of weak and deap potential. Then I introduce the problem of an optical lattice with a constant force that leads to a coherent dynamics named Bloch oscillations. I describe the evolution of the momentum distibution and of the wave packet in position space, comparing the dynamics in the two coordinates for different initial sizes of the condensates by the help of numerical simulations.
In the last section I explain our idea to realize a large spacing optical lattice exploiting the beating of two wavelengths. I investigate numerically the band structure of this bichromatic lattice calculating the energy gap for different regimes and configurations.

2.1 Optical Lattices

In order to confine an ultracold atomic sample it is possible to expolit the so called AC Stark effect. When an atom is placed in a light field, the oscillating electric field of the latter induces an electric dipole moment in the atom $\vec{d} = \alpha\vec{E}$, where α is the complex polarizability. The real part of α describes the component of $\vec{d}$ oscillating in phase with $\vec{E}$ and it is responsible for the dispersive properties of the interaction. The imaginary part describes the out-of-phase component of $\vec{d}$ and it is connected with the dissipative properties.
The real part leads to a dipole potential, defined by the interaction energy of the induced dipole $\vec{d}$ interacting with the driving electric field, that in the case of a laser with a frequency ω far from the atomic resonance ω_0, can be expressed as [28]:

$$V_{dip}(\vec{r}) = \frac{1}{2\epsilon_0 c}\mathrm{Re}(\alpha)I(\vec{r}) = \frac{3\pi c^2}{2\omega_0^3}\Big(\frac{\Gamma}{\Delta}\Big)I(\vec{r}) \tag{2.1}$$

where the detuning $\Delta = \omega - \omega_0$, is much larger than the radiative linewidth Γ and $I(\vec{r})$ is the intensity profile of the beam. The dissipative effects related to the imaginary part of

α describes the absorption of photons from the incident light beam. The scattering rate of a photon is defined as:

$$\Gamma_{scatt} = \frac{1}{\hbar\epsilon_0 c}\mathrm{Im}(\alpha)I(\vec{r}) = \frac{3\pi c^2}{2\hbar\omega_0^3}\Big(\frac{\Gamma}{\Delta}\Big)^2 I(\vec{r}) \tag{2.2}$$

The expr. (2.1) shows that if $\omega < \omega_0$ the force applied on the atoms points in the direction of increasing field. Choosing the spatial profile of the beam $I(\vec{r})$ it is therefore possible to engineer the trapping potential. For example, in order to trap a Bose-Einstein condensate in a periodic potential, the most common technique is to exploit the interference pattern created by two or more overlapping laser beams.
Let us consider two plane waves with the same frequency ω superimposed with an angle θ and where amplitudes of the electric fields are E_0 and E_1. The total field is:

$$E(\vec{x}, t) = E_0 e^{i(\vec{k_1}\cdot\vec{x}-\omega t)} + E_1 e^{i(\vec{k_2}\cdot\vec{x}-\omega t+\phi)} \tag{2.3}$$

where the two wave-vectors $\vec{k}_{1,2}$ have the same modulus and differ only in the direction. The total intensity is given by the square modulus of the total field. Exploiting trigonometric relations and averaging over the terms oscillating at the optical frequency ω, it is possibile to demonstrate that in the crossing region the intensity along the x direction in given by:

$$I(x) = \frac{1}{2\epsilon_0 c}[(E_0 - E_1)^2 + 4E_0E_1\cos^2(k_L x)] \tag{2.4}$$

where the wave vector of the lattice $k_L = \pi/d$ is related to the peridocity of the standing wave by

$$d = \frac{\lambda}{2\sin(\theta/2)}. \tag{2.5}$$

Assuming $E_0 = E_1$ and exploiting the eq. (2.1), the dipole potential felt by the atoms is

$$V(x) = V_0\cos^2(k_L x) \tag{2.6}$$

where the lattice depth V_0 is proportional to the optical intensity I_0. Typically, the lattice depth is measured in units of the recoil energy $E_R = \hbar^2 k_L/2m$, that represents the main energy scales for the atoms in the optical lattice.

2.2 Non-interacting particles in a periodic potential

Let us consider a gas of non interacting particles in a one-dimensional periodic potential where its spatial profile is given by the expr. (2.4).
Since the potential is periodic, the Bloch theorem ensures that the eigenfunctions of the system can be written as the eigenfunctions of the translational operator that have the form:

$$\psi_{k,n}(x) = e^{ikr} u_{k,n}(x) \tag{2.7}$$

where the functions $u_{k,n}(x)$ have the same periodicity of the potential. The parameter k is the quasi-momentum associated to the Bloch state and the index n refers to the n-th energy band. We note that, because of the discrete invariance of the Hamiltonian under translations $x = x + nd$ (with n integer), the quasimomentum is defined modulus $2\pi/d = 2k_L = G$, that is the period of the reciprocal lattice. As a matter of fact, the periodicity for a given quasimomentum of the problem in real space induces a periodic structure also in momentum space, in which the elementary cells are the so called Brillouin zones. For each k many different solutions with different energies $E_n(k)$ exist, as shown in Fig. (2.1a). These solutions are identified with the band index n.
In order to solve the problem, the wave function of a Bloch state with quasimomentum k and the potential can be written in a Fourier series:

$$\begin{aligned} \psi_{n,k}(x) &= \sum_G c^{(n)}_{k-G} e^{i(k-G)x} \\ V(x) &= \sum_G U_G e^{iGx} \end{aligned} \tag{2.8}$$

where the Fourier coefficients U_G are related to $V(x)$ by the relation

$$U_G = \frac{1}{d} \int_0^d dx e^{-iGx} V(x) \tag{2.9}$$

Substituting the expressions (2.8) in the Schrodinger equation we find an equation for the coefficients c_{k-G} and the eigenvalues ε [29]:

$$\Big(\varepsilon - \frac{\hbar^2 (k-G)^2}{2m}\Big) c_{k-G} = \sum_{G'} U_{G'-G} c_{k-G'} \tag{2.10}$$

Each Fourier component U_G couples states whose wave vector k differs from the other only by a vector G. Expanding the potential provided in (2.4) one finds $V(x) = \frac{V_0}{2} + \frac{V_0}{4}\left(e^{i2k_L x} + e^{-i2k_L x}\right)$. Therefore, apart from the constant term, an optical lattice couples states whose wave vector differ by $2k_L$: physically, this process represents the absorption of a photon from a lattice beam with a momentun $\hbar k_L$ and the consequent stimulated emission of a photon with a momentum $-\hbar k_L$ in the other beam.

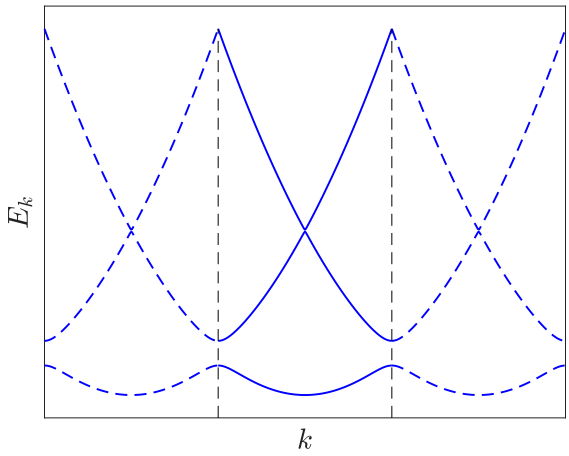

Figure 2.1: The dispersion relation of an atom in a periodic potential shows the different energy bands. For $V_0 \neq 0$, an energy gap between the first two bands appears and the bands become flatter.

2.2.1 Perturbative approach for weak potentials

In order to solve exaclty the problem (2.10) one needs to solve an infinite set of coupled equations, that can be achieved only numerically. However the spectrum $E_n(k)$ can be calculated in the two limits of weak and strong potentials.
In the case of weak potential, i.e. $|V| = V_0 << E_R$. or $s_L = V_0/E_R << 1$, it is possible to use a perturbative approach to decouple the equations and solve them analitically [29]. In this approximation we need to consider two different cases, depending on whether the two states that are coupled by the potential are degenerate or not.

Non degenerate states: a state $c_{k-\tilde{G}}$ with an unpertubed energy $E^0_{k-\tilde{G}} = \dfrac{\hbar^2(k-\tilde{G})^2}{2m}$ can be considered non-degenerate with all the other levels E^0_{k-G} if the the energy difference between them is larger than all the fourier components of the potential U_G. In this approximation it possibile to demonstrate that the general solution for the eigenvalues ε is [29]:

$$\varepsilon = E^0_{k-\tilde{G}} + \sum_{G \neq \tilde{G}} \frac{|U_{G-\tilde{G}}|^2}{E^0_{k-\tilde{G}} - E^0_{k-G}} \tag{2.11}$$

The expression shows that for non degenerate states the first correction to the unperturbed energy is of the order of $|U_G|^2$. Since for an optical lattice $G = \pm 2k_L$ and $U_{\pm 2k_L} = V_0/4$, the energy spectrum of the lowest energy band $\varepsilon(k)$ can be written as:

$$\varepsilon(k) = \frac{\hbar^2 k^2}{2m} - \sum_{G=\pm 2k_L} \frac{V_0^2}{64 E_R (1 + 2k/G)} \tag{2.12}$$

For particles with $k = 0$ the energy shift is simply:

$$\varepsilon(k=0) = -\frac{V_0^2}{64 E_R} \tag{2.13}$$

From expr. (2.12), when k approaches $\pm k_L$ the denominator diverges and the calculation is no longer correct: near the edge of the Brilluoin zone the states coupled by the potential are degenerate and one need to consider the correct perturbation theory.

Degenerate states: if there are two (or more) states such that $|E_{k-G_1} - E_{k-G_2}| \sim U$ the linear equations for the energy eigenvalues ε are:

$$(\varepsilon - E^0_{k-G_1})c_{k-G_1} = U_{G_2-G_1}c_{k-G_2} + \sum_{G_1,G_2}\left(\sum_{G\neq G_1,G_2}\frac{U_{G-G_1}U_{G_j-G}}{\varepsilon - E^0_{k-G}}\right)c_{k-G_j} \tag{2.14}$$

$$(\varepsilon - E^0_{k-G_2})c_{k-G_2} = U_{G_1-G_2}c_{k-G_1} + \sum_{G_1,G_2}\left(\sum_{G\neq G_1,G_2}\frac{U_{G-G_1}U_{G_j-G}}{\varepsilon - E^0_{k-G}}\right)c_{k-G_j} \tag{2.15}$$

Differently from the previous case, there are two contributes, one linear in U_G and the other of the order of U^2. If we consider only the first one we need to solve a simple linear system that leads to the solutions:

$$\varepsilon = \frac{(E^0_{k-G_1} + E^0_{k-G_2}) \pm \sqrt{(E^0_{k-G_1} - E^0_{k-G_2})^2 + 4|U_{G_1-G_2}|^2}}{2} \tag{2.16}$$

that in case of exactly degenerate states are reduced to

$$\varepsilon_{1,2} = E^0_{k-G} \pm |U_{G_1-G_2}| \tag{2.17}$$

The coupling with the external potential removes the degenerancy, showing an avoid crossing behaviour. The condition of exact degenerancy is satisfied for $k = k_L$, therefore the effect of the potential is the creation of a gap $\Delta E_{gap} = 2|U_{G_1-G_2}| = V_0/2$ between the first two bands, as shown in Fig. (2.1b).

2.2.2 The tight binding regime

When the recoil energy becomes much smaller than the depth of the periodic potential, the energy bands become flat and the Bloch wavefunctions turn out to be strongly modulated (see Fig. (2.2)). For increasing depth of the potential the energy bands asymptotically tend to the eigenenergies of the harmonic oscillator obtained with a parabolic approximation of the single lattice site potential.
In this regime, around each minimum we can make the following harmonic approximation

$$V(x) = V_0 cos^2(k_L x) \simeq V_0 k_L^2 x^2 = \frac{1}{2}m\omega_L^2 x^2 \tag{2.18}$$

that defines an effective trapping frequency

$$\omega_L = \sqrt{\frac{2V_0k^2}{m}} = 2\frac{\sqrt{V_0 E_R}}{\hbar} \tag{2.19}$$

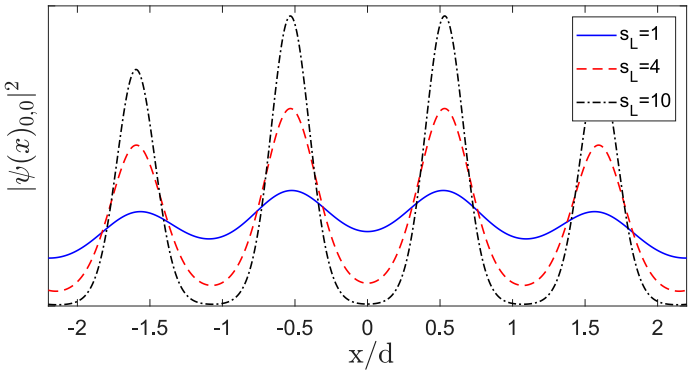

Figure 2.2: Squared modulus of the lowest band wavefunction with $k = 0$ for three different depths of the periodic potential $V_0 = E_R$ (solid), $V_0 = 4E_R$ (dotted), $V_0 = 10E_R$ (dashed). Increasing the lattice depth, the wavefunction changes from a weakly modulated plane wave to a function that is strongly localized on the lattice sites.

In this tight binding limit the wavefunction of the system can be more conveniently written as a superposition of many wavefunctions located at each lattice site x_i

$$w_n(x - x_j) = \sqrt{\frac{d}{2\pi}} \int_{BZ} dk e^{-ikx_i} \psi_{n,k}(x) \tag{2.20}$$

that are the so-called Wannier functions. For low lattice depths the Wannier functions spread over the entire lattice. In the tight binding regime the Wannier functions become strongly localized and, for increasing lattice depth, asymptotically tend to the wavefunctions describing the eigenstates of the single lattice sites.
In this limit the dispersion law of the first band can be calculated analitically as $\varepsilon(k) = -2J\cos(kd)$, where the tunneling rate J decays exponentially with the lattice depth s_L, following:

$$\frac{J}{E_R} = \frac{4}{\sqrt{\pi}} (s_L)^{3/4} e^{-2\sqrt{s_L}} \tag{2.21}$$

2.3 Bloch dynamics in presence of an external force

In this section I describe the basic concepts about the dynamics of a Bloch wavepacket in the presence of external constant force, that exhibits a dynamical coherent response named Bloch oscillations.
Let us consider a superposition of Bloch states with a mean quasimomentum k_0 and a quasimomentum spread σ_k much smaller than the width of the Brillouin zone. It follows that the spatial extent of this wavepacket is much larger than the lattice spacing, i.e. the wavefunction extends on many lattice sites. The temporal evolution of a general wave packet can be described by decomposing the initial wave function into Bloch states $\psi_{n,k}(x)$ with the corresponding amplitudes $\alpha_n(k)$. The subsequent evolution is purely a

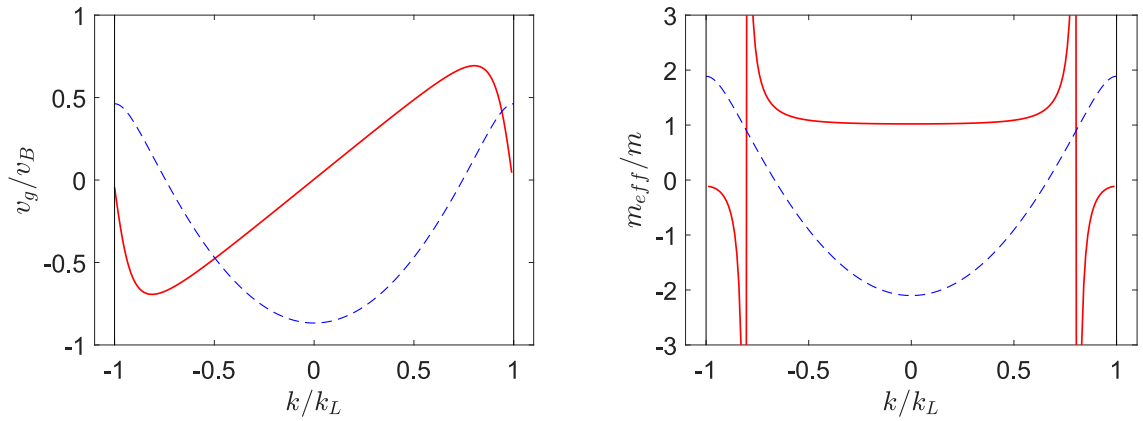

(a) (b)

Figure 2.3: Group velocity (a) and effective mass (b) in the first energy band for a particle of mass m in the optical lattice. The velocities are expressed in natural units $v_B = \hbar k_L/m$ and the effective masses in units of the real mass m.

consequence of the accumulated phase of each Bloch state $\theta_{n,k}(t) = \varepsilon_n(k)t/h$ and the wavefunction at time t is [30]:

$$\psi(x,t) = \sum_n \int_{IBZ} dk \alpha_n(k) \psi_{n,k}(x) \exp(i\theta_{n,k}(t)) \tag{2.22}$$

The assumption that only a small range of quasimomenta centered around k_0 is involved in the dynamics, allows to approximate the energy dispersion relation by a Taylor expansion:

$$\epsilon(k) = E(k_0) + (k-k_0)\frac{\partial \varepsilon(k)}{\partial k}|_{k=k_0} + \frac{(k-k_0)^2}{2}\frac{\partial^2 \varepsilon(k)}{\partial k^2}|_{k=k_0} \tag{2.23}$$

where the linear and the quadratic terms lead to the definition of the *group velocity*:

$$v_g(k_0) = \frac{1}{\hbar}\frac{\partial \varepsilon(k)}{\partial k}|_{k=k_0} \tag{2.24}$$

and the *effective mass*:

$$m_{eff}(k) = \hbar^2 \left(\frac{\partial^2 \varepsilon(k)}{\partial k^2}|_{k=k_0} \right)^{-1} \tag{2.25}$$

The bloch wave moves with a group velocity v_g in analogy of a packet of electromagnetic waves having a dispersion relation $\omega(k)$ and a velocity $\partial\omega/\partial k$. The wave packet spreads with a dispersion relation $\varepsilon(k) = \hbar^2 k^2/2m_{eff}$, where the mass of the atoms inside the lattice is replaced by the effective mass. In Fig. (2.3) I show the group velocity and the effective mass for atoms in the first band.

If now we introduce an external force F, the simplest model describing the dynamics of a Bloch wavepacket is the semiclassical model that can be derived with two important assumptions: the external force does not modify the energy spectrum, having only the effect of changing the mean position and the quasimomentum, and it is weak enough

to avoid interband transitions. When the energy gradient between the sites is large respect to the depth of the lattice, the so called *Landau-Zener tunneling* [31] occurs. In prarticular, when the quasimomentum reach the boundary of the Brillouin zone, the tunneling probability across the gap is given by [30]:

$$\Gamma = e^{-a_c/a} \quad a_c = \frac{V_0^2 d}{16\hbar^2} \tag{2.26}$$

depending on the spacing d and the depth of the potential V_0.
In the regime of weak force the dynamics of the Bloch packet can be described in a semiclassical approach by the equations of motion

$$\begin{cases} \hbar\dot{k} = F \\ \dot{x} = v_g \end{cases} \tag{2.27}$$

In presence of a constant force, the equation (2.27) leads to a linear time evolution of the quasi-momentun $k(t) = k_0 + Ft/m$. Since the quasimomentum k is defined modulus $2\pi/d$, the evolution is periodic with a Bloch period $\tau_B = h/Fd$ [32, 33] corresponding to the time required to scan a full Brillouin zone (see Fig. (2.4)a). Moreover, since the group velocity of a wave packet depends on the quasimomentum, also the position of the wave packet continuously changes. In particular, the group velocity changes sign when the central quasimomentum reaches the Brillouin zone boundary (Fig. 2.3) and the result of the force are oscillations instead of an acceleration. The latter are known as Bloch oscillations in real space [33, 34] (shown in Fig. (2.4b)
For the previous discussion we have considered the case of a Bloch wave as an initial condition and we have studied the dynamics in the momentum space, writing the wave functions as a superposition of Bloch states. It is also interesting to study a situation where only a few wells of the optical potential are populated and the spread of the momentum ditribution starts to become comparable with the width of the Brillouin zone. In this case, it is convenient to use a the notion of of the Wannier states (2.20). To simplify the analysis, we consider a tight binding model and a single-band approximation. The tight binding hamiltonian has the form [35]:

$$H_{TB} = \sum_l (E_0 + Fdl) \left|l\right\rangle \left\langle l\right| + J \sum_l (\left|l+1\right\rangle \left\langle l\right| + \left|l-1\right\rangle \left\langle l\right|) \tag{2.28}$$

where J is the hopping matrix element between neighboring sites, i.e. the tunneling rate, and $E_0 = \overline{\varepsilon(k)}$. The Hamiltonian (2.28) leads to a discrete spectrum $E_l = E_0 + Fdl$ knows as Wannier-Stark ladder [36] and the correspondent eigenfuctions $\phi_l(x)$ are knows as Wannier-Stark states. The Wannier-Stark states are localized in space with a localization length l_{WS} that depends on the force applied on the lattice: for $Fd > J$ $l_{WS} = 1$ (in units of lattice period) and $l_{WS} \sim J/Fd$ for $Fd < J$. The general solution of the Schrodinger equation can be written as a sum over the Wannier-Stark states

$$\psi(x,t) = \sum_l c_l \exp(iE_l t/\hbar)\phi_l(x) \tag{2.29}$$

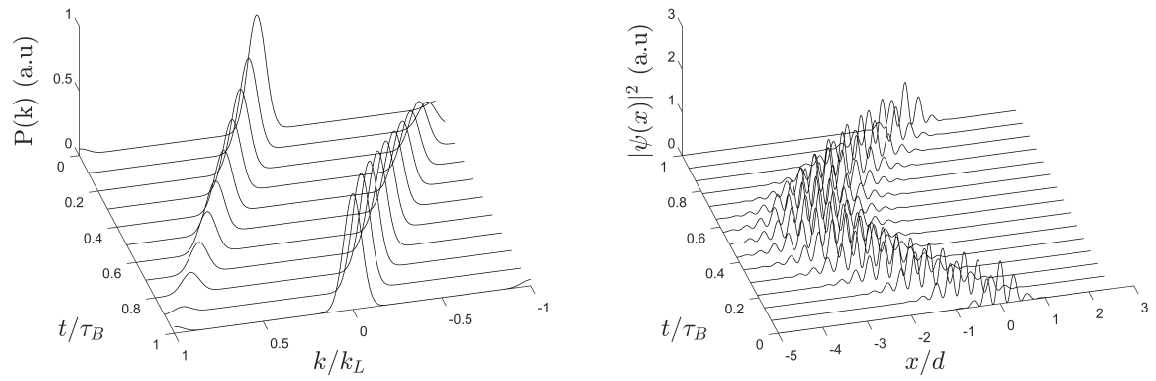

(a) (b)

Figure 2.4: Dynamics of the atomic momentum distribution $P(k)$ induced by a weak constant force F in (a) and the corrispondent spatial oscillations of the localized wave-packet in (b). The amplitude of the oscillations in real space is given by the localization length of the Wannier-Stark states $l_{WS} \sim 1/F$.

and the dynamics is represented by an oscillation of the center of mass of the wave-packet. The localization length l_{WS} defines the maximum distance where the wave-packet can move to.

2.3.1 On-site vs in far field

In the Bloch dynamics, the width of the momentum distribution depends only on the initial size of the trapped condensate. Larger is the number of occupied sites and smaller is the width of the peak respect to the Brillouin zone. In real space, the amplitude of the oscillations depends on the localization length of the Wannier-Stark functions, proportional to the tunneling J and to the inverse of the energy difference between sites Fd. This last statement is not completely true, because the amplitude depends also on the initial size of the condensate.
In order to clarify this argument, I have performed numerical simulations of the Bloch dynamics for different values of the initial trapping potential, i.e. the initial size of the condensate, and different values of the ratio between $\delta = Fd$ and J. This analysis can be usefull to understand which quantities allow to have the largest resolution observing the oscillations. The results are reported in Fig. (2.5). On the x-axis there is the initial width of the condensate espressed in terms of the lattice spacing, in the y-axis the ratio δ/J. In the case of Bloch-oscillations in far field, with the color map I report the width and the amplitude of the oscillations of the momentum distribution. In the case of the in situ dynamics, I report the amplitude of the oscillations of both the center of mass position and the width of the wave packet.
As expected, when the size of the initial condensate is smaller or comparable with d, the width of the momentum distribution is of the same order of the entire Brillouin zone. The dynamics in the momentum space disappears and this behaviour is indipendent on the

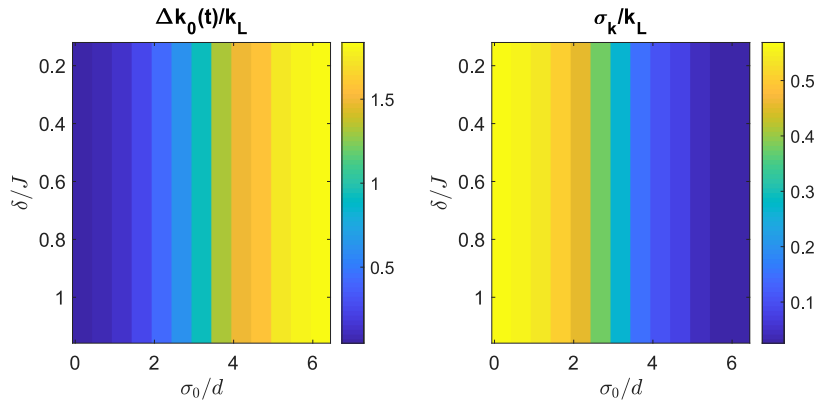

(a)

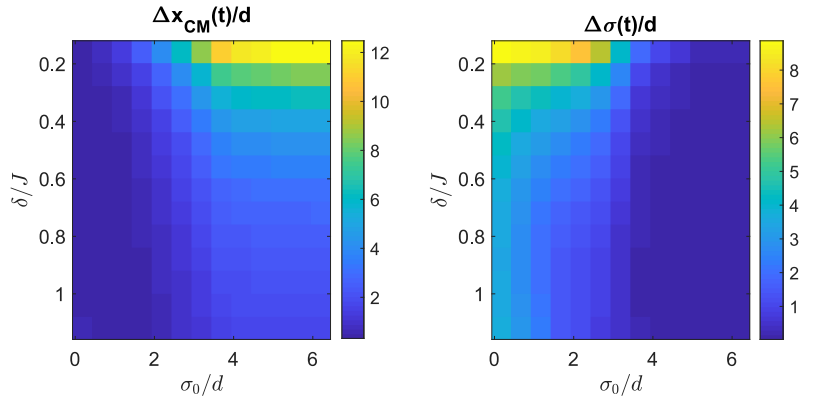

(b)

Figure 2.5: (Above) I report the amplitude of the oscillations of the quasi-momentum and of the width of the momentum distribution as a function of the ratio δ/J and the initial size of the condensate σ_0. The results show that decreasing the initial size, i.e. the number of occupied sites, the amplitude becomes smaller and the distrubution spreads over the Brillouin zone. The values don't depend on the ratio δ/J, i.e. on the appied force. (Below) Amplitude of the oscillations of the center of mass and of the width of the wave-packet in real space as a function of the same parameters. The results show that, if a small number of lattice sites is occupied, the center of mass stops to move but the coherent dynamics can be observed in the time evolution of the size.

value δ/J. At the same time, also the amplitude of the real space oscillations decreases monotonically with the decreasing inizial width. However, despite all the dynamics is frozen, it is still possible to observe coherent oscillations: the good observables is not the center of mass of the cloud but the width of the wave packet. The atoms are more confined and the large kinetic energy leads to a spread of the clouds in the neighbouring sites. The atom remains localized to a small volume and undergoes a periodic breathing motion in position space [34]. Such type of dynamics has already been observed experimentally in [23, 37, 38]. Increasing δ/J, the dynamics of both the center of mass and the width become smaller and smaller because of the reduction of the localization length of the Wannier-Stark function. In conclusion, this results show that in an optical lattice it is possible to observe a coherent dynamics even if the starting condensate occupies only one

site. This is relevant since our goal is to measure forces exploiting lattices that have a spacing of the order of ten microns, larger than the usual size of an optically trapped condensate.

2.4 An optical lattice made by a beat-note

If we consider now the superposition of two optical lattices at two different wavelengths $\lambda_{1,2}$, the resultant potential felt by the atoms is:

$$V(x) = V_1 \cos^2(k_1 x) + V_2 \cos^2(k_2 x) \tag{2.30}$$

where $k_{1,2} = 2\pi/\lambda_{1,2}$ are the two wavevectors. Using some algebra and assuming $V_1 = V_2$ the expression (2.30) can be written in the form

$$V(x) = V_0[1 + \cos((k_1 + k_2)x)\cos((k_2 - k_1)x)] \tag{2.31}$$

The resulting potential is therefore formed by two modulations, one fast and one slow, correspondent to the sum and the difference of the starting. In particular, if the two wavelengths fulfill the relation $(n+1)\lambda_2 = n\lambda_1$ (alternatively $(n+1)k_1 = nk_2$), after n oscillations the two lattices recover the same phase difference and the period of the slow modulation is $d = n\lambda_1/2$. Fig. (2.6) shows the potential in the case of $\lambda_1 \sim 1$ μm and $n = 20$. In this work I refer to this potential as a beat-note lattice (BL).
In order to understand the effect on the atoms, a simple energetic picture can be examined. Let us consider the expr. (2.31) and assume that $k_1 \sim k_2$, such that $k_1 + k_2 \approx 2k_1$. We can schematize the potential as a lattice $V(x) = V_0(x)\cos(2k_1 x)$ with a low frequency space-depending amplitude given by $V_0(x) = V_0 \cos((k_2 - k_1)x)$. As shown in section (2.2), in the perturbative regime the energy shift $\Delta\epsilon$ for an atom with $k = 0$ is described by the expression (2.13). If we extimate the spatially varying $\Delta\epsilon(x)$, that depends on the local depth of the lattice potential (centered around V_0), we get:

$$\Delta\varepsilon(x) = -\frac{V_0^2}{8E_R}\cos^2((k_2 - k_1)x) \tag{2.32}$$

where I assume $E_R = \frac{\hbar^2 k_1^2}{2m} \sim \frac{\hbar^2 k_2^2}{2m}$. The energy shift depends on the position, indicating that the beating of two lattices can be schematize as an effective potential $V_{eff}(x) = \Delta\varepsilon(x)$. In the regions where the amplitude of the modulation is higher, the energy of the state at $k = 0$ is smaller. As a consequence, the density of the ground state increases (Fig. 2.6) in these regions.

In the limit of small depth the energy gap between the first two bands is equal to half the depth, and therefore in the case of the BL it can be written as:

$$\Delta E_{gap}^{(BL)} = \frac{V_0^2}{16E_R} \tag{2.33}$$

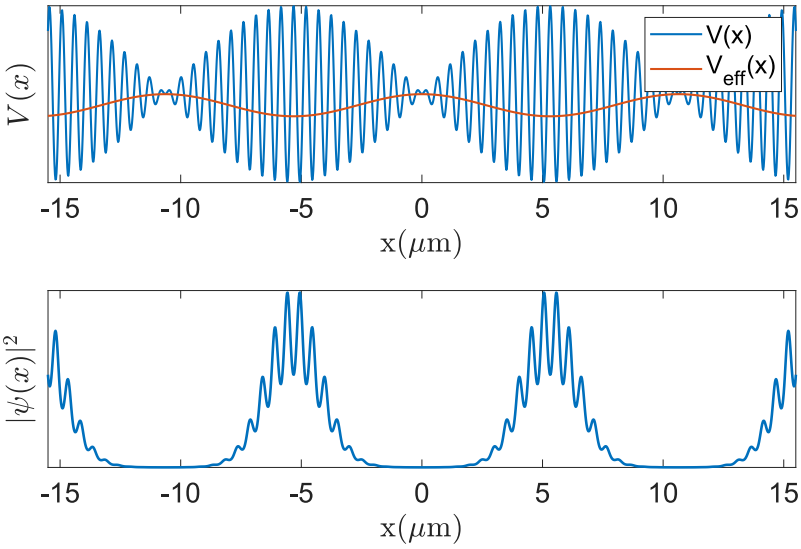

Figure 2.6: Spatial profile of the beat-note lattice potential (above) and of the density of atoms in the ground state (below). The red line represents the effective potential $V_{eff}(x)$

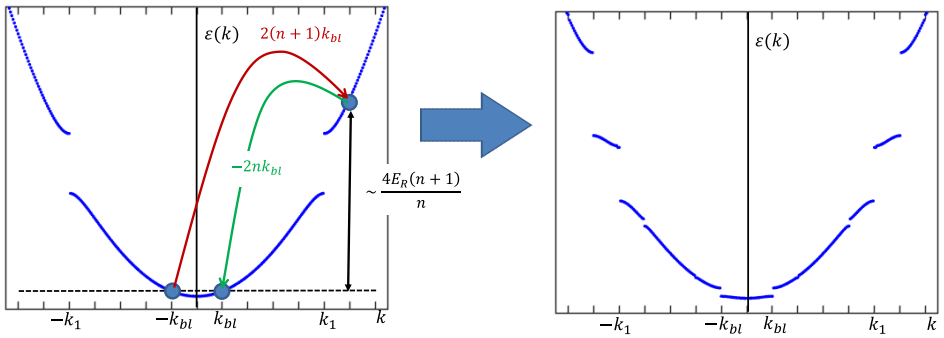

(a)

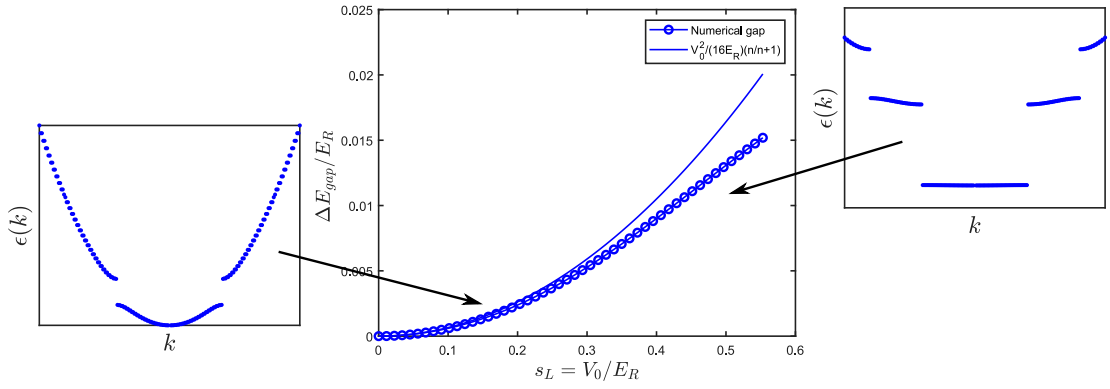

(b)

Figure 2.7: a) Schematic representation of the process that creates the additional gap inside the first band of the beat-note lattice. The first one is extactly at $k_1/2n = k_{BL}$. b) Comparison between the numerical values of the gap and the analytic result given by the expr. (2.35). The perturbative approach starts to fail when $s_L > 0.3$ because the bands become flat.

2.4.1 Exact calculation of the band structure in the momentum space

It can be interesting to derive the exact magnitude of the energy gap repeting the same calculations performed in the momentum space discuessed in section (2.2). Since the potential is periodic, the Bloch's theorem can ensure again to write the wave-function in the form (2.7) and one can exploit the same formalism. The effective periodicity of the reciprocal lattice is $k_2 - k_1 = k_1/n = 2k_{BL}$ and it defines the first Brillouin zone. If we remain in the perturbative regime where $V_1, V_2 < E_R$, the energy gap between the states at the edge of the Brillouin zone is provided by the expressions (2.14) and (2.15). The linear term in U_G does not provide any contribution because it can only couple states whose momenta differ by $2k_1$ or $2k_2$. The second order term can instead contain two different fourier components, that can belong to the two different lattices. The first one (for example U_{G_2-G}) connects the initial state with another state such that the difference is $\Delta k = 2k_2 = 2(n+1)k_{BL}$. The other one ($U_{G-G_1}$) provides a transition in the opposite direction and leads to $\Delta k' = -2k_1 = -2nk_{BL}$. The total momentum transfer is $2k_{BL}$ (for better explanation see Fig. 2.7a). Such process, that represents the absorption of two photons from a lattice and the stimulated emission of other two photons in the other lattice, is responsible to the creation of the additional gaps inside the first band (see Fig. 2.7 a).
The magnitude of the two components $|U_{G-G_{1,2}}|$ are $V_{1,2}/4$ and the detuning between the initial state and the intermediate state can be calculated as:

$$\begin{aligned}\Delta E &= \frac{\hbar^2}{2m}(k_2 - k_1)^2 - \frac{\hbar^2}{2m}(2k_2 - (k_2 - k_1))^2 = \frac{\hbar^2}{2m}(k_2 - k_1)^2 - \frac{\hbar^2}{2m}(k_2 + k_1)^2 = \\ &= -\frac{\hbar^2}{2m}(4k_1k_2) = -4\frac{\hbar^2 k_1^2}{2m}\frac{n+1}{n} = -4E_R\frac{n+1}{n}\end{aligned} \tag{2.34}$$

Colletting all the terms and considering that the processes with $\Delta k = 2k_{BL}$ and $\Delta k' = -2k_{BL}$ lead to the same result, giving an additional factor 2, the energy gap at the edge of the first Brillouin zone of a beat-note lattice in the perturbative regime is:

$$\Delta E_{gap}^{(BL)} = \frac{V_0 V_1}{16E_R\dfrac{n+1}{n}} \tag{2.35}$$

The result in (2.35) is in agreement with the relation (2.33) based on the picture of the effective potential in the limit of $n >> 1$, i.e. in the limit of infinite oscillations in a single well.
In Fig. (2.7b) I report the comparison between the analitical result in (2.35) and numerical simulations of the energy gap as a function of the lattice depth, assuming $V_1 = V_2$. For values of s_L up to 0.3 they show a good agreement. For larger depth, the system starts to enter in a tight binding regime where the bands are flat. It is possible to recover an analitic expression assuming that the picture of the effective potential is stil correct. If the atoms start to localize in the minimum of the effective potential, we can approximate

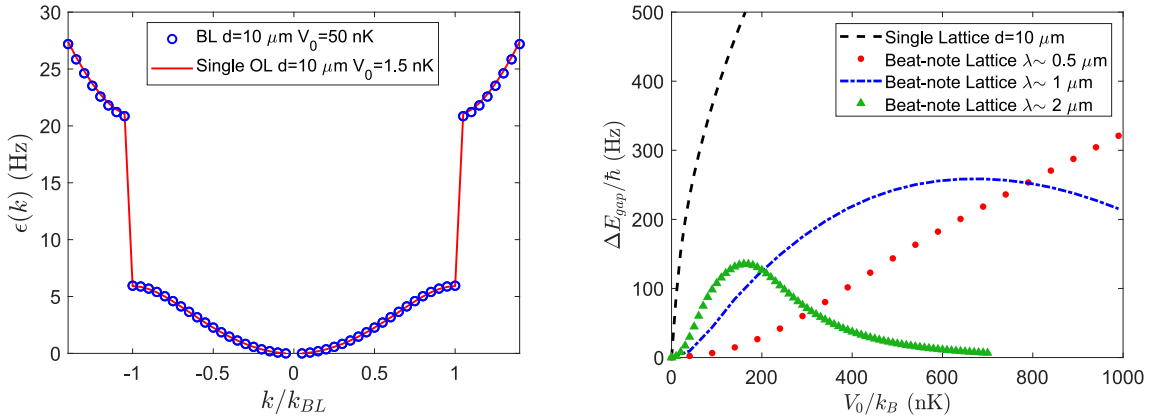

Figure 2.8: a) Comparison between the band structure of the BL and a single wavelength optical lattice with the same periodicty. In order to obtain the same structure the BL needs a larger V_0. b) Energy gap of the beat-note lattice as a function of the lattice depth for different values of the wavelengths of the primary lattice.

it as harmonic and use the expr. (2.19), that leads to:

$$\Delta E_{gap}^{(BL)} = \sqrt{\frac{V_0^2}{m4E_R}(k_2 - k_1)^2} \propto V_0 \tag{2.36}$$

2.4.2 Deep potential regime

I have shown that it is possibile to obtain an arbitrary large spacing lattice exploiting the beating of two short wavelengths. In particular, in Fig. (2.8a) I report the comparison between the energy bands of a single wavelength lattice and a BL with the same effective periodicity. In particular the comparison shows that the only requirement in order to obtain the same band structure is a larger lattice depth, i.e., a larger optical intensity. Such requirement depends on the wavelength λ of the radiation, i.e. on the spacing of the primary lattice (Fig. (2.8b)). In the limit of deep potential, the behaviour of the energy gap is no longer monotonic as a function of the lattice depth but it has a maximum achievable value. Note that, in a standard optical lattice we find instead an asimptotic scaling with $\sqrt{V_0}$

In Fig. (2.9) I compare the calculated wavefunction of the ground state of the first band and the lowest energy state of the second band for different values of $s_L = V_0/E_R$. I restrict the calculation within one site. For small values of V_0, the tunneling between the wells of the primary lattice with $d = \lambda_1/2$ is high and the wavefuctions are spread all over the sites. Increasing V_0 the tunneling becomes smaller and smaller, the particles start to localize inside the primary lattice and they stop to feel the BL as an effetive potential with $d = \pi/(k_2 - k_1)$. The tunneling amplitude of the primary lattice represents a limitation of the maximum gap achievable by the BL. As shown in Fig. (2.10) we observe two different behaviours. The gap of the BL increases with V_0 with the scaling discussed before. The tunneling amplitude instead decreases with V_0, first linearly and then exponentially.

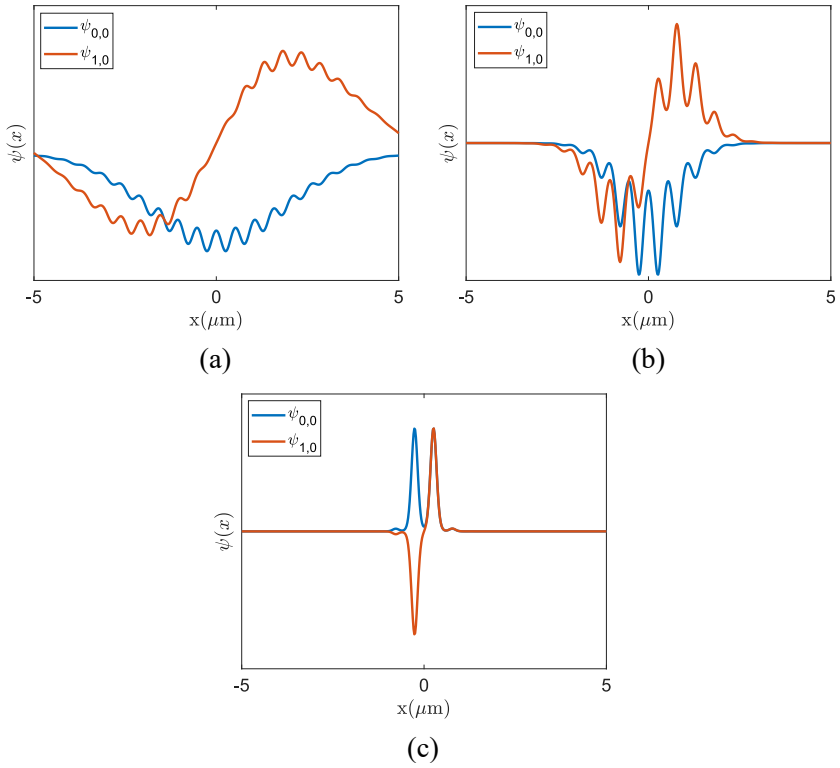

Figure 2.9: Calculated wave-functions of the ground state of the first band $\psi_{0,0}$ and of the lowest energy state of the second band $\psi_{1,0}$. The lattice depth is $s_L = 0.5$ (a), $s_L = 2$ (b), $s_L = 10$.

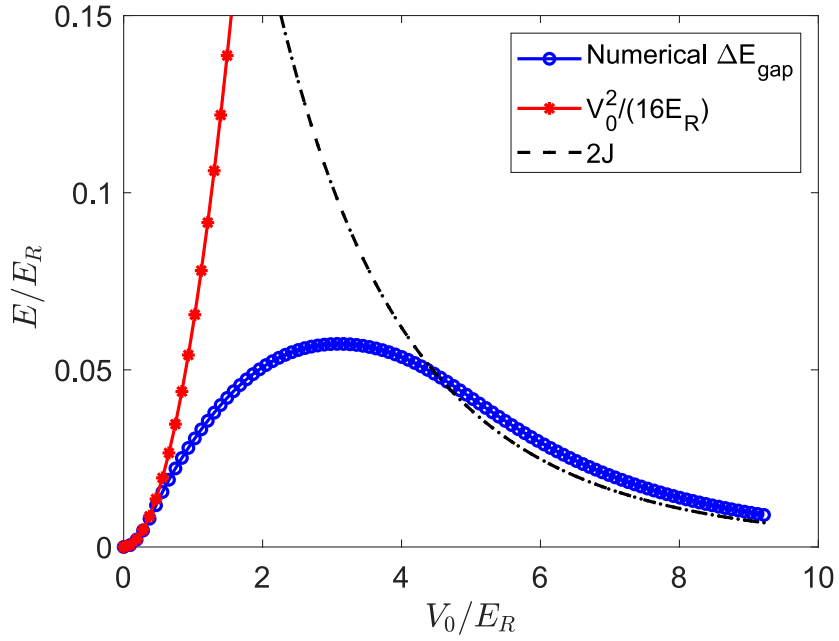

Figure 2.10: Calculated energy gap (blu-dotted line) at $k_{BL} = k_1/n$ as a function of the lattice depth. Initially, in the perturbative regimes, the energy gap (red squares) increases quadratically with the lattice depth. For larger depth, the width of the first band of the primary lattice (dashed-dotted) with $k_L = k_1$, i.e, the tunneling between neighbouring sites, decreases. The competition of these two trends creates a maximum value of the gap for the BL around $V_0/E_R \approx 3$.

The competition between this two trends leads to the appearance of a maximum. For large V_0 the energy gap and the tunneling amplitude approach each other and the gap of the BL decreases exponentially.
In conclusion, numerical simulations show that is possible to realize an effective large spacing opical lattice exploiting the beating between two short wavelengths. However, there are some limitations: the maximum achievable energy gap, usefull to avoid inter-band transitions, depends on the periodicity of the primary lattice. Shorter is the wavelength and larger is the maximum achievable gap. However, in order to obtain the same value, a larger wavelength is preferable in terms of optical intensity required.

Chapter 3

Experimental setup

In this chapter I describe our experimental platform for the realization of Bose-Einstein condensates with tunable interaction trapped in a beat-note optical lattice. In the first section I describe briefly the main parts of the experimental setup. Then I focus the attention on the new laser system used to produce and control the optical lattices. After a brief introduction to the theory of the Pound-Drevel-Hall method, I describe in more details the characteristic of the optical cavity and the electronic system that I have assembled in order to lock more than one frequency to the same reference. Finally, I show the measured frequency noise spectra and I use them to extimate the linewidth of the lasers when they are locked to the cavity.

3.1 Our experimental platform

Our experimental platform consists in three different chambers where different vacuum levels are achieved and different cooling stages are performed, as explain in [39, 40]. Once the ^{39}K sample are slowed down with a 2D+ MOT (Magnetic Optical Trap) configuration and cooled down to sub-doppler temperatures in the 3D MOT cell, the atoms are moved in the final chamber where the Bose-Einstein condensation is achieved employing evaporative cooling in a dipole optical trap. With this sysem we manage to produce with this system ensembles of up to 10^5 atoms almost purely condensed.
In particular, once the atoms reach the science chamber, they are loaded in a crossed dipole trap provided by two tightly focused red detuned infra-red beams with a wavelength around 1060 nm ("IPG" and "radial beam" in the sketch (3.1)). After the evaporative cooling the IPG is swicthed off while the radial beam remains on during all the experiments in order to provide the confinement in the radial direction. Moving the position of the crossed dipole trap respect to the lattice it is possible to decide which lattice sites are populated.
The two laser beams at 1064 nm and 1013 nm that produce the lattices come out from the same fiber, sharing the same spatial profile and the same optical path. The polarization is well defined by a Glan Taylor polarized placed at the output of the fiber. After they

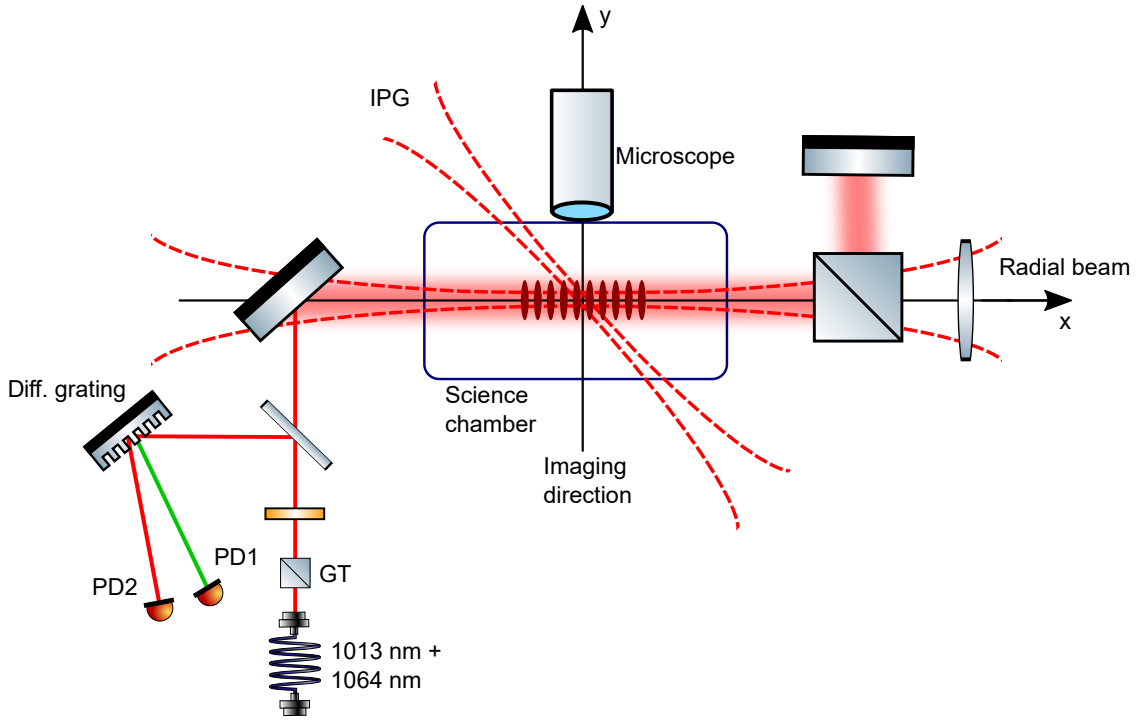

Figure 3.1: Sketch of the laser beams in the science chamber (from above). The radial beam and the lattice beams have different polarizations and they are mixed on a BS cube. After the fiber a part of the lattice beam is sent to a diffration grating in order to separate the two wavelengths and measure the intensity of each beam on two photodiodes.

have passed through the cell, they are reflected by a beam splitter-cube where they are superimposed with the radial beam, that has an opposite polarization. Finally, they are simply retro-reflected with an HRR mirror and sent back into the fiber.
At the output of the fiber, a fraction of the light is sent to a diffration grating in order to separate the two wavelengths and measure the intensity of each beam separately on two photodiodes. The two signals are sent to different PID controllers to monitor and stabilize the intensity.
Magnetic coils close to the chamber are used to tune the interaction strength among the atoms exploiting magnetic Feshbach resonances [41, 42]. Another couple of magnetic coils provide a magnetic gradient that can compensate the gravitational force.

3.1.1 Tunable interactions

One of the most important tools in our experiment is the possibility to control the interatomic scattering length via a magnetic Feshbach resonance. The two-body scattering length depends on the magnitude of the magnetic field by the relation:

$$a_s = a_{bg}\left(1 - \frac{\Delta B}{B - B_0}\right) \tag{3.1}$$

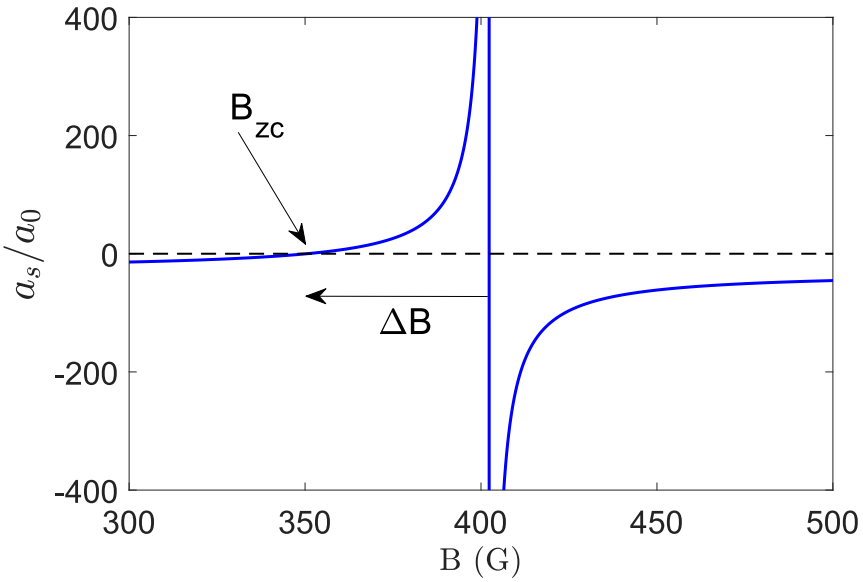

Figure 3.2: Value of the two-body scattering length in Bohr radia versus the magnitude of magnetic field in Gauss for the state $F = 1, M_F = +1$ near the resonance at 400G

In paticular, in the case of ^{39}K, there is a broad resonance for the state F=1,M_F=+1 near a value of B_0=400 G, as shown in Fig. (3.2). The width of this resonance is ΔB=50 G and the zero crossing point is at 350 G. Around this point the slope is $0.6a_0/G$, so it is possible to change the value of the scattering length very precisly.

3.1.2 Imaging technique

In order to measure the distribution of the atoms in the optical lattice potential we use an absorption imaging technique, performed shining on the atoms a laser at a resonant wavelength and an intensity I_{in}. A first image is taken recording the intensity I_{out} after the beam has crossed the cloud; a second image is taken without the atoms measuring the incident intensity.
The density of the atomic sample can be extracted integrating the Beer-Lambert law in the direction of the beam (y direction in Fig. (3.1)). The column density of the cloud can be obtained from:

$$n(x,z) = -\frac{1}{\sigma_0}\ln\left(\frac{I_{out}}{I_{in}}\right) \tag{3.2}$$

where $n(x,z)$ is the density of the atoms, I_{sat} is the saturation intensity of the atomic transition and σ_0 is the absorption cross section that can be expressed as:

$$\sigma_0 = \frac{3\lambda^2}{2\pi}\frac{1}{1+\dfrac{I}{I_{sat}}+\dfrac{4\delta^2}{\Gamma^2}} \tag{3.3}$$

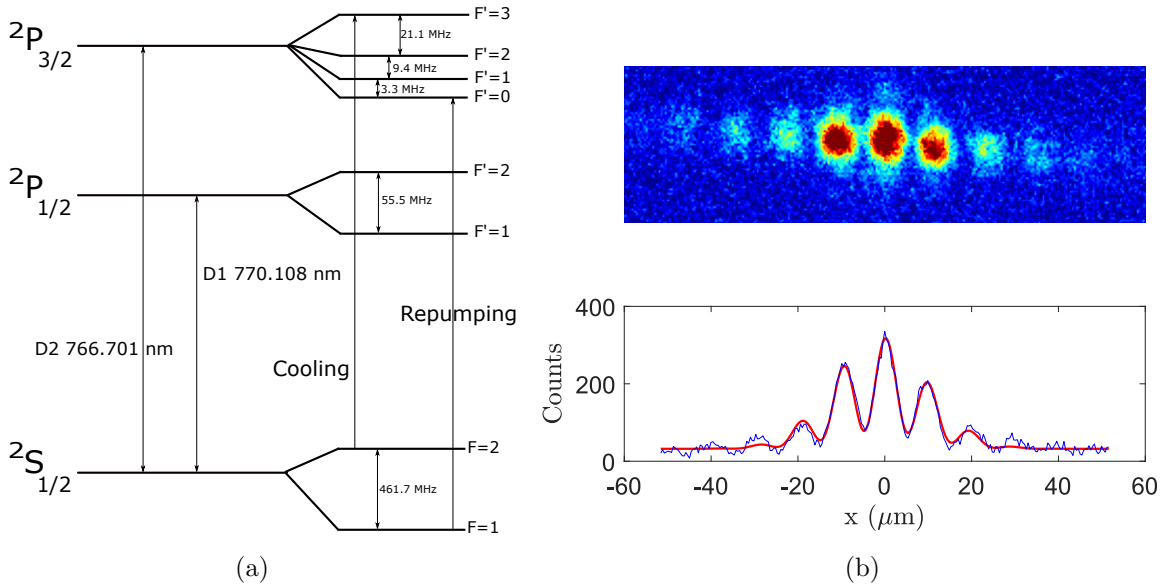

Figure 3.3: a) Optical transitions of the D1 and D2 lines of ^{39}K. b) An example of the images of the atoms in the lattice and the relative integrated density profile.

where Γ is the natural width of the atomic transition and $\delta = \omega - \omega_0$ is the detuning between the frequency of the laser and the frequency of the transition. In the case of the D2 line of the potassium (see Fig. (3.3)a) $\Gamma/2\pi \simeq 6$ MHz. The imaging procedure is performed with negligible magnetic field and using a light resonant with the transition F=2 $\rightarrow$ F'=3 (named cooling light in Fig. (3.3)a) with a polarization σ^+. The experiments are performed with atoms in the state F=1, MF=1 and they aren't in resonance with the imaging light. For this reason a pulse with the repumper light (resonant with the transition F=1 $\rightarrow F' = 2$) is first shined in order to allow a decay in the state F=2. We need this repumping laser on during the whole imaging procedure, because the difference in frequency between the two states $F' = 3$ and $F' = 2$ is only 3.6 Γ. There is a high probability that the imaging light induces the transition F=2 $\rightarrow F' = 2$ with consequent losses of atoms from the $F' = 2$ to the $F = 1$ state .
An example of an image of the atoms in the lattice taken with our high resolution imaging (of the order of 1 μm) is shown in Fig. (3.3b)

3.1.3 Laser setup for the optical lattices

Fig. (3.4) shows the laser setup for the production and the control of the frequency and intensity of the two lasers at 1064 nm and 1013 nm.
The light at 1064 nm is provided by a high power Mephisto MOPA (MM) infrared laser and the light at 1013 nm is provided by a Toptica TA PRO diode laser with a maximum power of 2 W. After optical isolators a fraction of light of both beams is sent to electro-optical modulators (EOMs) and then they are combined with a beam splitter in a fiber that brings the light to an optical cavity. I'll describe in details the characteristics of the

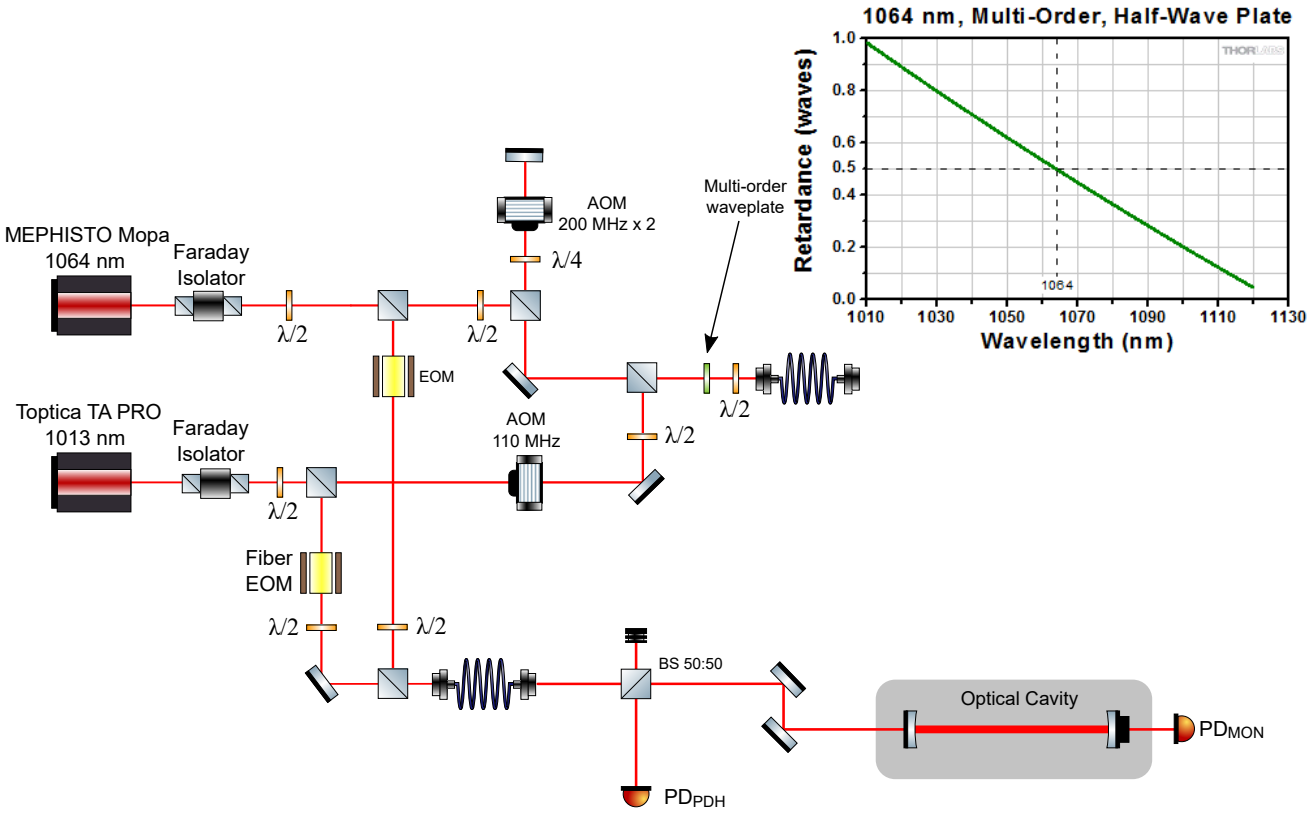

Figure 3.4: Scheme of the laser setup to produce and control the two lights at 1064 nm and 1013 nm. In the inset above I show the retardance as a function of the wavelength of the multi-order waveplate used to obtain the same polarization at the entrance of the fiber.

EOMs, the cavity and the electronic setup in section (3.2). The rest of the light is sent to acusto-optical modulators (AOMs) that, togheter with the photodiodes in Fig. (3.1) and PID controllers, allow to stabilize the intensity. For one of the two beams we use a double passage AOM in order to have the possibility to tune dinamically the frequency of the laser in a wider range of about 200 MHz. As I'll show in section (4.1), it is useful to tune the phase of the lattice during the experiment.
After the AOMs the two laser beams are mixed on a PBS and sent togheter in the same fiber that brings the light to the atoms. Before this fiber they are superimposed on a BS cube. Since the two beams have different polarizations, on the GT polarizer at the exit of the fiber it is not possible to have all the power transmitted for both the beams at the same time. In order to avoid power losses, we have decided to use a multi-order half-lambda waveplate by Thorlabs, whose retardance as a function of the wavelength is shown in the inset of Fig. (3.4). The waveplate has exactly a retardance 0.5λ for light at 1064 nm and about λ for light at 1013 nm. It means that the polarization of the first is rotated while the polarization of the second is left unchanged. In this way we can send the two beams inside the fiber with the same polarization and have all the power avaiable for both the beams.

3.2 Experimental setup for the laser frequency stabilization

The relative phase of the two lattices determines the position of the maxima and the minima of the beat note-lattice. In order to increase the stability in relative frequency fluctuactions and to narrow the linewidth of the diode laser (that has a nominal free running line width of 300 kHz) I have realized an experimental setup to lock all the frequencies to an external high finesse Fabry Perot cavity, exploiting a Pound-Drevel-Hall technique.

3.2.1 The optical cavity

The optical cavity that we currently use has been lend us by an other experiment that used light at 1064 nm (Fig. (3.5)a). It is made of INVAR (a material with a small thermal expansion coefficient) and the mirror are in a hemispherical configuration where the input mirror is nearly flat and other one is concave. Since we didn't know all the optical properties of the cavity, we have performed some tests in order to measure them directly.
Scanning the piezo that is placed behind the first mirror or scanning the frequency of the laser it is possibile to measure the optical proprieties of the cavity. The resultant spectra, measured by a photodiode that is placed behind the cavity, are shown in Fig. ((3.5 (b) and (c)). The modes of a Fabry-Perot cavity is given by the equation:

$$\nu/\nu_0 = (q+1) + \frac{m+n+1}{\pi} + \arccos\left(\left(1-\frac{d}{R_1}\right)\left(1-\frac{d}{R_2}\right)\right) \tag{3.4}$$

where the frequency seperation between neighbouring fundamental modes, called Free Spectral Range (FSR), is $\nu_0 = \frac{c}{2d}$, with d the distance between the two mirrors. When the cavity is well aligned we observe very sharp peaks that correpond to the fundamental modes. The measured FSR of the cavity is:

$$\nu_0 \simeq 1090 \quad \text{MHz} \tag{3.5}$$

that correponds to $d \simeq 13.7$ cm.
In order to measure the radius of curvature of the backside mirror, we misallign slightly the cavity and the tranverse modes appears clearly (Fig (3.5)b). Since the input mirror is flat, i.e. $R_1 = +\infty$, measuring the distance between two trasnverse modes it is possible to extimate R_2 from the expression (3.4). Substituting d and ν_0 we find $R_2 \simeq 31.4$ cm. The last quantity that defines an optical cavity is the finesse $\mathcal{F}$, defined as:

$$\mathcal{F} = \frac{FSR}{\Delta\nu_{FWHM}} \tag{3.6}$$

where $\Delta\nu_{FWHM}$ is the full width at half maximum of a cavity mode. As shown in Fig (3.5d) the FWHM of the measured modes is 230 kHz that corresponds to $\mathcal{F} \simeq 4800$.

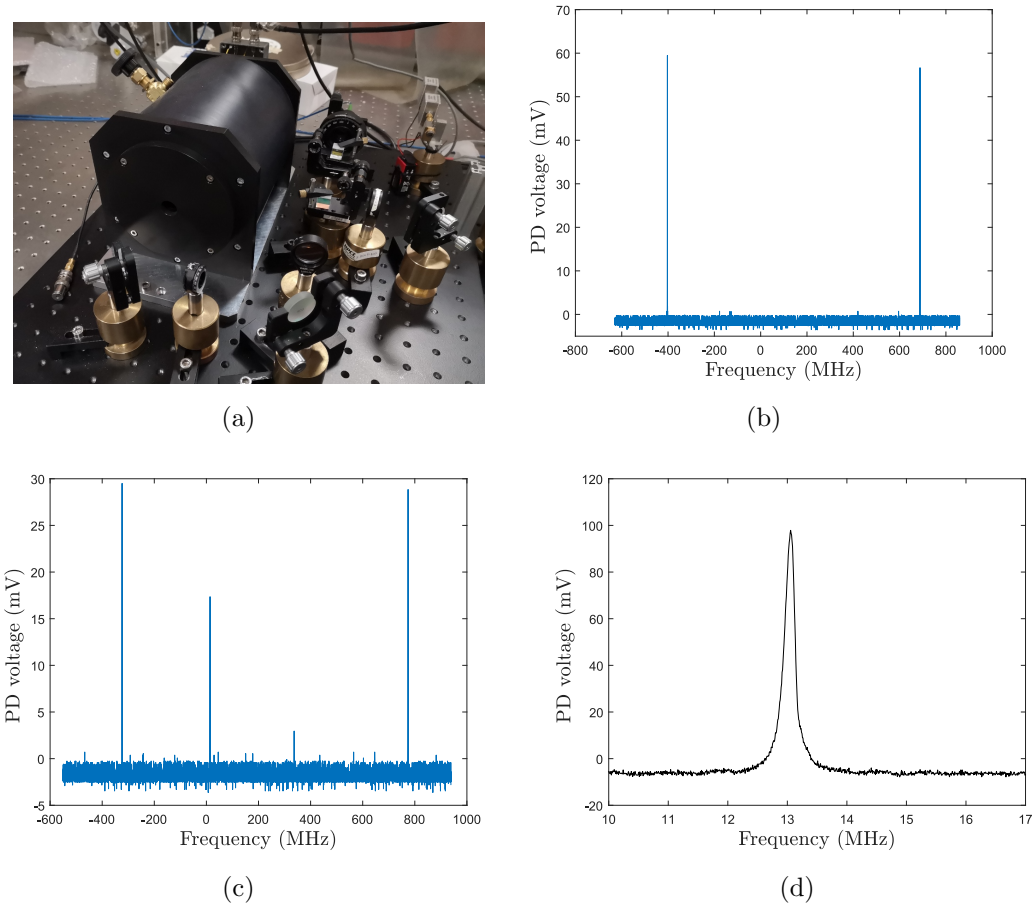

Figure 3.5: a) Picture of the cavity in the vacuum setup. b) A well aligned cavity shows very sharp fundamental modes. b) Higher order (tranversal) modes appear when it is slightly misalligned. c) Zoom of the fundamental transmission peak

3.2.2 Pound-Drevel-Hall locking scheme

If the laser frequency drifts out of resonance with the cavity, you cant tell just by looking at the reflected intensity whether the frequency needs to be increased or decreased to bring it back onto resonance. The derivative of the reflected intensity, however, is antisymmetric about resonance. If we manage to measure this derivative, we would have an error signal that we can use to lock the laser. A good way to generate this signal is to examine the light reflected from the cavity, whose spectrum is the product of the incoming spectrum and the complex amplitude reflection coefficient of the cavity $F(\omega)$, where $\omega = 2\pi\nu$. The amplitude of $F(\omega)$ goes to zero at the resonance frequencies and approaches unity between them. The width of the resonance is characterized by the finesse of the cavity. It is the phase of $F(\omega)$ that contains the information about whether the light frequency is above or below the resonance, since it has different sign in the two sides of the resonance. A measurement of the phase shift experienced by the reflected light can be used to generate an error signal for locking the laser to the cavity resonance.
One standard technique to create such error signal is the Pound-Drever-Hall [43, 44]

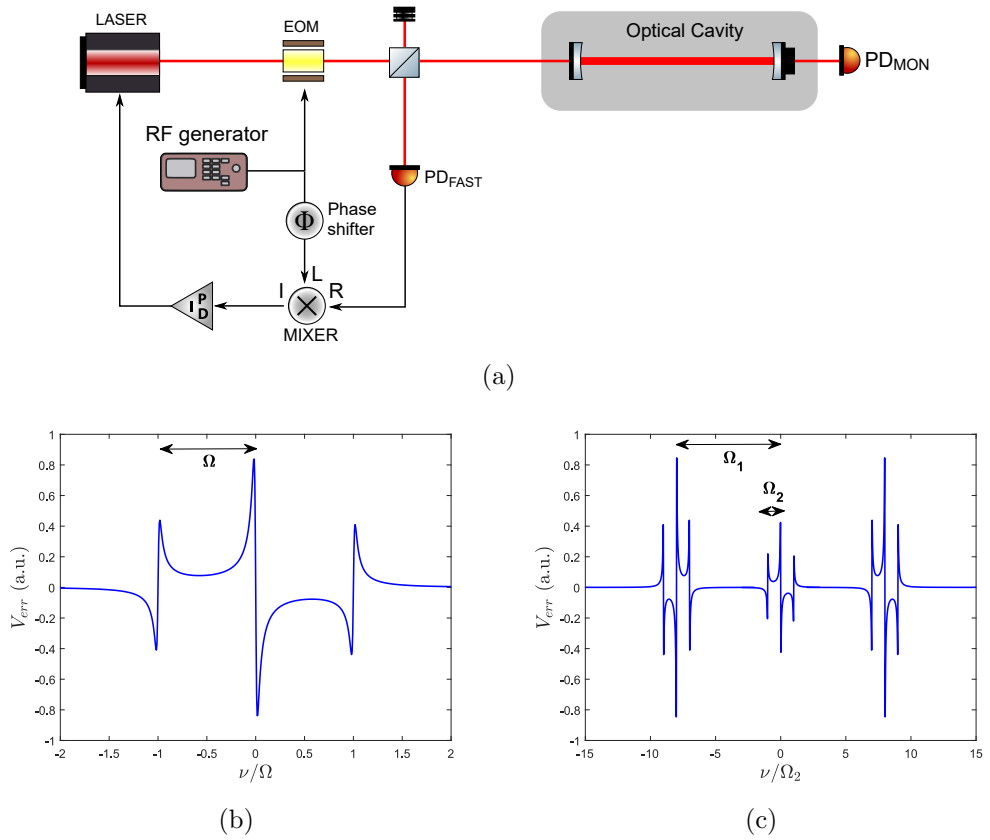

Figure 3.6: a) Schematic representation of PDH locking loop. Solid red line represents the optical paths and the black arrows represent the path of the electronic signals. b) Error signal after the mixer in the standard PDH configuration and c) in the dual sidebands configuration: in the latter, the same shape of the error signal is reproduced around $\omega_c \pm \Omega_1$

scheme. Fig. (3.6a) shows the basic setup of the locking loop. The light incident on the cavity is first phase-modulated, usually by an EOM, so that the electric field is of the form

$$E = E_0 \exp(i(\omega_c t + \beta \sin(\Omega t))), \tag{3.7}$$

where E_0 is the amplitude of the incident field on the modulator, ω_c is the angular frequency of the incoming light, β is the modulation depth, and Ω is the angular frequency of the modulation. If the depth β is small, the effect of phase modulation is to split the beam into three distinct frequency components: a carrier at $\omega = \omega_c$ and two sidebands at $\omega = \omega_c \pm \Omega$. For sufficiently large Ω, the sidebands are completely reflected when the carrier is near resonance. If the carrier is not perfectly in resonance, a portion of it will reflect and generate an intensity modulation by interfering with the reflected sidebands at a frequency Ω. When the carrier is near resonance the refelcted intensity $P_{ref,\Omega}$ is proportinal to the frequency difference between the carrier and the cavity resonance. Therefore, an error signal suitable for locking to the cavity resonance can be generated by measuring $P_{ref,\Omega}$ using a fast photodetector and demodulating the output signal by a mixer, in order to recover the components at $\pm\Omega$. The DC signal coming out from

the mixer is sent to a servo amplifier and then into the tuning port on the laser driver, locking the laser to the cavity. The shape of the error signal (Shown in Fig (3.6)b) can be adjusted introducing a phase shift between the local oscillator and the signal from the photodetector. Finally, there is an optimal modulation depth β that increases the slope of the error signal. This slope is a measure of the sensitivity of the error signal to fluctuations in the laser frequency or cavity length and it depends on the sidebands power. In particular, it is possible to demonstrate that the optimal power in the sidebands relative to the power in the carrier is [44]:

$$\frac{P_S}{P_C} \simeq 0.4 \tag{3.8}$$

Offset sideband locking

The standard PDH scheme shown before allows to lock the frequency of the laser to the reference cavity. We use this method to lock the light provided by the Mephisto. Since the double passage AOM provides a tunability of the frequency smaller than 200 MHz, for the other laser we use a slightly different technique, in order to have the possibility to tune the laser frequency with respect to the cavity resonance inside the whole FSR. The frequency of the carrier is then adjusted by changing the frequency used to generate the sidebands. This technique is called offset sideband locking [45, 46]. In particular we use a dual-sideband configuration (DSB), modulating the beam at two distinct frequencies, one of which is adjustable. The electric field that is phase-modulated with two sinusoidal signals of depth β_i and frequency Ω_i $(i = 1, 2)$ is given by

$$E_{DSB} = E_0 \exp(i(\omega_c t + \beta_1 \sin(\Omega_1 t) + \beta_2 \sin(\Omega_2 t))) \tag{3.9}$$

Expanding again to first order in $\beta_{1,2}$ the result of the phase modulation is a carrier with angular frequency ω_c, sidebands with angular frequencies $\omega_c \pm \Omega_1$, sidebands with angular frequencies $\omega_c \pm \Omega_2$, and sub-sidebands at $\omega_c + \Omega_1 \pm \Omega_2$ and $\omega_c - \Omega_1 \pm \Omega_2$. The error signal is shown in Fig. (3.6c) assuming $\Omega_1 > \Omega_2$ and $\beta_1 > \beta_2$. Note that the spectral structure centered around $\omega_c + \Omega_1$ with sidebands offset by Ω_2 is analogous to the standard PDH modulation spectrum in Fig. (3.6a). In DSB locking, this structure allows to place one of the $\omega_c \pm \Omega_1$ sidebands on resonance and demodulate the reflected power with Ω_2. In this way it is possible to tune the frequency of the laser changing Ω_1.

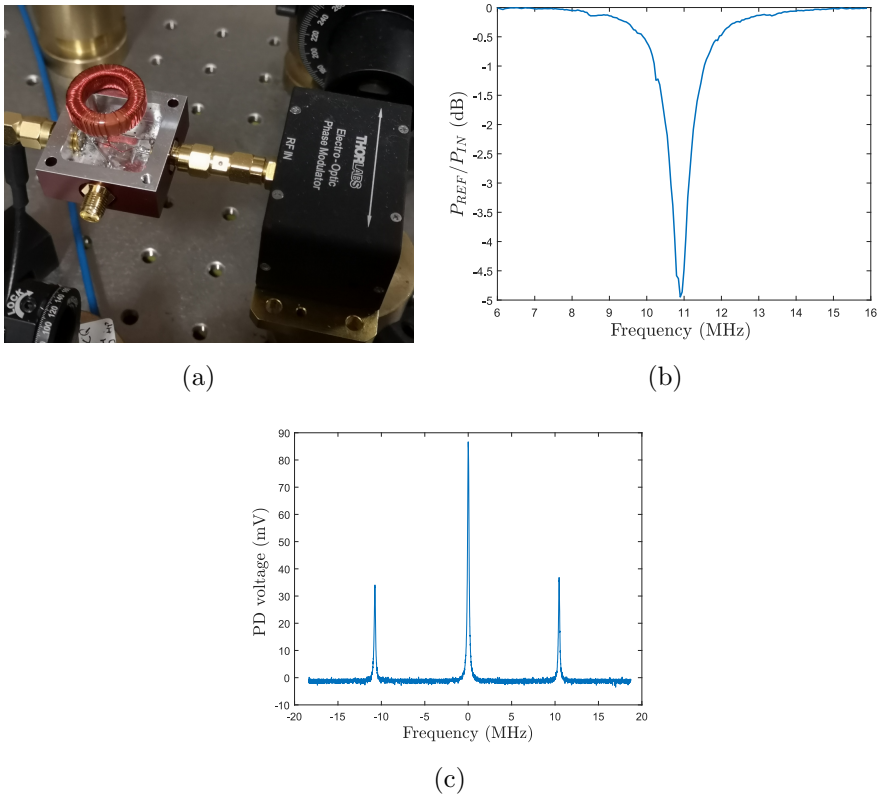

(a) (b)

(c)

Figure 3.7: a) Picture of the external inductor to create a resonant circuit with the EOM b) Fractional reflected power a s a function of the frequency sent to the EOM: the resonance is at 10.8 MHz. c) The signal on the photodiode after the cavity shows the two sidebands at $\omega_c \pm \Omega$

3.2.3 Electro-optical modulators

In order to phase modulate the light that enters the cavity we use two different Electro-optical modulators. For the light at 1064 nm we use a free-space EOM by Thorlabs that has an RF bandwidth of 50 MHz. The voltage required to drive this type of EOMs in order to achieve a good modulation depth is very high, of the order of 100 V. This value can be achieved only by high voltage amplifiers that usually are expensive and noisy. However, the non linear-cristal inside acts as a capacitor. Therefoer, I have assembled an external inductor and I have placed it at the RF input connection, as shown in Fig. (3.7a). This configuration corresponds to a resonant LC circuit whose resonance has ben measured with a Vector-Network-Analyzer. In Fig. (3.7b) I report the measured ratio between the reflected power and the input power as a function of the frequency. It shows a nice resonance around 10.8 MHz where the gain that we have measured is larger than 20. Sending an RF signal at this frequency with an RF generator and amplifying the signal up to 1 V we manage to generate two clear sidebands with a modulation depth near the optimal value expressed in (3.8). The signal recorder by the photodiode after the cavity is shown in Fig. (3.7c).
Usually, if the polarization of the light that enter in the EOM is not very clean and parallel

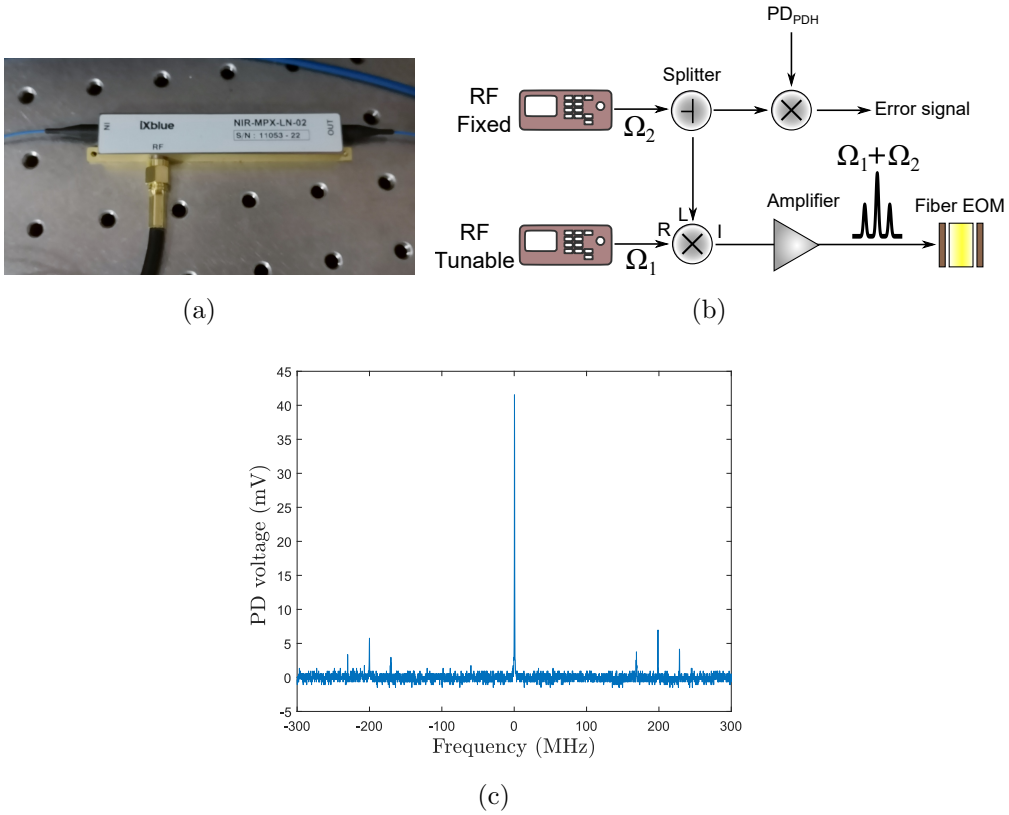

Figure 3.8: a) Picture of fiber-integrated EOM. b) Schematic representation of the RF line to produce the sidebands at $\Omega_c \pm \Omega_1$ and $\Omega_c \pm \Omega_1 + \Omega_2$, where Ω_1 is tunable. c) The signal on the photodiode after the cavity shows the sidebands and the sub-sidebands.

to the axis of the crystal, not only the phase but also the polarization is modulated. This modulation is translated to an intensity modulation by the cube after the fiber. Since the frequency is the same as the phase modulation, the effect is the appearence of a floor in the signal after the mixer that does not depend on the frequency of the laser but that is proportional to the intensity of the laser. This effect is called residual amplitude modulation (RAM) and it can cause an uncontrolled spread of the laser linewidth due to intensity fluctuactions. In order to minimize this effect we place a Glan Taylor polarizer before the EOM in order to clean very well the polarization.

For the frequency locking of the light at 1013 nm we use a more complicated scheme. First, we use a fiber-integrated EOM by IXblue (NIR-MPX-LN-02) (Fig. (3.8a)) that has a very large RF bandwidth, of the order of 2 GHz. It requires a low RF power to obtain a good modulation depth, indipendently on the frequency. Moreover, it is possible to drive it with more than one RF frequency and it is suitable for the offset dual-sideband locking scheme that I presented before. A sketch of the setup that we use to generate the RF signal is shown in Fig. (3.8b). The two frequencies Ω_1 and Ω_2 are generated by two different RF generators, where the first one is tunable up to 2 GHz and the second one is fixed at 30 MHz. The two signals are sent into a mixer in order to generate high order harmonics. In particular the highest components are at $\omega = \Omega_1 \pm \Omega_2$, the ones

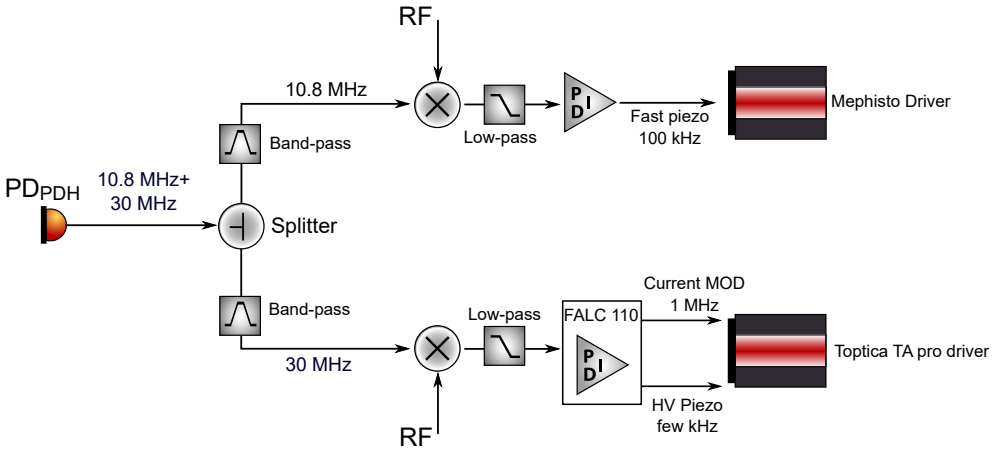

Figure 3.9: Sketch of the electronic circuit to exract the two error signals from the fast photodetector that measured the retroreflected light from the cavity. Each signal is sent to the correpondent PID controller and laser driver.

which we are interested in. The output of the mixer is then amplified to the desidered power and sent to the EOM. The resultant spectrum on the monitor photodiode shows the complicated spectrum of sidebands and sub-sidebands that we expected (Fig. (3.8)c). At the same time, a part of the signal at Ω_2 is taken to demodulate the PDH signal from the fast photodetector.

3.2.4 Multi-wavelengths locking scheme

There are different proposals to obtain indipendent error signals in the case of different lights inside the same optical cavity. One solution, shown in [46], is to divide the different wavelengths with specific dichroic mirrors and use more fast photodiodes, one for each wavelength. In our case we have decided to use a different scheme (Fig. (3.9)), where it is possible to exploit only one photodiode. In particular, the PDH signal from the photodiode is splitted in two parts and the two frequency components are filtered by using band pass filters. Each component is then mixed togheter with the correpondent local oscillator by a mixer that generates the error signal. The two error signals are shown in Fig (3.10). In the case of the Mephisto we send the error signal to a PID controller that has bandwidth of 200 kHz and its output is connected to the piezo driver of the laser that has a nominal bandwidth of 100 kHz. For the Toptica TA pro we use instead a commercial PID controller (FALC 110) that has two output channels. The fast output has a bandwidth up to few MHz and it is connected to the fast current modulation input of the driver with a bandwith of about 1 MHz. This part reduces the noise for frequencies larger than few tens of Hz. The slow output has instead a transfer function that is enhanced in the very low frequency range and it is exploited to cancel slow drifts keeping the frequency around resonance. The output of this part is connected to a HV piezo inside the laser head that has a large tunability in terms of frequency but a very small bandwidth.

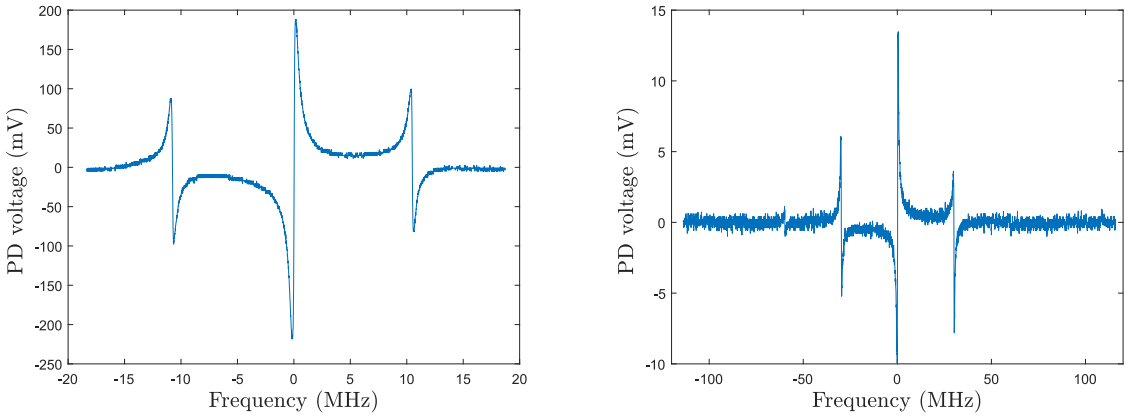

(a) (b)

Figure 3.10: Error signal after the last mixer of the 1064 nm laser when the carrier is near reosonance in (a) and of the 1013 nm laser when the sideband at $\omega + \Omega_1$ is on resonance in (b)

3.3 Extimation of the linewidth

Let us consider the electric field of the laser as:

$$E(t) = Ae^{i(2\pi\nu_0 t + \varphi(t))} \tag{3.10}$$

where A is the amplitude that changes slowly respect to $1/\nu_0$, ν_0 is the carrier frequency and $\varphi(t)$ is the istantaneous modulation of the phase. The frequency modulation of the ligth field is defined as the instantaneous variation of the phase:

$$\nu(t) = \nu_0 + \frac{1}{2\pi}\frac{d\varphi}{dt} \tag{3.11}$$

where the second term $\delta\nu(t) = \frac{1}{2\pi}\frac{d\varphi}{dt}$ is called the frequency noise of the field. We can define the spectral density noise (frequency PSD) the function defined as:

$$S_\nu(f) = \lim_{T\to+\infty} \frac{1}{T}\left| \int_0^T \delta\nu(t)e^{-i2\pi ft}dt \right|^2 \tag{3.12}$$

where f is the Fourier frequency. The function $S_{\delta\nu}(f)$ is a distribution that describes the frequency noise of the laser.
In [47] a simple method to extimate the linewidth of the laser starting from the frequency noise spectrum is shown. The frequency noise spectrum can be separated into two regions that affect the lineshape in a different way. In the first region, defined by $S_{\delta\nu}(f) > 8ln(2)f/\pi^2$, the noise contributes to the central part of the line shape and thus to the laser linewidth. In the second region, defined by $S_{\delta\nu}(f) < 8ln(2)f/\pi^2$, the noise contributes mainly to the wings of the lineshape but does not affect the linewidth. The striking difference between the noise effects in these two regions can be understood in terms of frequency modulation theory. In the first region, the noise level is high compared to its Fourier frequency, therefore it produces a slow frequency modulation with a high

modulation index $\beta > 1$, where β is defined as the ratio between the deviation $\Delta\nu$ and the modulation frequency f. Instead, in the second region, the noise level is small compared to its Fourier frequency and the modulation index β is small, which means that the modulation is too fast to have a significant effect on the laser linewidth. The line separating these two regions is called the β-separation line. As a result, the line shape is a Gaussian function whose variance is the sum of the contributions of all high modulation index noise components. Therefore, one can obtain a good approximation of the laser linewidth by the following simple expression [47]:

$$\Delta_{FWHM} = (8\ln(2)A)^{1/2} \tag{3.13}$$

where A is the surface of the high modulation index area, i.e., the overall surface under the portions of $S_{\delta\nu}(f)$ that exceed the $\beta - separation$ line

$$A = \int_{1/T_0}^{+\infty} H(S_{\delta\nu}(f) - 8ln(2)f/\pi^2)S_{\delta\nu}(f)df \tag{3.14}$$

where H is the Heaviside unit step function and T_0 is the measurement time that prevents the observation of low frequencies below $1/T_0$.
We optimized the lock using the noise spectrum of the in-loop PDH error signal measuring it by an FFT spectrum analyzer. The measured spectra after the optimization of the lock performances, is reported in Fig. (3.11) and (3.12). The cut-off frequency $1/T_0$ is 0.5 Hz. The traces are composed by spectra normalized by their resolution bandwidth and the volt-to-hertz conversion factor is estimated from the PDH signal amplitude.
The Mephisto MOPA laser in free running configuration has a linewidth that is already quite small, since it has a cavity inside its head. The company ensure a linewidth near 1 kHz. As one can see from Fig. (3.11), almost all the frequency noise is under the β-line, except for the peak at f=50 Hz. The magnitude of this component is very close to the β-line and we expect that its contribution to the linewidth is very small. The origin of this peak is the frequency modulation of the AC supply current. At frequencies higher than 50 kHz the noise is flat because the laser itself has a high frequency stability. Using the expressions (3.13) and (3.14), the extimated linewidth is about 100 Hz. Unfortunately, we can't measure the in-loop frequency noise when the laser is not locked because its PID controller does not have a slow output that keeps the laser near resonance.
The TOPTICA laser, instead, is based on a laser diode and we expect a significant frequency noise in absence of an active stabilization. When only the slow channel of the PID is switched on, we observe that the noise level is above the beta line for most of the frequency range of the measurement (see Fig (3.12)). Performing the same calculation as in the previous case, the extimated free-running linewidth is about 100 kHz. When the laser is locked to the cavity we observe instead a significant reduction (of about three order of magnitude) of the noise in the low frequency region, which is the most significant for the laser linewidth narrowing. For frequency higher than 10 kHz the noise level grows up again but it remains under the β-line. The final linewidth is of about 1.2 kHz.

However, despite the in-loop spectra can provide information about the performances of the locking system, the contribution of the cavity noise is not taken into account. The real laser linewidth can be determined only exploting an external reference that has better spectral properties or only by observing atomic transitions.

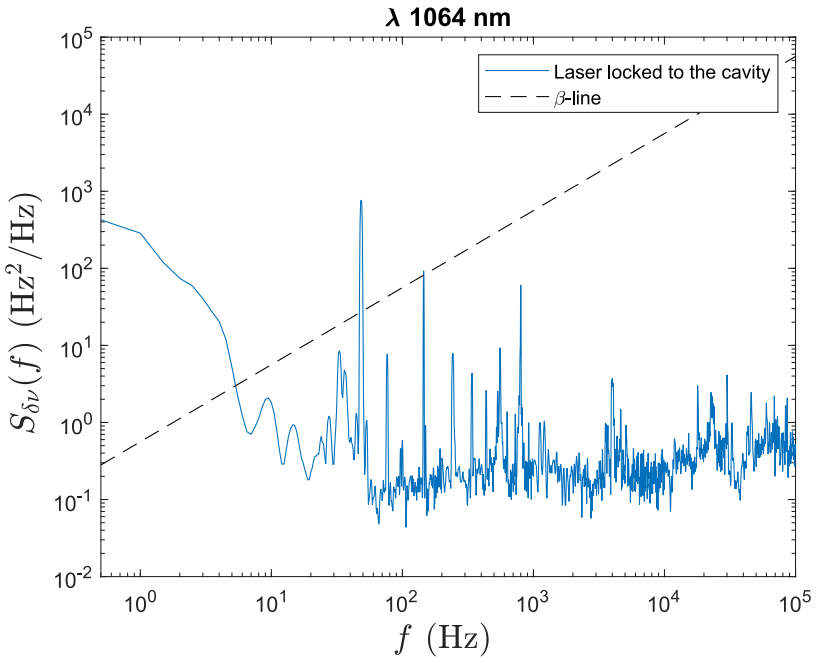

Figure 3.11: Frequency noise spectrum of the laser at 1064 nm locked to the cavity. The β-line [47] is a limit above which the frequency noise components contribute significantly to the laser linewidth.

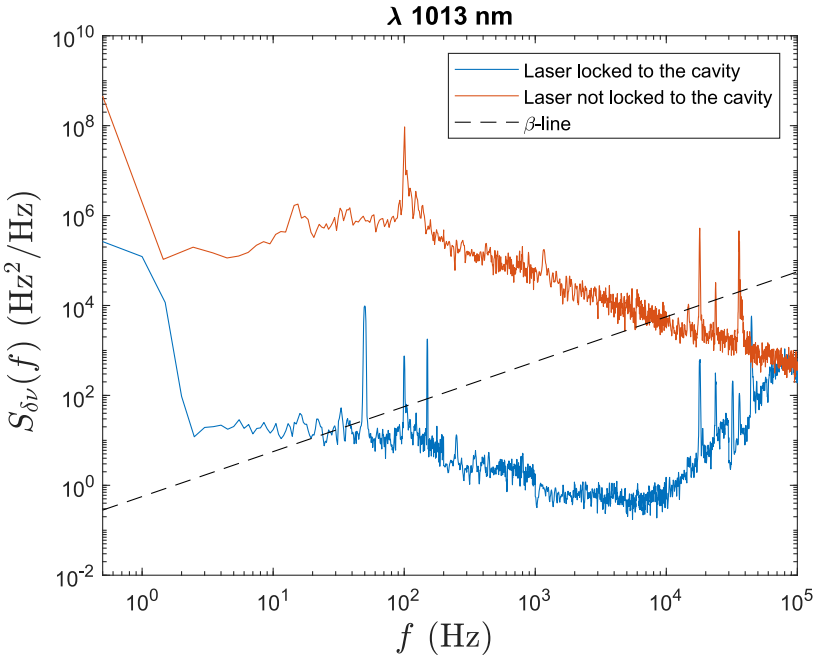

Figure 3.12: Comparison between the noise spectrum of the 1013 nm laser in free running and when it is locked to the cavity. I report again the β-line as a reference.

Chapter 4

Experimental results on the beat-note lattice

In this chapter, I start describing the calibration of the lattice depth that we perform measuring the on-site trapping frequencies. From the knowledge of the lattice depth we can extimate the tunneling rate between neighbouring sites by the help of numerical simulations. Since our goal is to induce Bloch oscillations, we need to know very well which forces are present on our system. For this purpose, I show some measurements of the residual forces exploiting two different methods: observing the clouds in free expansion and, in the case of magnetic force, exploting RF spectroscopy on two separate condensates. I show how we manage to observe a coherent dynamics in the BL in presence of an external force starting from two different initial conditions: populating only one site or starting with a condensate spread over few sites. Finally, I compare the experimental data with the theoretical expectation predicted for Bloch oscillations. In the last section, I explain some future improvements that can help to enhance the stability of our system.

4.1 Calibration of the lattice depth

The two main parameters that characterize an optical lattice is the tunneling rate between neighbouring sites and the energy gap between the first bands. These two quantities depend on the lattice depth that we can control changing the intensity of the laser beams. A measurement of the lattice depth can be perform indirectly by measuring the trapping frequency in a single well that, in the regime where the energy bands are flat, correponds to the first energy gap.
The experimental sequence that we use is simple. After the evaporation, we load the atoms in few wells and we switch off the dipole trap beam that provides the longitudinal confinement. Then we change instantaneously the position of the minima of the periodic potential. The condensates are initially out of equilibrium and start to oscillate inside the wells. Fitting the oscillations we can extract the frequency.
In order to shift the position of the minima we change the frequency of the RF that we

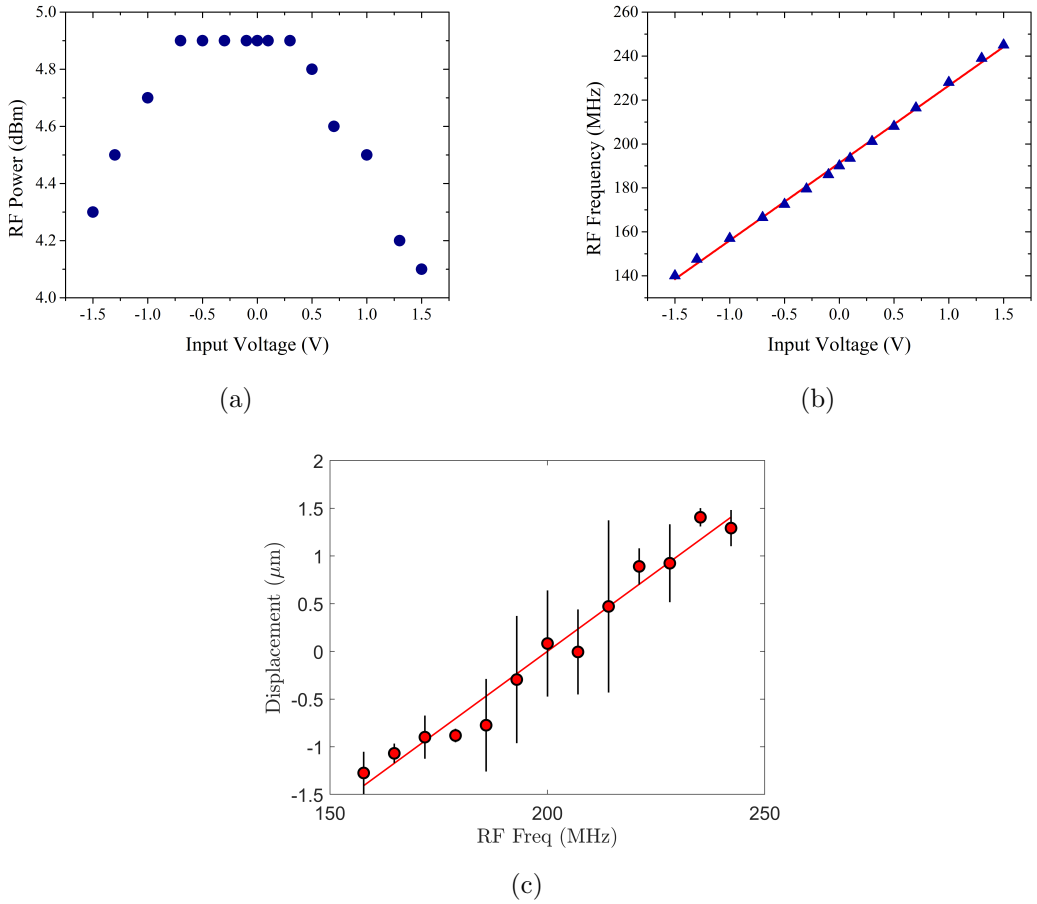

Figure 4.1: Power (a) and frequency (b) of the RF signal sent to the double passage AOM used to control the lattice phase as a function of the control voltage. In c) I report the displacement of the minima of the lattice as a function of the detuning of the frequency of the RF.

sent to the double passage AOM showed in section (3.1.3). In general, in a configuration where the optical lattice are generated by retro-reflected beams, the phase difference between the two beams can be adjusted changing the wavelength of the radiation. Correspondently the position of the maxima (or minima) of the potential moves. A relative variation of the laser frequency $\Delta\nu/\nu$ correponds to a shift of the position $\Delta x \simeq \frac{\Delta\nu}{\nu}L$, where L is the distance between the atoms and the retro-reflecting mirror. The BL is the superposition of two lattices, so we need to extract the dependence numerically. We calculate that the displacement of the minima respect to a variation of the frequency is of the order of $\Delta x_0 \simeq 0.02\mu$m/MHz.
In Fig. (4.1) I report the frequency and the power of the RF provided by the AOM driver as a function of the control voltage. The AOM has a nominal RF bandwith of 90 MHz and, in the range from -1 V to 1 V, it is possible to tune the frequency around 200 ± 40 MHz without significantly changing the RF power. Thanks to the double-passage configuration, this shift corresponds to a laser frequency variation of 160 MHz. According to the numerical extimation, we experimentally measure (Fig. (4.1c)) that this tunability

allows to move the position of the minima up to 2 μm that is large enough respect to the spatial resolution of our imaging system.
Some examples of oscillations of the center of the condensate in a single site, recorded for different values of the lattice depth, are reported in Fig. (4.2). We observe an interesting behaviour: a clear beat-note between two different frequencies appears for all the values that I report. Two frequencies correponds to two different energy scales. Our interpretation is that the non complitely harmonic shape of the potential leads to an energy spectrum where the distance between the first energy bands is not the same. If the initial wavefunction is projected not only on the second band but also on the third one, we expect an oscillation of two different frequencies, corresponding to the energy distance between the energy bands. Therefore, we fit all the oscillations with the product of two sinusoidal functions and the fit reproduces very well the observed behaviour. The non zero population of the third band is caused by the the instantaneous shift of the BL position, that enlarge the momentum distribution and can provide additional kinetic energy to the atoms.
In Fig. (4.3) I show the measured trapping frequencies as a function of the lattice depth that is extimated by the geometrical and optical characteristics of the beams measured by a CCD camera. In order to confirm the picture of more bands involved in the dynamics, I compare the experimental data with the theoretical values of the energy difference (expressed in terms of frequency) between the first three bands. The good agreement between the experimental data and the theory confirms the prediction and provide a good calibration of the energy gap and the tunneling of the BL. Moreover, it indicates that, for certain values of the optical intensity, the beat-note lattice works as expected as an effective large spacing optical lattice. However, on site it does not reach the behaviour of a pure harmonic potential.

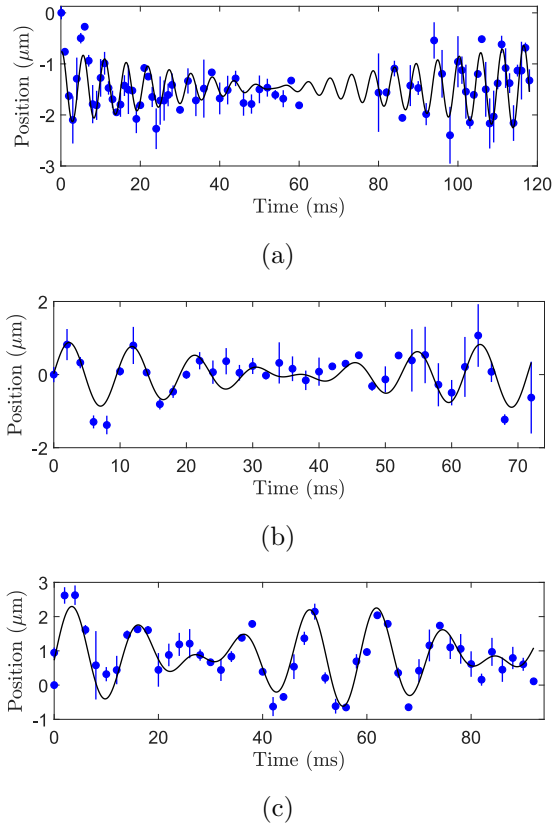

Figure 4.2: On-site oscillations of the condensate in the BL for different values of the lattice depth: a) 400 nK b) 200 nK c) 140 nK. The appearance of a beating between two different frequencies is clear.

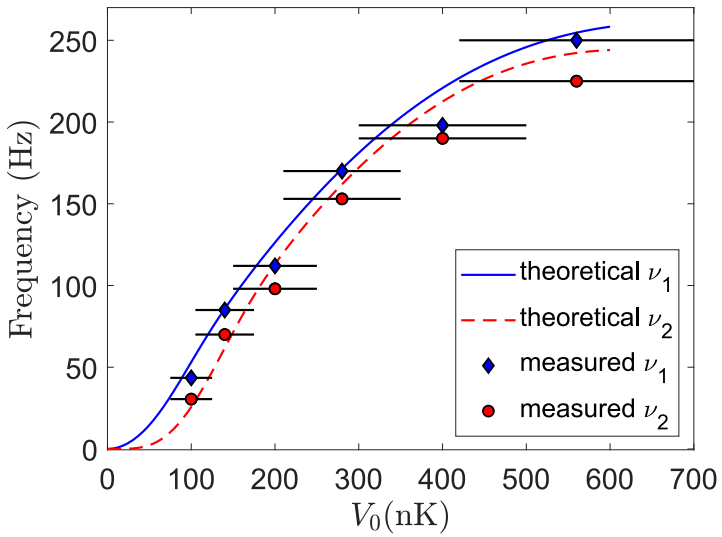

Figure 4.3: Measured trapping frequencies as a function of the lattice depth. The red dots and the blu diamonds are the experimental data, where the error bars on the lattice depth take into account the uncertainties of the measurements of the beam's size and of the optical power. The solid blu line and the dashed red line represent the theoretical values of the first two gaps.

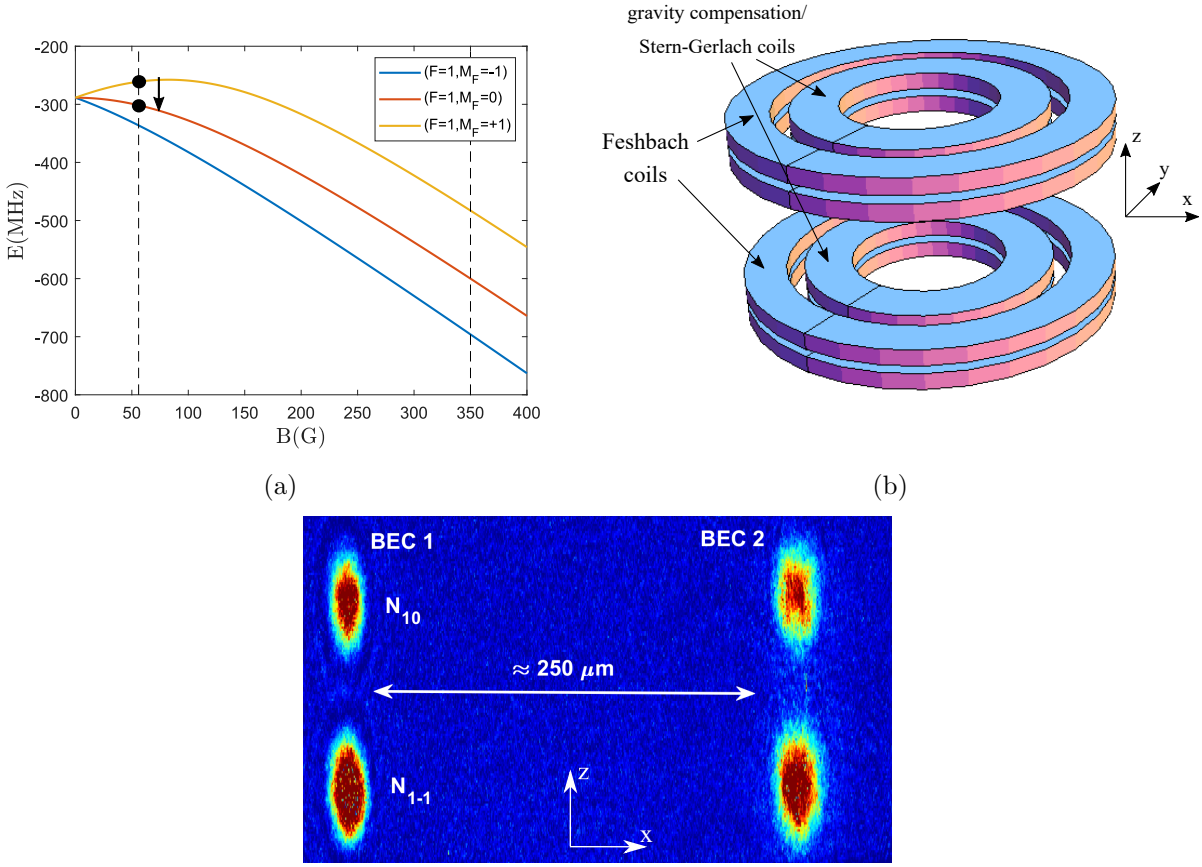

Figure 4.4: a) Magnetic field dependence of the energy of the various ground state magnetic sublevels of 39K. RF spectroscopy measurements are performed at B=56 G exploiting the transition $M_F = -1 \rightarrow M_F = 0$ instead all the experiments in the lattice are performed around 350 G. b) Sketch of all the coils that are present around the science chamber. c) Image of the two clouds in time of flight during a Stern-gerlach experiment to measure the magnetic gradient.

4.2 Measurement of the residual forces on the system

During the measurements of the trapping frequencies, for small values of the lattice depth, we have observed a residual force on the atoms that tends to drag them away from the initial position. In order to compensate this effect we slightly move the focus position of the radial beam and we tune its intensity to provide an opposite force. Moreover, the knowledge of the residual potential applied on the sample is really important in the realization of an interferometer. In this section we will focus the attention on the methods that we have used to measure these residual gradients and to calibrate and control the applied force on the condensate.

4.2.1 RF spettroscopy at low magnetic field

The energy of the three hyperfine state of the lowest energy manyfold $F = 1$ of the ^{39}K is shown in Fig (4.4a). The magnetic dipole of each state correpond to the derivative of the energy respect to the magnetic field. At values smaller than 150 G, the three hyperfine states show different magnetic dipoles. For this reason a spectroscopic measurement that exploits RF transitions between two hyperfine states is possible. Observing two different BECs far away one from the other can provide information about magnetic gradients that are present in the chamber. A sketch of all the magnetic coils present around the chamber is shown in Fig. (4.4b). If there is a difference in the local magnetic field, the resonant frequency between the internal states of the two condensates will be shifted by a proportional quantity.
Experimentally we perform measurements around B=56 G exploiting the transition between the hyperfine states $|F = 1\,|M_F = -1\rangle$ and $|F = 1\,|M_F = 0\rangle$. At this value of the magnetic field both the states have respulsive interactions, ensuring the stability of the condensate. The difference between the two magnetic dipoles is 0.7 MHz/G $\simeq 0.5\ \mu_B$, where μ_B is the Bohr magneton. After the condensation in the $|F = 1\,|M_F = -1\rangle$ in the radial beam, we load the atoms in two crossed dipole traps, made by using the IPG and an additional IR beam (see Fig. (4.4)c) that comes from below and that intersects the radial beam. According to the dimensions of our imaging system, we manage to separate the two condensates up to 250 μm. After the loading, we set the magnetic field around 56 G and we apply an RF pulse of 60 μs on the sample. We adjust the amplitude and the length of the RF pulse in order to completely transfer all the atoms in the $|F = 1\,|M_F = 0\rangle$ state. After the pulse we switch off the dipole trap and let the atom move in a vertical magnetic gradient, generated by the coils that we use to compensate gravity (see Fig. 4.4b). Due to the different magnetic dipole moments the two states spatially separate as in a Stern-Gerlach experiment and we can count the atom number in the different components.
First, we measure the residual magentic gradient when only the Feshbach field is on. The Feshbach coils are designed to produce a very homogeneous magnetic field, therefore we do not expect to observe a difference in the resonant frequency. Scanning the frequency of the RF pulse we obtain the profiles shown in Fig. (4.5), where I report the fraction of the transferred atoms as a function of the RF frequency. We fit indipendently the two curves and we extract the position of the central frequencies $\nu_{1,2}$. As expected, the difference $\Delta\nu = \nu_1 - \nu_2$ is lower than 0.4 kHz, that correponds to a magnetic gradient smaller than 20 mG/cm.
However, this technique is limited by the common fluctuactions of the magnetic field. In order to achieve an higher sensitivity we can exploit the fact that we measure the magnetic field in two different positions at the same time. For a single realization the two

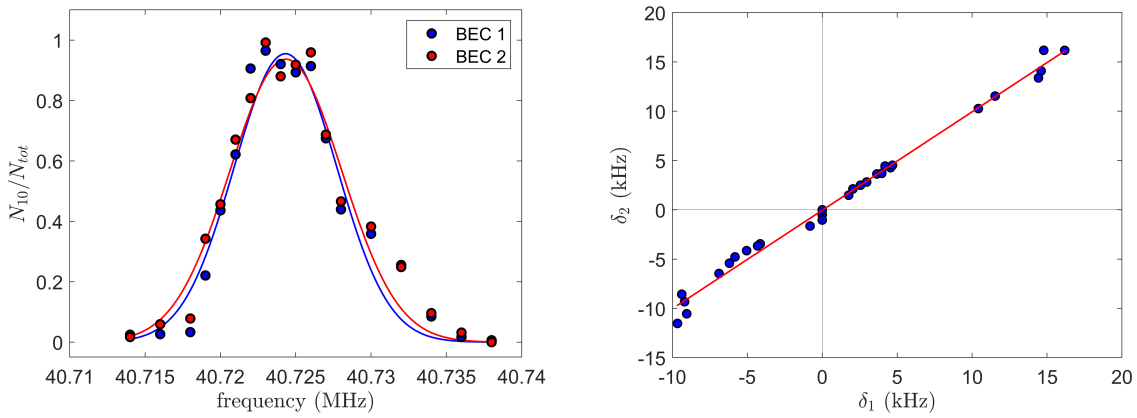

(a) (b)

Figure 4.5: a)Fraction of the transferred atoms in the two BECs as a function of the RF frequency, in presence of the Feshbach magnetic field only. No appreciable shifts are present. b) Corrispondent comparison between $\delta_{1,2}$, extracted solving the equation (4.1). The results of the measurement is reported in Tab. (4.1).

measured fractions of the transferred atoms in the $|F = 1\,|M_F = 0\rangle$ are:

$$\begin{aligned} \frac{N_{10}}{N_{tot}}\Big|_1 &= \frac{\Omega^2}{\Omega^2 + \delta_1^2}\sin\Big(\sqrt{\Omega - \delta_1}\Delta t\Big) \\ \frac{N_{10}}{N_{tot}}\Big|_2 &= \frac{\Omega^2}{\Omega^2 + \delta_2^2}\sin\Big(\sqrt{\Omega - \delta_2}\Delta t\Big) \end{aligned} \tag{4.1}$$

where Ω is the Rabi frequency and $\delta_{1,2} = \nu - \mu B(x_i)$ is the detuning from the resonance of each cloud. The Rabi frequency Ω can be measured from coherent Rabi oscillation between the two hyperfine states. The only unknown quantities are $\delta_{1,2}$ that we can extract solving numerically the two equations in (4.1) for each realization. In Fig. (4.5) I report on each axis the measured values of δ_i togheter with a linear fit. If the intercept of the line is different from zero, it provides a mesurement of the deviation between the two resonances where the common noise of the magnetic field is removed. Indeed, the uncertainty is reduced by a factor around 2-3 and the resulting shift is lower than 0.2 kHz. The result provides an upper value for the residual magnetic gradient of 10 mG/cm. We repeat the same procedure switching on the coils for gravity compensation and we find a different situation. As shown in Fig. (4.6) mainly two effects can be identified. First, we observe a global shift of both the resonances of the order of few hundreds of kHz, that correponds to a changing of the bias field B_0 of the order of $0.1 - 0.3$ G. This offset can be taken into account during the Feshbach field calibration, and it is not relevant for our purposes. More importantly, we observe a small deviation between the central peaks of the two resonances that higlights the presence of a spatial gradient of B along x, that is more relevant because represents an additional potential along the direction of the lattice. Such effect can be due to non-pefect anti-Helmoltz configuration of the coils.
In order to characterize better this gradient, we probe the field for different values of the

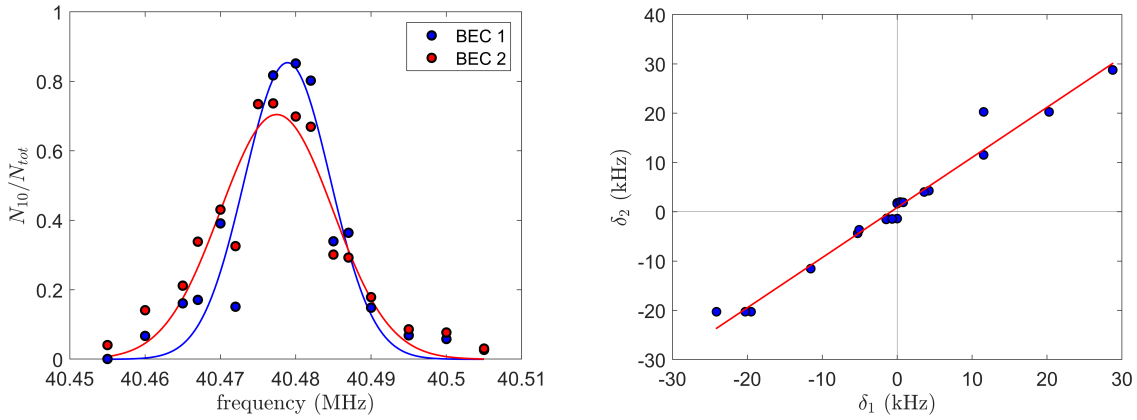

(a) (b)

Figure 4.6: a) Fraction of the transferred atoms in the two BECs as a function of the RF frequency, in presence of the Feshbach magnetic field plus the gradient generated by the gravity compensation coils with a current of 3 Amps. The centers of the two resonances are shifted by about 1 kHz b) Corrispondent comparison between $\delta_{1,2}$ extracted solving the equation (4.1). The results of the measurement is reported in Tab. (4.1)

	$\Delta\nu$ (kHz) (independent fit)	$\Delta\nu$ (kHz) (correlated fit)	ΔB_0 (G)	$\Delta B/\Delta x$ (mG/cm)
Fesh only (56 G)	< 0.4	< 0.2	/	< 10
Fesh (56 G) + Grad (2A)	1.7 ± 0.9	0.9 ± 0.3	0.23 ± 0.01	50 ± 16
Fesh (56 G) + Grad (3A)	1.4 ± 1	1.4 ± 0.5	0.35 ± 0.01	80 ± 30
Fesh (56 G) + Grad (5A)	1.3 ± 1.4	1 ± 0.6	0.56 ± 0.01	60 ± 40

Table 4.1: The table resumes the results of the measurements of the residual magnetic gradient in four different conditions. I report the result of both the analysis discussed in the text, here labelled as "independent" and "correlated" fit. As one can see, when the coils for gravity compensation is switched on there is a residual gradient of B along x.

current that flows in the coils. I summarize all the results in the Tab. (4.1). As expected the offset in the bias field is proportional to the current. The residual gradient instead does not show a dependence on the current. The reason why it does not depend on the current is now under investigation. The dynamics that I'll show in the next sessions will be driven by acceleration of the order of 10^{-3} μm/ms^2, that corresponds to a magnetic force of 10^{-3} G/cm. For this reason we are looking for a realiable method to compensate such residual magnetic gradient.

As I explained in the previous chapter, all the experiment in the lattice are performed in the state $|F = 1\,|M_F = 1\rangle$ around 350 G. The most reliable procedure should be measuring the residual gradient at the same value of magnetic field starting from the same hyperfine state. However, in this region (see Fig. (4.4)a) all the sublevels in the manifold $F = 1$ have a similar magnetic dipole moment. In particular, the difference is

smaller than 0.06 MHz/G. The resonances of two clouds 300 μm far from the other that experience a gradient of 0.1 G/cm will be shifted by 0.2 kHz that is of the same order of our uncertainty.

4.2.2 Balistic expansion in the radial beam

In order to measure the residual force on the condensate at high magnetic field, we can observe the motion of the atomic cloud during a free expansion in the waveguide provided by the radial beam. This measurement can be useful to understand the magnitude and the sign of spurious forces.
The first measurement that we perform is the observation of the expansion with only the Feshbach field on. Surprisingly, while at low magnetic field we measure a negligible force, we observe a strong acceleration. Because of that, we slightly move the focus of the radial beam respect to the position of the crossed dipole trap (made with the IPG) where the condensate is produced. In this way the dipole potential inprints an optical force on the sample that can compensate the magnetic one. The magnitude and the sign of the total force can be therefore controlled tuning the intensity of the optical beam.
We perform the same measurement with only the Feshbach field on for different values of the intensity of the radial beam. We observe a parabolic trajectory, higligthing the presence of an external constant force. We fit the data with a parabolic function and we extract the acceleration. The three different trajectories are shown in Fig. (4.7) where I report the correpondent measured acceleration as a function of the power of the radial beam P. The acceleration goes linearly as a function of P and the intercept at P=0 provides a measurement of the residual gradient when the optical force is switched off. We measure a strong acceleration of the order 0.3 μm/ms^2. If we convert this value in a magnetic gradient, it correponds to $\Delta B/\Delta x \approx 0.2$ G/cm, much larger than the one we measure at B=56 G. We repeat the measurement in the working condition, i.e with both the Feshbach and the gravity compensation coils on, and we find a gradient a factor of two smaller. The levitating system creates a force in the opposite direction that naturally helps to compensate the spurious gradient. The magnitude of the component provided by the levitating system is of the order of 0.1 G/cm, that is comparable with the measurement performed by using RF spectroscopy. Finally, in order to check if the strong acceleration that we measured comes only from spurious magnetic fields, we observe the motion of a condensate in the state $|F = 1\,|M_F = -1\rangle$ at B=83 G. At this field the sample has a negligible magnetic dipole moment, of the order of $5 \cdot 10^{-3}$ μ_B. The resulting residual acceleration at P=0 is 0.06 μm/ms^2, much smaller than in the first case. It indicates that the main contributions to the residual gradients are provided by some magnetic effects acting on the apparatus. For example, due to the high field and the high currents that flow in the Feshbach coils, some thermal and mechanical effects can occur, leading to some deformations of the structure and the position of the coils. Moreover, the high field can magnetize some objects around the chamber, leading to a deformation of the magnetic field lines.

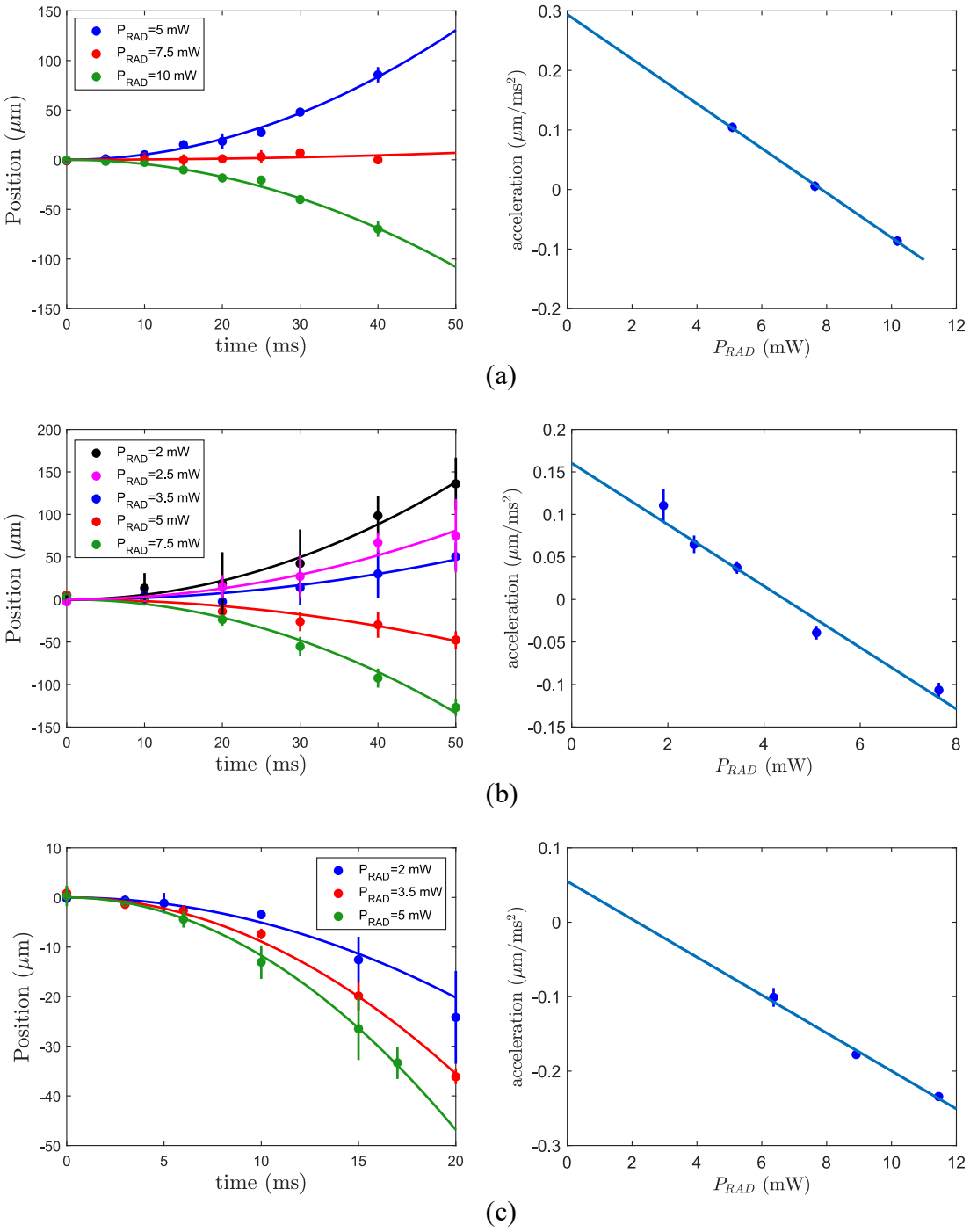

Figure 4.7: Trajectories of the free expanding condensate in the radial beam (left) and correspondent measured acceleration as a function of its optical power (right). The measurements are performed with only the Feshbach field on at 350 G (a), with the gravity compensation switched on (b) and with a non magnetic cloud at B=83 G (c).

	a_{cc} (μm/ms^2)
B = 350 G	0.29 ± 0.01
B = 350 G + Anti G ON	0.160 ± 0.015
B = 83 G	0.06 ± 0.02

Table 4.2: The table resumes the results of the measurements of the acceleration during a free expansion in the radial beam.

The measured acceleration at B=83 G could be due to the non perfect orizzontal alignement of the radial beam. If the direction of the beam has an angle θ with the horizzontal direction, a fraction of gravity equal to $g \sin\theta$ is applied on the sample along x. From the measured value we can extimate that $\theta = \arcsin(a/g) \approx 6 \cdot 10^{-3}$ rad.

4.2.3 Calibration of the local force on the sample

The goal of this work is to observe Bloch oscillations in presence of very weak forces. In an optical lattice, the maximum tunneling rate between neighbouring sites is of the order of $E_R/4$. Since we are working with a spacing of 10 μm, it corresponds to about 3 Hz. In order to achieve an appreciable amplitude of the dynamics in situ and avoid that the atoms will be dragged away, we have to apply accelerations smaller than 0.2 Hz/μm$\sim 2 \cdot 10^{-3}$ μm/ms^2. For this reason, we keep the radial beam out of focus and we tune the intensity to change the local force that is applied on the sample.
Since the force is provided by a focused laser beam, it depends on the spatial profile of the intensity. The peak intensity of a gaussian beam along the direction of propagation x is given by:

$$I_0(x) = \frac{2P_0}{\pi w(x)^2} \tag{4.2}$$

where the $1/e^2$ waist $w(x)$ evolves in space following the relation $w(x) = w_0\sqrt{1 + (\frac{x-x_0}{x_R})^2}$, with w_0 the waist in the focus placed at x_0, x_R the Rayleigh range and P_0 is the total optical power. The correspondent dipole force $F = -\frac{dU}{dx}$ is reported in Fig. (4.8). It shows a strong dependence on the position. In order to minimize such dependence we place the atoms around an extremal point where the derivative of the force is negligible. Measuring the radial trapping frequency in different positions we extimate a waist $w_0 \approx 17$ μm and that the atoms are distant 450±50 μm from the focus.
One way to calibrate the total force applied on the system, is to observe spatial Bloch oscillations [33] in a single lattice with $d = 0.5$ μm. The procedure that we exploit is the following. We load the condensate in the crossed dipole trap with radial trapping frquencies of $\omega_\perp \approx 2\pi \cdot 200$ Hz and a longitudinal frequency of about $\omega_\parallel \approx 2\pi \cdot 40$ Hz. We then adiabatically ramp up only the intensity of the lattice with $\lambda = 1064$ nm and we change the Feshbach field in order to have negligible interactions. We switch off instantaneously the longitudinal harmonic trap and we let the condensate moves in the

lattice in presence of the force. We repeat the same measurement for different value of the radial beam.
In Fig. (4.9a) I report the measured frequency as a function of the power of the radial beam. We observe a linear behaviour of the frequency only for large values. When the frequency approaches zero, we observe instead a deviation.
The oberved behaviour is mainly related to two limitations of this technique. The first one is the limited interogation that is influenced by the loss of coherence during the evolution. In this experiments we manage to observe a clear dynamics up to half a second. We need to work with an high lattice depth and intensity fluctuactions can cause heating in the sample and shorten our interrogation time. Since the frequency scales like $1/d$ it is not possible to perform measurements with forces smaller than 1 Hz/μm, that correspond to 20 Hz in the BL. We need to reach values that are one order of magnitude smaller.
The second limitation is related to the amplitude of the oscillations. If we reduce the lattice depth in order to decrease the heating effects, the amplitude becomes larger than the field of view of the imaging system. On the other side, the maximum lattice depth that we can achieve is $V_0 \approx 5E_R$ and it is not enough to confine the motion of the cloud in a region where the force is almost constant even for the largest value of the force we can apply. As a test, we observe bloch oscillations for a fixed value of the force changing the depth of the lattice. We find (Fig. (4.9)b) a significant variation of the frequency, indicating that the atoms explore regions where the force depends significantly on the position. The example that I show, corresponds to the maximum value of the frequency measured in Fig. (4.9a). For smaller forces the situation is even worse because the amplitude is inversely proportional to the frequency. In conclusion, we cannot use this type of measurements as a calibration of the local force on a length scale of few tens of micrometers.
As an alternative way, we can observe again the balistic expansion of the sample inside the radial beam measuring its position after a fixed time. We set the scattering length of the condensate slightly negative, in order to reduce the spreading of the wave function, and we record the position of the cloud, changing the intensity of the radial beam. During this expansion the displacement of the condensate from the starting point is always smaller than ± 20 μm. Therefore, despite the precision of measurement is not very high, the results shown in Fig.(4.10) can provide a first calibration of the local force as a function of the power of the beam.

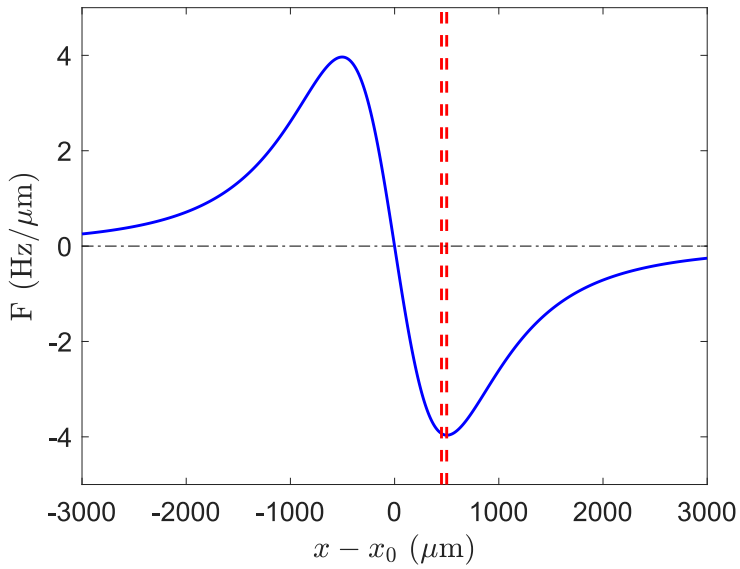

Figure 4.8: a) Dipole force provided by the radial beam as a function of the displacement from the position of the focus x_0. The values are calculated for a power of 1 mW. The two vertical dashed lines indicate the uncertainty in the knowledge of the position of the atoms.

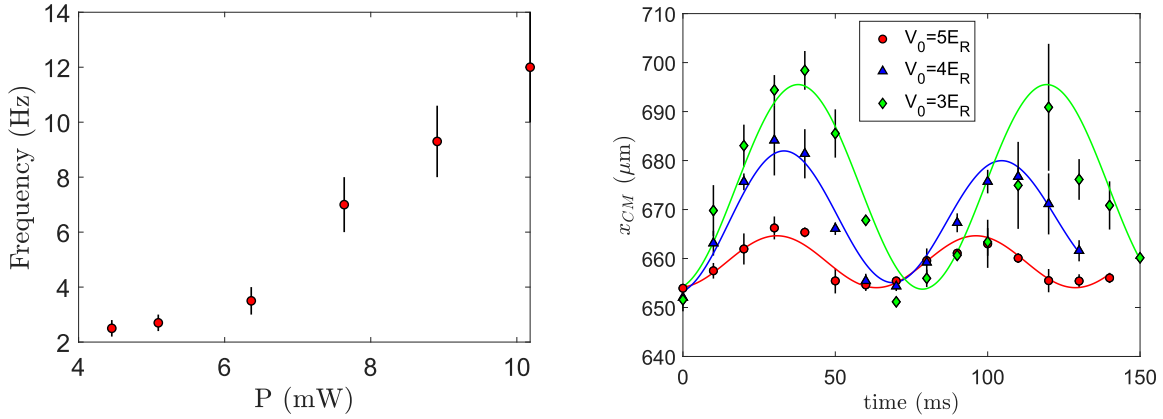

(a) (b)

Figure 4.9: Bloch oscillations inside the primary lattice. a) Bloch frequency as a function of the power of the radial beam. For large value of the optical power, i.e the applied force, the frequency scales linearly. For smaller values the amplitude of the oscillations increases and the cloud moves in region where the force is not constant. In b) I report the time evolution of the center of mass for a fixed value of the force and different values of the lattice depth. The results show a dependence of the frequency on the amplitude.

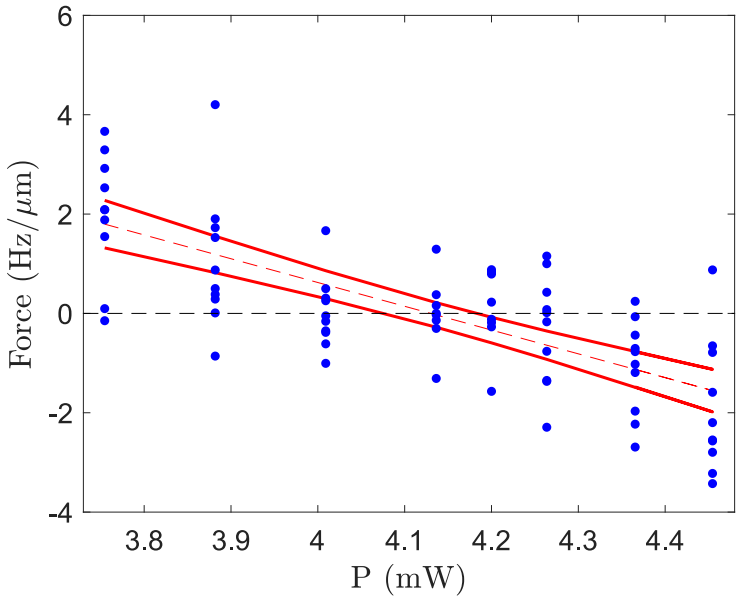

Figure 4.10: Calibration of the local force on the atoms as a function of the optical power of the radial beam. The dots are the data points extracted measuring the position of the cloud after 50 ms of balistic expansion. The dashed line represents the linear fit with the best fit parameters and the solid lines correpond to the 95% confidence interval.

4.3 Coherent dynamics in presence of an external force

The amplitude of Bloch oscillations is proportional to the ratio between the potential energy difference among the sites and the tunneling rate, that depends on the lattice depth and the lattice spacing. The dynamics that we want to observe has a time scale of few Hz. Therefore, in order to achieve a tunneling rate of the same order we need to work with very shallow lattices. In this condition, the energy gap between the two first bands of the BL is very small, of the order of tens of Hz. For this reason, we develope an experimental procedure that can allow to avoid sudden changes in the potential that can lead to unwanted excitations in the upper bands.

4.3.1 Experimental procedure to induce Bloch oscillations

After the evaporative cooling in the dipole trap we ramp up the lattice adiabatically in 300 ms to a lattice depth larger than 200 nK in order to populate only one site, keeping small repulsive interactions that help to evaporate the excitations. Then, we switch off the longitudinal dipole trap slowly and, at the same time, we decrease also the intensity of the radial beam, changing the scattering length to a negligible value. The duration of this step is of the order of hundreds milliseconds. This procedure helps to evaporate excitations that can be still present after the first step. After this second evaporation, we change the power of the radial beam to the working value, setting the total force.

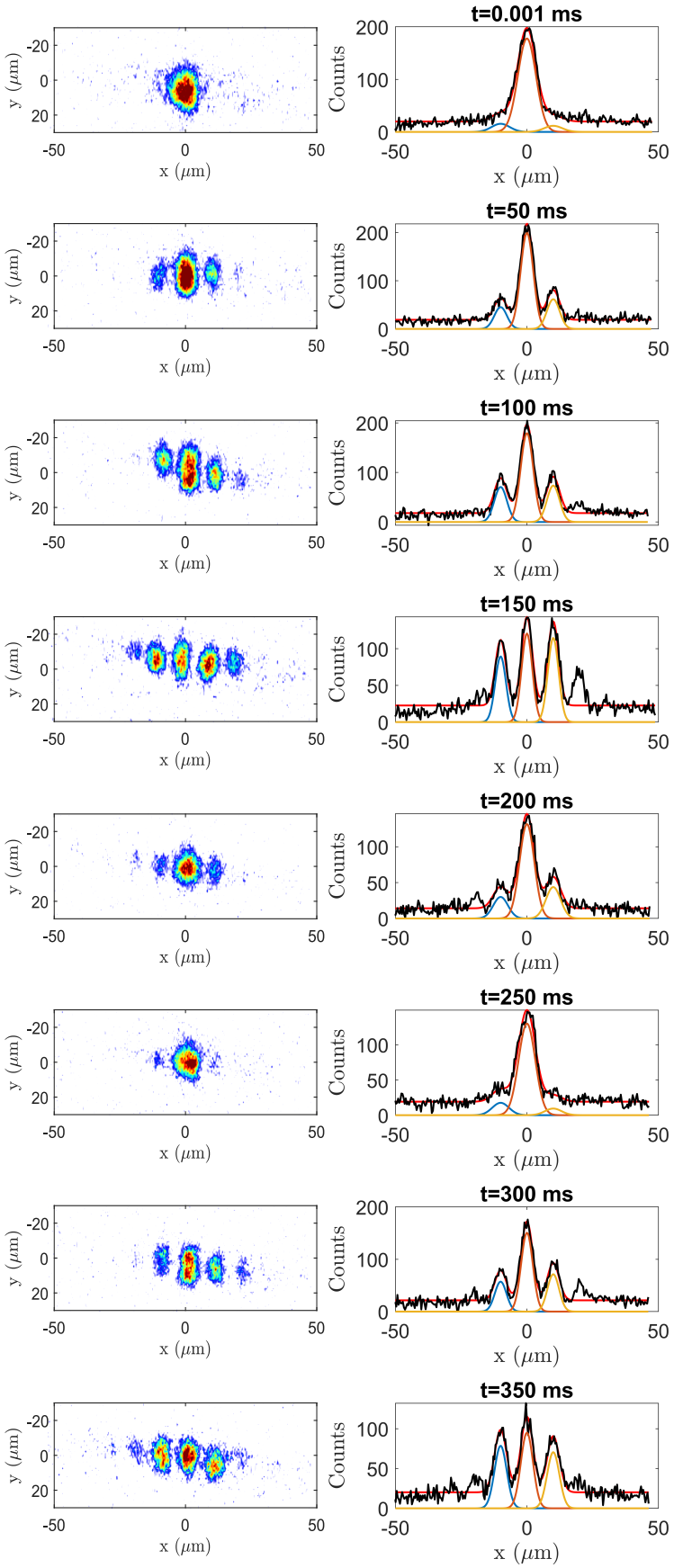

Figure 4.11: In-situ images and correpondent density profile during a Bloch oscillations togheter with the fit performed with a triple gaussian function.

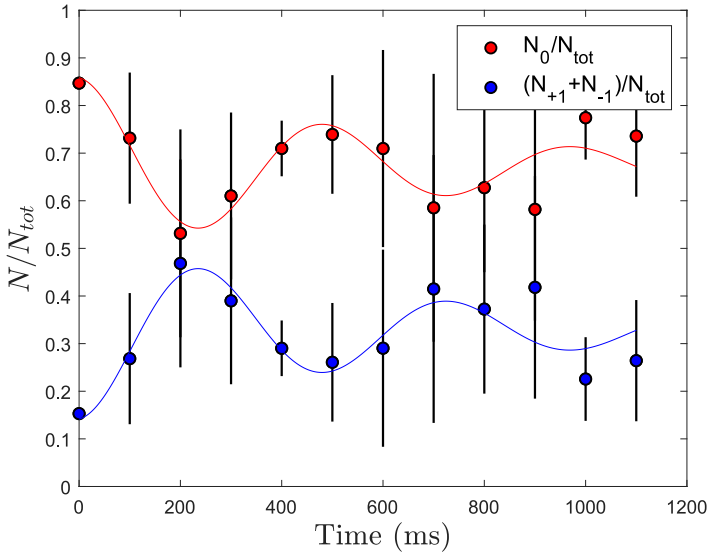

Figure 4.12: Time evolution of the populations in the starting site N_0 and in the neighbouring site $N_{\pm 1}$. The dots are the data and the solid line is a fit performed with a sinusoidal function times an exponential decay. The errors are the statistical uncertainties calculated on 5-6 images recorded for each value of the time.

Finally, we decrease the lattice depth in 50 ms to a value around 70 nK, that correponds to a finite tunneling rate of few Hz. Following the results in Fig. (4.3), the energy gap passes from 100 Hz to 40 Hz, so this time interval is longer enough to ensure an adiabatic tranformation and avoid unwainted excitations. The time scales of the dynamics goes from 1 to 6 Hz, therefore the subsequent oscillation is not significantly modified after the rapid passage. We set $t = 0$ at the end of this ramp. Obviously, mainly when the force is large, the dynamics can already start during the ramp, but this delay corresponds only in a phase shift respect to the starting point. During the oscillation we set the scattering length to a negligible value. According to the stability of the magnetic field and the dependence of a_s on $B($ that is of the order of 0.6 a_0/G), the scattering length is null with an uncertainty smaller than 0.1 a_0.
Following the discussed procedure we manage to observe the time evolution shown in Fig. (4.11), where I report images of the condensate togheter with the spatial density profile integrated in one direction. In order to extract the atom number in each site we fit the profile with a multi-gaussian function. In particular, we are interested in the fraction of atoms that remain in the starting site N_0 and that tunnel in the neighbouring sites $N_{\pm 1}$. In Fig. (4.12) I report an example of the time evolution of the populations. In particular, I show the evolution of N_0 and the sum of N_{+1} and N_{-1}. We fit the data with an exponentially dumped sinusoidal function:

$$f(t) = f(0) + \exp(-t/\tau)\sin^2(\frac{\omega t}{2} + \phi) \tag{4.3}$$

that takes into account the decreasing of the amplitude that we observe. This trend could be caused by different sources. First, fluctuactions of the intensity of the radial beam

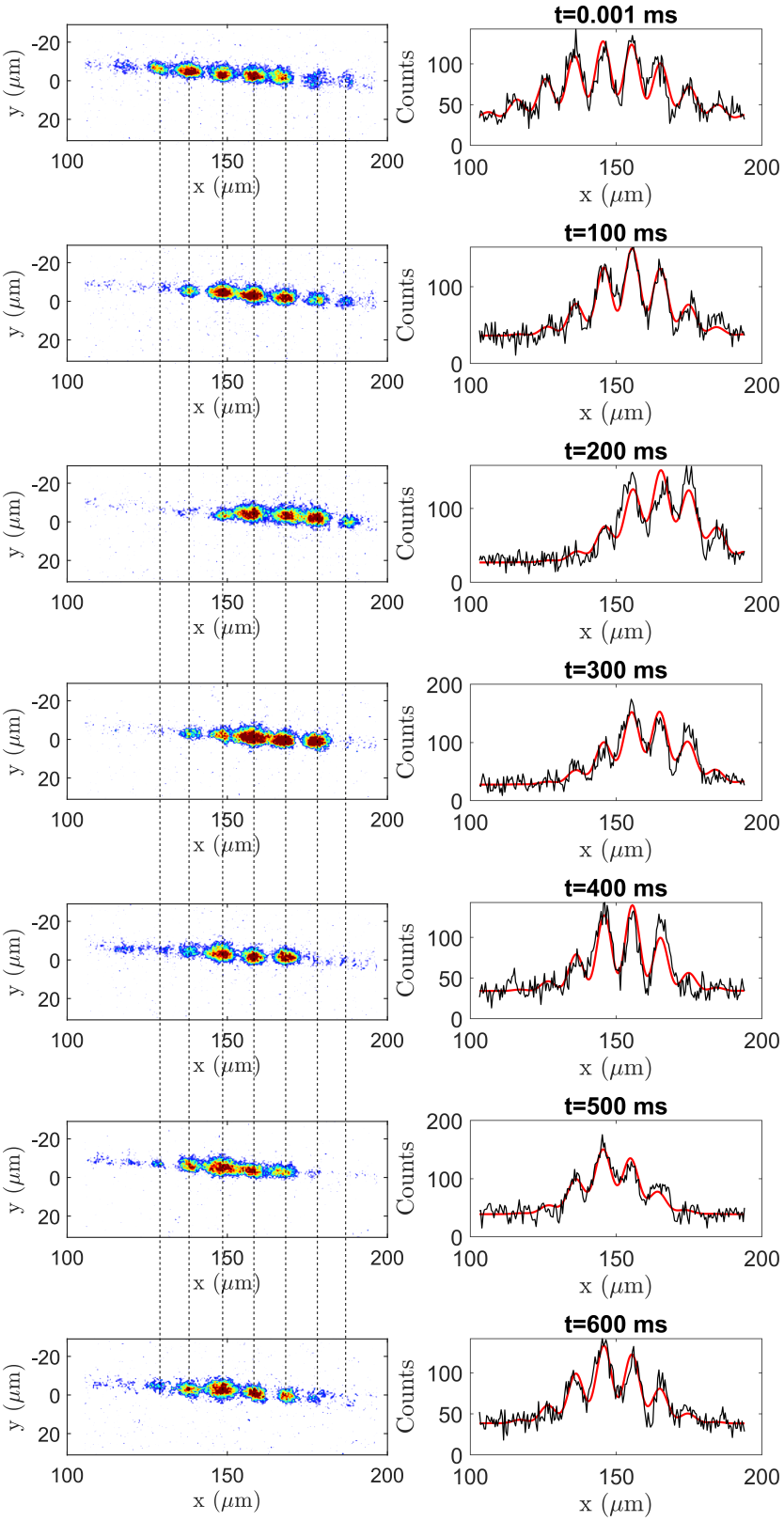

Figure 4.13: In situ images and realtive density profile during a Bloch oscillations togheter with the fit perfomed with a modulated gaussian function. The vertical dashed lines connect the same lattice sites at different time.

and the magnetic residual gradient can introduce excitations with a consequent loss of coherence. Moreover, a non perfect cancellation of the interaction can caused interaction induced decoherence, decreasing the amplitude [48] and reducing the interrogation time. In order to check the latter we plan to observe oscillations with different interaction strength. Finally, phase noise due to vibrations of the retroreflecting mirror and the frequency noise of the lasers can contribute to this effect. However, we measure a 1/e decay time of the amplitude τ of the order of 500 ms that allows an interrogation time up to 1 s. This window is long enough to measure frequencies of 1 Hz.
To our knowledge this is the lowest frequency measured in an interferometric sensor using trapped atoms for the detection of small forces. The state of the art interferometers based on a double well scheme show a coherence time up to 100-200 ms and they are mainly limited by the presence of interatomic interaction [11] and the stability of the optical potential [13]. Note that, in our system, 1 Hz corresponds to a force of 10^{-4} g.
With the discussed procedure we can extract the magnitude of the force. However, since we start from a single site, the center of mass motion of the cloud is frozen. Therefore, in order to gain information about the sign of the force, we repeat the same procedure changing the delay between the switching-off of the longitudinal dipole trap and the increasing of the heigth of the lattice. In this way we load few sites at $t = 0$ and the consequent dynamics is represented by an oscillation of the center of mass. This type of measurement is more sensitive to the spatial dependence of the force, since the cloud is spread over distances larger than 50 μm. However, depending on the sign of the initial velocity we can indentify the sign of the force. As in the previous case, In Fig. (4.13) I report images of the condensate during an oscillation togheter with the integrated spatial density profile. In this case the fit of the density is performed using a gaussian function with an additional modulation:

$$f(x) = \exp\left(-(x - x_0)^2/2\sigma^2\right)\left(1 + A\cos\left(\frac{2\pi}{d}x + \phi\right)\right) \tag{4.4}$$

where σ is the width of the gaussian envelope and d is fixed to 10 μm. We record the center of the envelope x_0 for different time and we obtain the time evolution reported in Fig. (4.14). I show the time evolution of the center of mass for two values of the power of the radial beam that highlight the changing in the sign of the force.

4.3.2 Discussion on the results and comparison with theory

We repeat the same procedure for different values of the applied force, tuning the power of the radial beam. We compare the frequencies measured by Bloch oscillations with the prediction provided by the calibration in Fig. (4.10), where I have converted the values of the force in terms of frequency. As shown in Fig. (4.15) the two set of data are comparable within the error bars and the confidence interval. They show the same dependence on the optical power of the beam, confirming that the observed coherent tunneling is driven by the external force. There is only a small shift that can be caused, for example, by

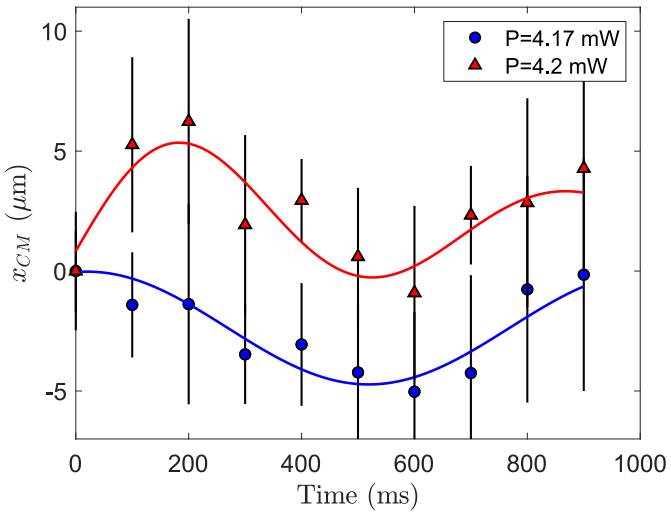

Figure 4.14: Time evolution of the center of mass of the condensate during Bloch oscillations in presence of a force with a different sign.

the presence of some sistematic errors in the measurement of the balistic expansion. An uncontrolled small initial velocity of the order of 0.05 μm/s can explain the observed deviation.

In a Bloch oscillation the amplitude and the frequency are correlated by the tunneling rate. We can create a sort of phase diagram where I report on the x-axis the measured frequency and on the y-axis the measured amplitude (Fig. (4.16)). We observe a sligthly dependence of the amplitude as a function of the applied force. As expected, small forces lead to larger amplitudes. We compare the observed behaviour with the theoretical expectations provided by numerical simulations that take into account the uncertainties in the value of the lattice depth, that goes from 65 nK to 75 nK. The two trends are in qualitatively good agreement excepted for frequencies below 1 Hz or larger than 4 Hz. The presence of residual harmonic potential can modify the amplitude and the frequency. From numerical simulations (for more details see Appendix 1) we observe that our data are comparable with an additional harmonic potential with a frequency of 1 Hz. However, the presence of this curvature does not explain the observed deviation for small frequencies. For an oscillation with a frequency of 1 Hz, the maximum value is reached at 0.5 s that correponds to τ. It means that it is still possible to extract the frequency but the amplitude does not reach its maximum value. Moreover, for such small frequencies the dependence of the amplitude on the force becomes stronger, and fluctuactions in the optical power of the radial beam are more significant.

In conclusion, we observe a coherent tunneling between neighbouring sites of the BL in presence of a small force of the order of 10^{-4} g with a spatial resolution of 10 μm. The results show that, incresing the lattice constant d, the sensitivity can be enhanced and, since the tunneling rate scales quadratically in d, the amplitude of the oscillations can be reduced to few lattice sites. The agreement with theoretical expectations for Bloch

oscillations indicates that the BL behaves as the same way of a single wavelength optical lattice with a spacing of 10 μm. The possibility to exploit retroreflected beams provided by the developed technique allows to achieve a larger stability respect to mechanical fluctuactions in comparison with the common way that is used to increase the lattice constant. The achieved results pave the way to the realization of an interferometer with trapped Bose-Einstein condensates with an unprecedent sensitivity to weak and local forces.

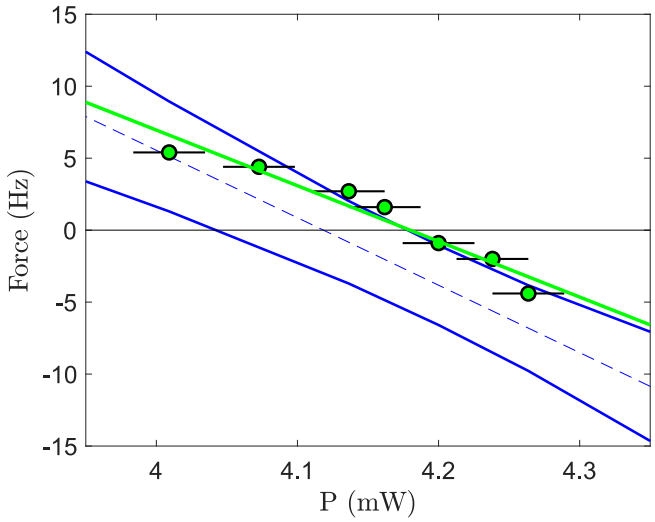

Figure 4.15: Measured frequency as a function of the power of the radial beam. I report the confidence interval of the calibration reported in Fig. (4.10), that shows how the force scales linearly with the optical power. The experimental data shows a linear dependence comparable with the expected behaviour, ensure that the dynamics in the BL is driven the external force. The horizzontal error bars correspond to the uncertainty due to the experimental noise of the electronic circuit for the stabilization of the optical intensity. The vertical bars (not visible) are extracted from the fit of the time evolution.

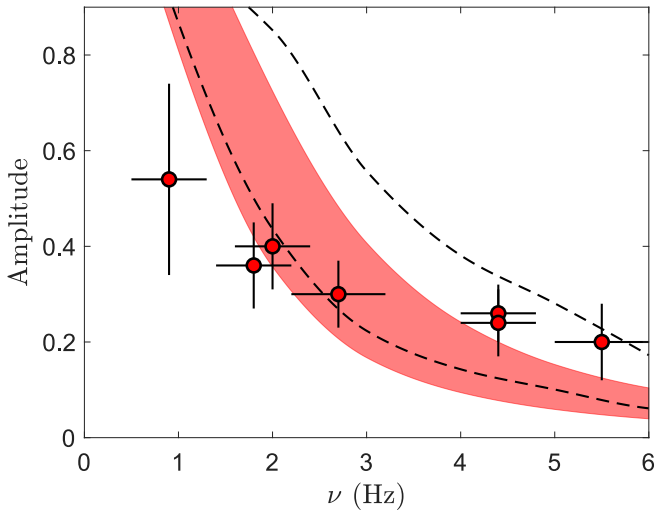

Figure 4.16: Measured amplitude as a function of the frequency. The error bars correpond to the uncertainty of the amplitude and the frequency provided by the fit of the oscillation. The shaded area represents the theoretical expectations provided by numerical simulations taking into acount the uncertainty of the lattice depth from the measurements in Fig (4.3). The dashed lines indicates how the shaded area is modified by the presence of an additional curvature of 1 Hz that can explain the deviation for large frequencies.

4.4 Future improvements

Starting from the results achieved so far, it is possibile to understand which are the crucial aspects of our system that need to be improved in order to enhance its performances. In this final section, I would like to discuss two main important upgrades that we plan to implement in our experimental setup.

4.4.1 A new RF antenna and an additional coil for compensation of the residual gradient

One of the most significant limitation in our apparatus is the presence of a large residual grandient that add an uncotrollable potential. Currently, this force is compensated optically but, in general, it is very difficult to stabilize the optical intensity of a laser beam very well. In our case we extimate that we can control the optical intensity of the radial beam with a relative uncertainty of $5 \cdot 10^{-3}$, that is equal to our current optimal sensitivity. In any case, achieve a stability better than 10^{-3} is very challenging and a different compensation method is needed.
One solution is to place additional magnetic coils in order to create a magnetic gradient along the direction of the lattice. The current that flows in a magnetic coil can be stabilized quite easly with an uncertainty of $10^{-4}/10^{-5}$. The geometrical constraints of our apparatus do not allow to place a pair of coils, that is the best configuration to create a magnetic gradient. Indeed, the combination of the magnetic field produced by coils

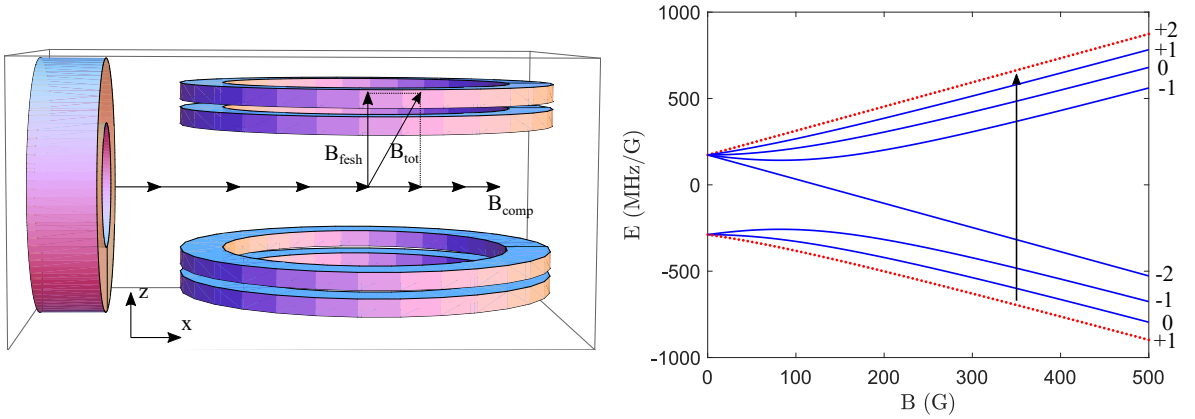

Figure 4.17: a) Sketch of the vertical Feshbach coils togheter with the additional orizzontal coil to compensate the external magnetic gradient. b) Energy of the magnetic sub-levels of the ^{39}K belong to the hyperfine manifolds F=1 and F=2 as a function of the applied magnetic field. The arrows indicates the transition that we plan to exploit to obtain an higher sensitivity in the measurements of residual magnetic gradients.

in anti-Helmholtz configuration, provides a field along the axis that scales linearly as a function of the distance from the center of coil [49].
We are investigating to place a single coil, like sketched in Fig. (4.17). A circular coil with a radius R and a current I provides a magnetic field along it axis [49]:

$$B_{comp}(x) \propto \frac{IR^2}{[R^2 + (A - x)^2]^{3/2}} \tag{4.5}$$

where x is the distance from the center of the coil. The total field is the sum of the additional coil and the bias vertical field provided by the Fesbbach coils. Since the bias field is strong ($\sim$ 350 G) the vertical modulus of the field along z does not change significantly. The presence of the additional field can instead modify the dependence of B in the x-direction. However, since the compensation field is not linear in x, if we manage to compensate locally the external residual gradient we introduce also an harmonic potential. In particular, from numerical simulations based on the geometrical properties of the coil that we want to use, we extimate that, compensating a gradient of 0.1 G/cm, we introduce a curvature of 3 Hz.
A second limitation of our work is the difficulty to measure the force precisely in an indipendent way respect to Bloch oscillations. In section (4.2.1) I have explained that, exploiting transitions between sublevels of the manifold $F = 1$ at 350 G, it is not possible to achieve an high sensitivity, because of the small difference in the magnetic moment. A possibility to increase the resolution is to exploit transitions between a sub-level of the manifold $F = 1$ and an other sub-level of the manifold $F = 2$. In particular, if we produce the condensate in the state $|F = 1, m_F = 1\rangle$ we can be coupled it with an RF pulse with the states $|F = 2, m_F = 2\rangle$. Between the two states there is a difference of the magnetic dipole of about $2\mu_B$, that corresponds to 2.8 MHz/G. Two condensates 100 μm far away

one from the other with a resolution of 0.3 kHz in the measurement of the resonance shifts (like reported in section (4.2.1) at low field) would correspond to a magnetic gradient resolution of 10 mG/cm. For this purpose we are designing a new RF antenna with a resonance frequency around 1.3 GHz that will help to measure and control the external magnetic force acting in the system with higher precision.

4.4.2 The beat-note of three wavelengths

The limited range of parameters that we have explored with the BL is due to the fact that we cannot tune separatly the tunneling and the energy gap because they are both related to the lattice depth.
In general, adding more wavelengths it is possible to engineer the potential with different shape and increase the tunability of the optical potential. In particular we are interested in the realization of an optical superlattice with two periodicities where one is the half of the other. This scheme realizes an array of double-wells that represents the ideal configuration for the realization of a Mach-Zender interferometer with trapped BECs [11]. A sketch of the working principle of such interferometer is reported in Fig. (4.18).
Exploiting the technique of the beat-note it is possible to produce a super-lattice involving only three different wavelengths. In particular if λ_i, with $i = 1..3$ are the wavelengths, the two relations that must be fulfilled at the same time are

$$\begin{cases} (n-1)\lambda_1 = n\lambda_2 \\ n\lambda_2 = (n+1)\lambda_3 \end{cases} \tag{4.6}$$

The two beat-notes $\lambda_1 - \lambda_2$ and $\lambda_2 - \lambda_3$ produce a peridocity of $d_1 = n\lambda_2/2$. Instead the beat-note between λ_1 and λ_3 generate an additional modulation with a periodicity $d_2 = n\lambda_2/4$. In Fig. (4.19) I show the expected potential maintaining $\lambda_1 \sim 1$ μm and $n = 20$ as in the previous discussion. The shape of the potential is an array of double wells with a periodicity of 10 μm for the primary lattice and of 5 μm for the secondary lattice. The energy gap can be modified changing the intensity of the beams with λ_1 and λ_2. The tunneling inside a single double well can instead be tuned indipendently changing the intensity of the lattice at λ_1 or λ_3. Obviously, in this way also the heigth of the barriers at 10 μm changes, but it is possible to compensate the deviation tuning the power of the lattice at λ_2. Changing instead the phase of the lattice at λ_3, it is possible to shift the position of the central barrier and unbalance the energy minima of the two wells, leading to a complete tunability of the optical potential.

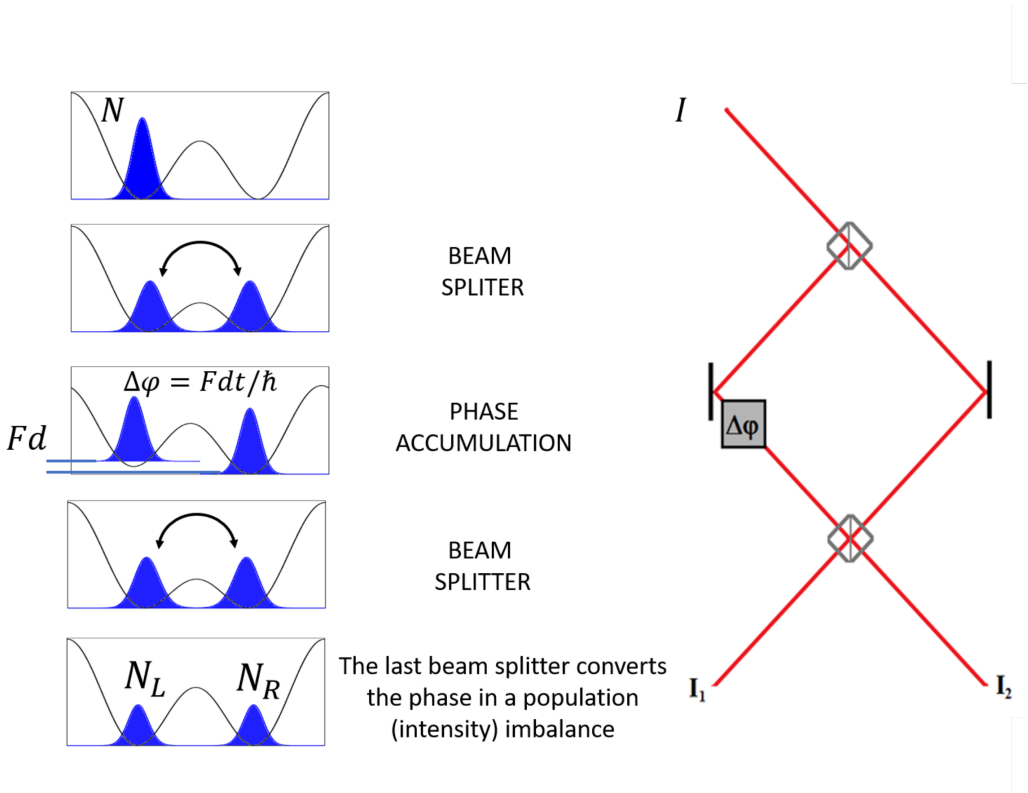

Figure 4.18: (Left) Sketch of the working principle of a Mach-Zender (MZ) interferometer with Bose-Einstein condensates trapped in a double well potential. The three steps are the first splitting, the subsequent phase accumulation and the final recombination. An external force causes an energy difference between the two wells Fd that is converted in a phase difference $\Delta\varphi = Fdt/\hbar$, where t is the interrogation time. At the end of the sequence, the information about the phase are converted in an atomic imbalance. (Right) A skecth of a MZ interferometer exploiting light waves shows the complete equivalence between the two schemes.

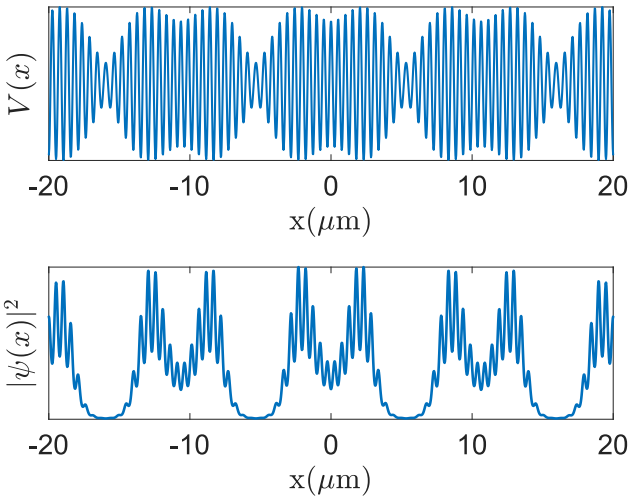

Figure 4.19: Spatial profile of the resulting potential of the beat-note between three wavelengths(above) and the correspondent ground state wave-function (below).

Chapter 5

Conclusions and perspectives

In conclusion, in this thesis I report the realization of a large spacing optical lattice exploiting the beat-note of two retroreflected laser beams with slightly different wavelengths, i.e 1064 nm and 1013 nm. The resulting potential, in addition to a very fast modulation, exhibits a slow periodicity that provides an optical potential for the atoms that behaves like an effective lattice with a 10 μm separation between the lattice sites.
I studied theoretically the band structure of the new lattice and I performed numerical simulations in order to obtain predictions of the energy gap as a function of the lattice depth in different configurations. I observed a maximum values of the achievable gap that depends on the wavelengths of the radiation that are used to realize the beating. The existance of this maximum is related to the tunneling rate inside the primary lattice. When the lattice depth becomes too large the wavefunction starts to localize inside the wells of the primary lattice and the BL stops to work as an effective large spacing optical lattice.
Regarding my experimental contribution, I showed the laser setup that I have designed and assembled for the production and the control of the optical potential on the atoms. In particular, I reported in details the methods that we exploit to lock the two frequencies at the same optical cavity in order to reduce relative frequency fluctuactions.
Thanks to the capability to cancel the interatomic interactions using magnetic Feshbach resonances, we have managed to observe spatial Bloch oscillations of condensates, measuring the atom number in each well. The observed dynamics exhibits a coherence up to 1 s that correponds to a sensitivity of the order of $5 \cdot 10^{-5}$ g with a spatial resolution of ten microns. We characterized experimentally the frequency and the amplitude of the oscillations for different values of the force and the results show a good agreement with theoretical simulations. To our knowledge the sensitivity acquired in this work is the higher reported in litterature in the measurement of small forces ($<< g$) using a trapped atom interferometer. The main limitations to the coherence time and the precision of the measurements are related to the limited control we have in the way we tune the external force, i.e, optically.
The simplicity of the Bloch oscillation interferometer and the creation of a large spac-

ing periodic potential open interesting perspective in the measurements of small forces with trapped condensates. They can be exploited, for example, for the investigation of Casimir-Polder forces or deviations of the gravitational law at short distances.

Chapter 6

Self-bound quantum droplets of ultracold atomic mixtures

Even if I have dedicated this thesis to the project on the new optical lattice, in this final chapter I report a summary of our experimental investigation about quantum droplets in ultracold bosonic mixture, that we carried on in the first half of my PhD.
Ultracold atomic systems are commonly found in a gas phase. However, self-bound quantum droplets have been recently theoretically predicted [50] and experimentally observed [51, 52, 53, 54] as a new liquid-like phase in this context. At the origin of this new phase there is the coexistence of repulsive and attractive forces that perfectly balance to generate the self-binding mechanism. In particular, in bosonic mixture, droplets form due to the balance of the attractive mean-field energy close to the collapse threshold and the repulsive first-order correction due to quantum fluctuations, the so-called Lee-Huan-Yang term [55]. This stabilization mechanism generated by the LHY correction has been recognized as responsible also for the formation of a different class of self-bound quantum systems, i.e., dipolar droplets [51, 52]. While attractive mixtures create spherical droplets, in dipolar gases droplets are elongated along the dipole direction and strongly anisotropic. The different geometry, together with the different kinds of interactions governing the stabilization, leads to important differences in the properties of the two objects and enriches the range of phenomena that can be explored.
Self-bound droplets have been observed in bosonic mixtures only in confined geometries [53, 54]. In this chapter I describe our experimental observation of self-bound droplets in an atomic mixture in free space. Two are the main ingredients of our work: the capability to tune the interatomic scattering lengths exploiting magnetic Feshbach resonances to reach the interaction regime where the mixture is predicted to be self-bound; the implementation of an optical levitating potential with negligible residual confinement along all directions, which allows us to have long interrogation times and access the droplet properties in free space. The most peculiar feature of quantum droplets realized with bosonic mixture in free space is related to its excitation spectrum. In a specific region of the droplet phase diagram, the particle emission threshold is predicted to lie below any

possible excitation mode [50]. Any excess of energy is thus expelled by losing particles, leading to an effective self-evaporation and keeping the droplet at zero temperature.
I start presenting a brief summary of the theoretical description of quantum droplets and then I explain how we create and observe them experimentally. I present in more details the properties of the optical levitating potential and the imaging technique that we have exploited. I present our experimental results and the comparison with the theoretical predictions. Finally, I show our research about collisions between two droplets. The dynamics of the collision could be useful to gain informations about the liquid-like nature of the droplet and the typical energy scales.

6.1 Theory of quantum droplets

I first introduce the theoretical description of the self-binding mechanism that generates droplets, starting from the case of a single condensate and then extending the theory to a bosonic mixture.

6.1.1 Beyond mean-field description: Lee-Huang-Yang correction

In the second quantization approach, the many-body Hamiltonian operator of N bosons in the external potential $V_{ext}(\vec{r})$ is:

$$\hat{H} = \int d^3r \hat{\Psi}^\dagger \left[-\frac{\hbar^2 \nabla^2}{2m} + V_{ext}(\vec{r}) \right] \hat{\Psi} + \frac{1}{2} \int d^3r d^3r' \hat{\Psi}^\dagger(\vec{r}) \hat{\Psi}^\dagger(\vec{r}') V_{int}(\vec{r} - \vec{r}') \hat{\Psi}(\vec{r}) \hat{\Psi}(\vec{r}') \quad (6.1)$$

where the field operator $\hat{\Psi}(\vec{r})$ is defined by:

$$\hat{\Psi}(\vec{r}) = \sum_i \psi_i(\vec{r}) a_i \quad (6.2)$$

and a_i is the single particle destruction operator of the i-th state described by the wavefunction $\psi_i(\vec{r})$ and $\int |\hat{\Psi}|^2 d^3x = N$. Because of the very small collisional energy, for ultracold bosons it is possible to assume that the physics of the interactions is dominated by the s-wave scattering and the two-body interaction V_{int} can be described by an effective contact potential $V_{int} \sim g\delta(\vec{r} - \vec{r}')$ where the strength of interactions is $g = 4\pi\hbar^2 a_s/m$, proportional to the the s-wave scattering length a_s. Assuming that the cloud is all condensed in the ground state we can substitute the field operator with a c-number. This approximation corresponds to neglect a term $\delta\hat{\Psi}(\vec{r}, t)$ (that takes into account quantum fluctuactions) in the field operator and write:

$$\hat{\Psi} = \sqrt{N_0}\Psi_0(\vec{r}, t) + \sqrt{N - N_0}\delta\hat{\Psi}(\vec{r}, t) \simeq \sqrt{N_0}\Psi_0(\vec{r}, t) \quad (6.3)$$

where N_0 is the number of atoms in the ground state and Ψ_0 is the wavefunction of the condensate. Substituting the ansatz (6.3) in the Hamiltonian (6.1) one obtains the so

called Gross-Pitaevskii equation [56] that leads to the energy functional with the non-linear term:

$$E[\psi] = \int d^3r \left[N\frac{\hbar^2}{2m}|\nabla\psi(\vec{r})|^2 + NV(\vec{r})|\psi(\vec{r})|^2 + \frac{1}{2}N^2 g|\psi(\vec{r})|^4 \right] \tag{6.4}$$

This approximation can describe many properties of the condensate but it assumes that all the particles are in the ground state of the system. This is not really true, because in an interacting condensate there is always a certain amount of particles that are not in the lowest energy state that is called quantum depletion. The atoms in the condensate collide and so they couple to the excited states. This interaction causes a shift in the energy of the condensate. In order to take into account this contribution, one needs to consider the term neglected in the field operator in (6.3). Substituting the complete expression for the field operator in the Hamiltonian (6.1) and neglecting the second order terms in $\delta\hat{\Psi}$, the total energy of the ground states becomes [57]

$$E_0 = \frac{1}{2}gnN + \frac{1}{2}\sum_{k\neq 0}\left[\epsilon(k) - g_o n - \frac{\hbar^2 k^2}{2m}\right] \tag{6.5}$$

where $\epsilon(k)$ is the famous Bogoliubov dispersion law [56]. Considering finite range contributions in the interactions in addition to the contact one, the energy per unit of volume can be written as [57]:

$$E_0/V = \frac{1}{2}gn^2\left[1 + \frac{128}{15}\left(\frac{na^3}{\pi}\right)^{1/2}\right] + ... \tag{6.6}$$

The energy of the ground state at zero order is given by $E_0 = 1/2gn^2$ and corresponds to the mean-field approximation. The first order correction of the energy of the ground states gives a term proportional to $n^{5/2}$ that is known as the first order Lee-Huang-Yang (LHY) term [55].
Usually in a single species condensate the LHY term is orders of magnitude smaller than the mean-field energy and it can be neglected. Despite the LHY correction is very difficult to measure, experimental observation have been made so far using the equation of state of an unitary Bose gas [58] or probing the system with RF spectroscopy [59, 60, 61, 62].

6.1.2 Bosonic mixtures

While in a single-species condensate both the MF and the LHY term depend on the same parameter a, a different situation occurs in a Bose-Bose mixture, formed by atoms of two different species, 1 and 2, which can be different atoms, different isotopes of the same atom, or atoms of the same isotope but in different hyperfine states. In the case of a mixture the interactions are described by different parameters: the intraspecies scattering lengths a_{11} and a_{22} and the interspecies scattering length a_{12}.
Let us consider the case of equal masses $m_1 = m_2$ and define the coupling constants as

$g_{ij} = 4\pi a_{ij}/m$, while n_1, n_2 are the densities of the two species. Following this notation the ground state energy for the mixture in the mean-field approximation is:

$$E_{MF} = \int_V d^3r \epsilon(n_1(\vec{r}), (n_2(\vec{r})) \tag{6.7}$$

where

$$\epsilon = \frac{1}{2}(g_{11}n_1^2 + g_{22}n_2^2) + n_1 n_2 g_{12} \tag{6.8}$$

Depending on the magnitude and sign of the three interactions, such energy functional describes different behaviours. In particular, in the case of repulsive intra-species interactions ($g_{11} > 0$, $g_{22} > 0$) and attractive inter-species interaction ($g_{12} < 0$), the mixture is thus stable according to the MF theory if:

$$\delta g = \sqrt{g_{11}g_{22}} + g_{12} > 0 \tag{6.9}$$

If instead $\delta g < 0$, which means that the mixture is globally attractive, according to the mean-field picture, the double BEC should collapse.
However, so far we have not considered beyond mean-field corrections, which will play an important role in the stability of the mixture. When the two species have the same density distribution, modulo a scale factor α (corresponding to different atom numbers $n_2 = \alpha n_1 = \alpha n$) and the system is close to the mean-field collapse threshold, one can further simplify the above expression by setting $g_{12} \simeq g_{11}g_{22}$ and neglecting small finite-δg corrections. In this regime, the interaction energy of the mixture, including the LHY term, can be written as the sum of two main contributes [50]:

$$E_{int} \simeq -2|\delta g|n^2 + f\left(\frac{\delta g}{g}\right)(gn)^{5/2} \tag{6.10}$$

Eq. (6.10) shows explicitly the competition between two contributions with different signs: the mean-field attractive interaction and the effective repulsion due to the LHY correction. Usually, the prefactor f is small and the second contribution is negligible. However, in the regime where the droplet forms $|\delta g| \to 0$, which means that the mean-field energy becomes smaller while the LHY repulsion ($\propto g^{5/2}$) does not vanish and the two terms become comparable. Finally, the different scaling as a function of the density leads to the interaction energy functional shown in Fig. (6.1): while the negative MF contribution leads to an increase of density and eventually to collapse, the presence of the LHY term generates a minimum for a finite value of the size that fixes the density of the droplet in absence of an external confinement.

6.1.3 Properties of the quantum droplet

The properties of the droplet depend on the number of atoms in the mixture and on the interaction strengths. At equilibrium the droplet is characterized by a well-defined ratio between the number of atoms in the two species that is fixed to [50]:

$$\frac{N_1}{N_2} = \sqrt{\frac{g_{22}}{g_{11}}} \tag{6.11}$$

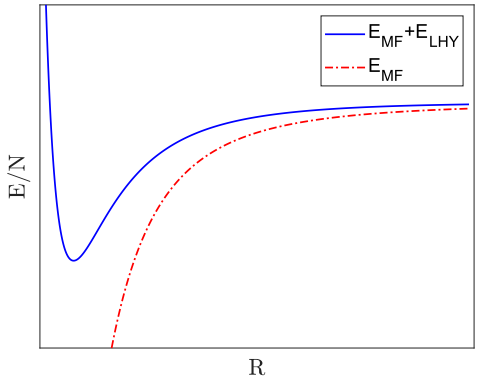

Figure 6.1: The energy of an attractive mixture ($\delta g < 0$) is represented as a function of the size of the atomic cloud R, for a fixed atom number N. The various terms contributing to the energy are the kinetic energy E_{KIN}, the MF interaction energy E_{MF} and the LHY contribution E_{LHY}. If only the first two are present, the minimum of E is for $R \to 0$, corresponding to collapse. Instead, thanks to the LHY term, the minimum occurs at a finite value of R, indicating the formation of a self-bound droplet.

that minimizes the mean field energy E_{MF}. Since the ratio is fixed, the wavefunction of the two components in the ground state can be written as $\psi(\vec{r},t) = \sqrt{n_i^{(0)}}\phi(\vec{r},t)$, where $\phi(\vec{r},t)$ is a scalar wave function and $n_i^{(0)}$ is the equilibrium density of the species i, that depends only on the scattering lengths. In the following discussions, all the quantities of interest will be rescaled using adimensional units. In rescaled units, the atom number $\tilde{N}$ is defined by the normalization condition

$$\tilde{N} = \int_V d^3\tilde{r}|\phi|^2 \tag{6.12}$$

with $\tilde{r} = r/\xi$, where ξ is a characteristic length scale of the droplet [50]:

$$\xi = \sqrt{\frac{3}{2}\frac{\sqrt{g_{22}}/m_1 + \sqrt{g_{11}}/m_2}{|\delta g|\sqrt{g_{11}}n_1^{(0)}}} \tag{6.13}$$

and $\tilde{N}$ is related to the number of atoms in the two components at equilibrium by $N_i = n_i^{(0)}\xi^3\tilde{N}$.
By studying the dependence of the energy of the droplet on the rescaled particle number $\tilde{N}$ it can be shown that, for decreasing $\tilde{N}$, the energy minimum at finite size first becomes metastable and then, over a certain critical number $\tilde{N}_c$, it disappears. The kinetic energy prevails and the system enters in a gas phase, expanding freely like a gas (Fig. (6.2)). When the atom number is sufficiently large respect to the critical number (Fig. 6.3) the droplet develops instead a constant bulk density, highlighted by the central flat region of the wavefunction. This recalls the behaviour of a liquid, thus pointing out the first interesting feature of these quantum droplets, which behave as a dilute liquid phase.
Another peculiar feature of the quantum droplet is related to its excitation spectrum [50], which is shown in Fig. (6.4). As one can see there is an interval of the atom number,

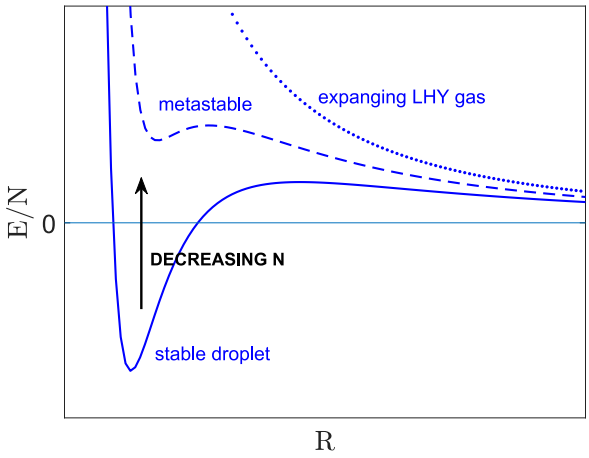

Figure 6.2: For decreasing atom number the energy minimum becomes first metastable (the global ground state corresponds to $r \to \infty$), and then disappears completely if $N < Nc$, where the phase of the system becomes an expanding gas.

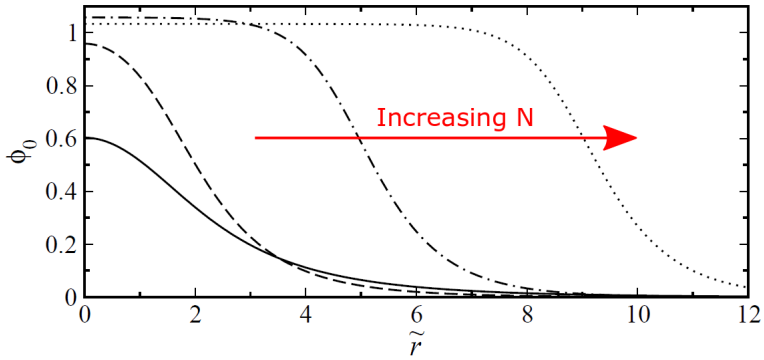

Figure 6.3: Droplet ground-state wave-function ϕ_0, as calculated by Petrov in [50], for different values of the rescaled atom number $\tilde{N}$. While for large atom number $\tilde{N}$ we can distinguish a bulk part having constant density and a surface part where the density decreases, for small $\tilde{N}$ the size of the droplet is comparable with its surface thickness.

in the range $20.1 < \tilde{N} < 94.2$, where no excitation modes below the emission treshold $-\tilde{\mu}$ can be excited. In this interval, exciting the droplet leads to a loss of particle or a breaking of the cloud in smaller droplets. This peculiar behaviour makes the droplet an effectively "zero-temperature" object.

6.2 Experimental observation of quantum droplets in free space

Experimentally we create self-bound droplets using two hyperfine states of ^{39}K, namely, $|F = 1, m_F = 0\rangle$ (state 1) and $|F = 1, m_F = -1\rangle$ (state 2). As I have explained before, Feshbach resonances allow us to tune the mutual contact interactions as a function of the

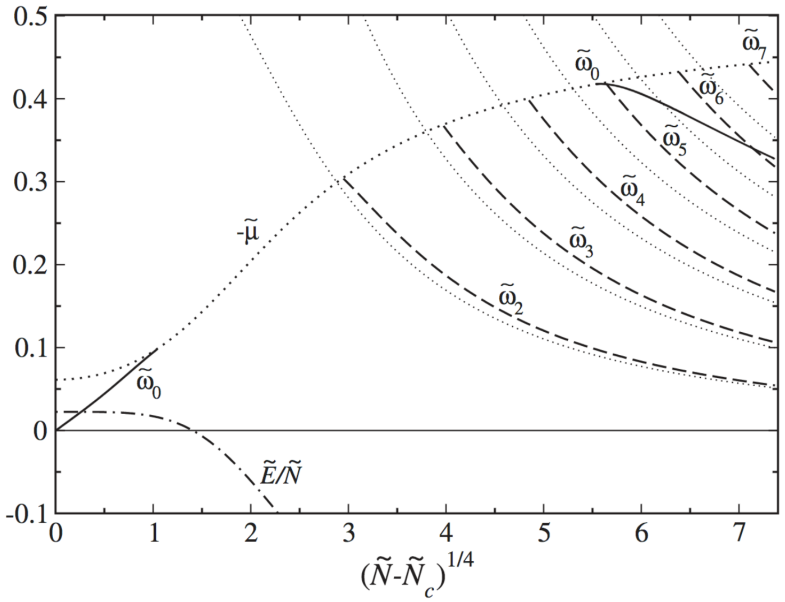

Figure 6.4: Energy per particle (dash-dotted line), particle emission threshold $-\tilde{\mu}$ (dotted), monopole frequency ω_0 (solid line) and frequencies of higher order modes as a function of $(\tilde{N} - \tilde{N}_c)^{-1/4}$, reported by Petrov in [50]. In the interval $20.1 < \tilde{N} < 94.2$ all the excited modes lie above the particle emission threshold.

magnetic field B. Fig. (6.5a) show that for these two states there is a certain region of the magnetic field where the scattering lengths a_{11} and a_{22} are both positive, while the interspecies a_{12} is negative. Considering the effective interaction δa, it becomes negative for $B < B_c$, where $B_c = 56.85$ G, setting the threshold for collapse of the BEC in the usual MF picture. The LHY term, however, determines a stabilization mechanism that prevents the collapse, depending on the atom number. If the atom number is above the critical value N_c the phase of the system is a liquid-like self-bound droplet that does not expand in free space (blue region in Fig (6.5)). Otherwise, if the atom number is below the critical value the system is an expanding LHY gas (light blu region in the diagram).

6.2.1 Experimental sequence for the production of a single droplet

We prepare the BEC in state 2, in a crossed dipole trap, created by three red-detuned laser beams (see Fig. (6.6a)), with almost isotropic trapping frequencies of the order of 200 Hz and up to $400{\cdot}10^3$ atoms. After we have ramped the value of the magnetic field to the desired target value, we apply a radio-frequency (RF) pulse to transfer 50% of the atoms in state 1.

In order to observe the subsequent evolution for sufficiently long times, remaining within the field of view of our imaging system, gravity compensation is required. Since the two states have different magnetic dipole moments we cannot use the standard magnetic levitation technique common in ultracold atomic systems. We have developed a novel optical levitating potential, that I'll describe briefly in session 6.2.2. In particular I focus on

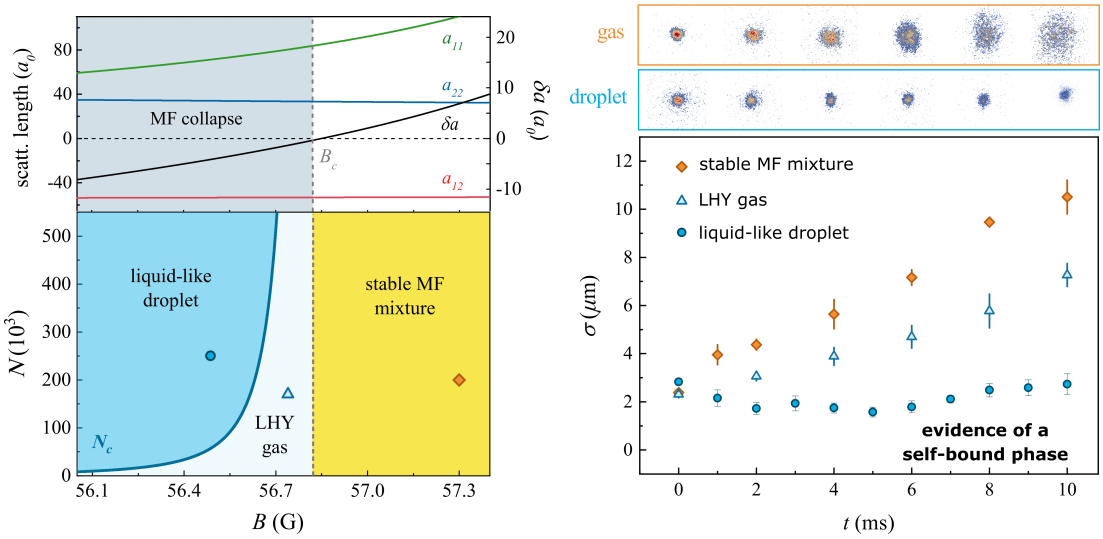

(a) (b)

Figure 6.5: a) (Top) Feshbach resonances relative to the intra- and interspecies scattering lengths for atoms in the hyperfine states $|1,-1\rangle$ (state 2) and $|1,0\rangle$ (state 1) of ^{39}K, tuned by an external magnetic field B. The MF energy of the mixture depends on the effective scattering length δa, which vanishes at Bc = 56.85 G. (Bottom) Phase diagram for the mixture as a function of the atom number N and of the magnetic field B. For $B < B_c$ the mixture would collapse according to the MF picture. The LHY term, however, determines a stabilization mechanism that prevents the collapse: depending on the atom number, the phase of the system is either a liquid-like self-bound droplet (blue region of the diagram), or an expanding LHY gas. b) The upper rows show the difference in the evolution of the density profiles in the gas and droplet cases. In the graph the time evolution of the average size of the atomic cloud is shown, for three different points in the phase diagram: gas, liquid-like droplet and LHY gas.

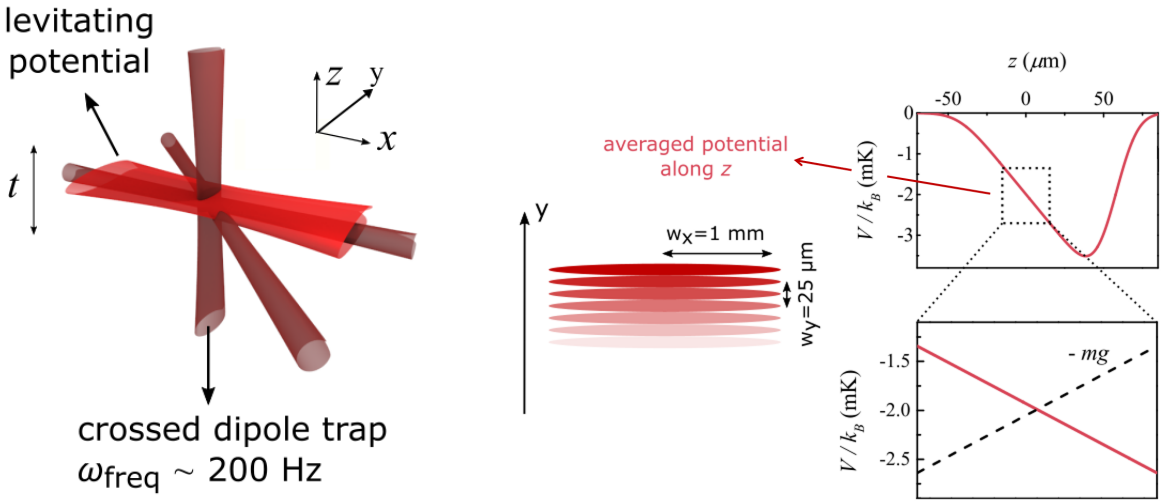

(a) (b)

Figure 6.6: a) Schematic representation of the geometry of the optical trap. b) The modulation of the position of an elongated red detuned beam along the vertical direction (y) provides a time average potential (above). Near the atomic position the resulting profile is linear and compensates the gravity (below)

my personal contributes to the understanding of the effect that this potential has on the atoms (for more details see [26, 63]).
At the end of the RF pulse, we switch off the dipole traps and switch on the levitating potential and, after a variable waiting time, we record the density profile of the cloud via absorption imaging. Fitting the density profiles with a gaussian function we measure the size of the clouds. In order to characterize the droplet phase, we also perform measurements of the total atom number and of the relative population in states 1 and 2. After a variable time, we perform a Stern-Gerlach separation of the two components, by applying a magnetic field gradient along the vertical direction z, so that we can count separately N_1 and N_2.

6.2.2 Effect of the modulation on the atoms

The main requirement for the levitating potential is to not provide any significant confinement to the atomic cloud. In order to distinguish droplets from standard gaseous mixtures, we want indeed to verify their self-bound nature in absence of external confining potentials. Using a single gaussian laser beam would require a very broad beam profile and, hence, a very large power. We then decided to make use of a time-averaged potential. Modulating periodically in time the position of a laser beam, one can indeed generate an arbitrary time-averaged intensity profile. If the modulation period is much smaller than the typical time scale for the dynamical evolution of the atoms, they do not distinguish the fast dynamics of the modulated potential, but they are only sensitive to the time average.
In particular the vertical position of a red detuned elliptical laser beam is modulated in time with an acousto-optical modulator, such that the averaged potential experienced by the atoms provides a gradient opposite to gravity (Fig. (6.6b)). The minimum modulation frequency is set by the timescales of the density oscillations of the cloud in the unmodulated beam, which are determined by the trapping frequency. In order to be more quantitative in the lower-bound limit of the modulation frequency, I have performed numerical simulations of a non interacting BEC in the time-averaged optical potential where I have studied the micro-motion and the heating of the cloud for different modulation frequencies. The first parameter is related to the position of the cloud while the second to its size. The time evolution of these two quantities is shown in Fig. (6.7): both effects are negligible for modulation frequencies larger than 1 kHz, which sets a lower bound. On the other side, while one would say that the best option is to modulate as fast as possible, we need to consider some technical limitations to the maximum reachable frequency. They are related to the frequency bandwidth of the AOM driver (in particular of the internal VCO) and to the finite bandwidth of the intensity stabilization feedback loop. In our case we measure that the global bandwidth ν_0 is about 100 kHz. If the modulation of the voltage has some Fourier components at frequencies larger than ν_0, the shape of the optical averaged potential is affected. By the help of numerical simulations, we can calculate the effect of a low pass filter with a cutoff frequency of ν_0 on the shape of potential. From

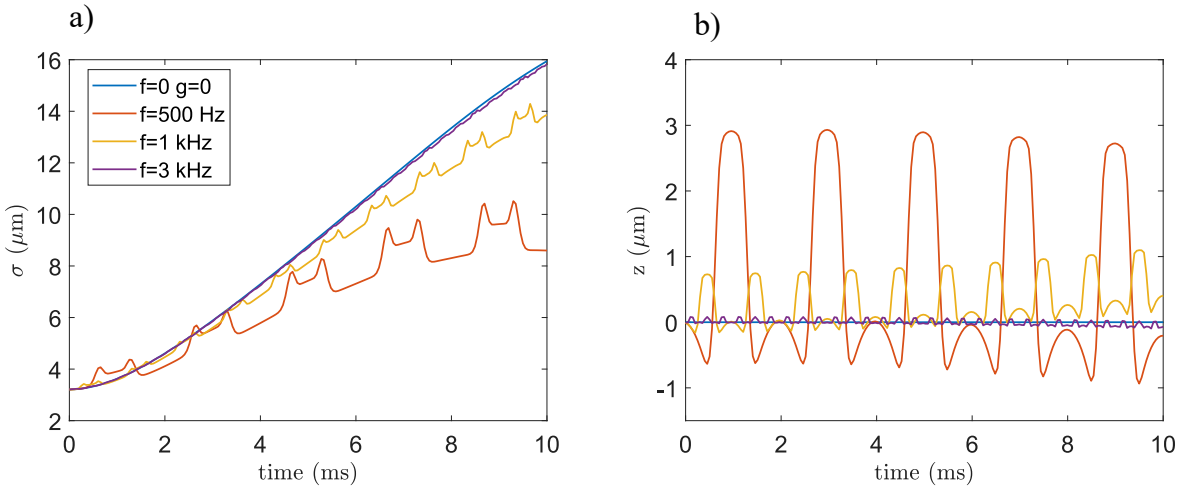

Figure 6.7: Numerical simulation of the micro-motion (a) and size (b) of a not interacting BEC inside the time-averaged optical potential, for different values of the modulation frequencies.

some measurements of the intensity profile of the beam acquired with an auxiliary CCD (for details see [63]), we find out that the upper bound is 5 kHz and therefore we set the frequency to 3 kHz.
The levitating beam has a large waist on the horizontal direction (y) in order to guarantee negligible residual curvatures on all directions. In order to measure the residual curvature, we compare the evolution of a Bose-Einstein condensate at $7.5a_0$ in the levitating potential and in free space. In Fig. (6.8) I show the time evolution of the measured Thomas-Fermi radius R_z of the cloud along z. The two datasets corrrespond to the expansion in free-fall (purple) and in the levitating potential (orange). We compare them to the theoretical curves corresponding to the expansion of the BEC in free space and in a harmonic confining potential $V(z) = \frac{1}{2}m\omega_z^2 z^2$. When R_z becomes larger than 30μm, we see a deviation from the free-space expansion, which is compatible with the evolution of the BEC with $\omega_z = 2\pi \times 12$ Hz. This measurement is mostly sensitive to the curvature at large distance and it also provides only an upper bound to the effective confinement experienced by the droplets around $z = 0$. Finally, note that the sizes of the droplets we observe are always isotropic along the two measured directions, togheter with the fact that we do not observe any deformation of the droplet from its predicted spherical geometry let us conclude that the effect of the levitating potential is negligible also on the vertical direction.

6.2.3 Switching-off of the magnetic field

As already mentioned in the chapter 2, in order to perform absorption imaging we need to switch off the magnetic fields, so that both hyperfine states composing the droplet become resonant with the imaging light.
Switching off the magnetic field requires a certain time before the current in the magnetic coils stops to flow. During the switching-off of the magnetic field the inter and intra-species scattering length in the mixture change Fig. (6.9) due to the presence of Feshbach

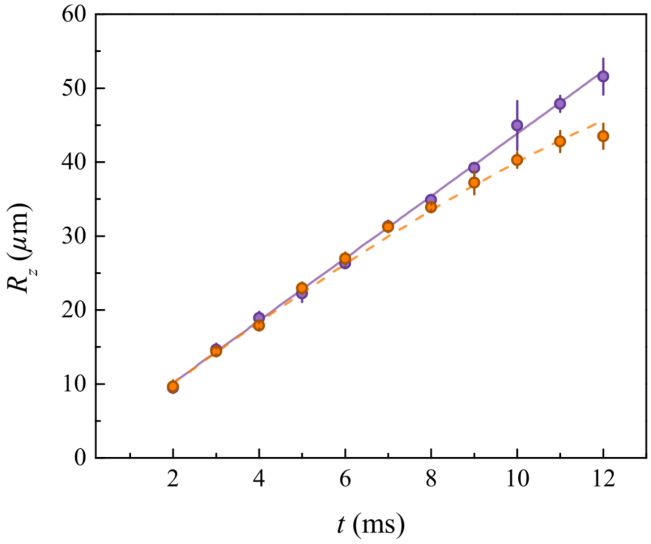

Figure 6.8: Expansion of a BEC in the levitating potential (orange dots) vs free space (purple dots). We measure the Thomas Fermi radius along the vertical direction after releasing a BEC from its dipole trap. The purple points correspond to the free-space evolution, while the orange ones to the expansion in the levitating potential. The theoretical curves are the result of the evolution calculated from the Gross-Pitaevskii equation in free-space (solid purple) and with a vertical confinement of 12Hz (dashed orange)

resonances, leads to a change in the size of the cloud. We optimized the experimental setup, identifying and removing the major sources of induced currents. This allowed us to implement an experimental sequence where the time required to switch off the magnetic field is reduced to $t_{switch} \sim 80$ μs.

As shwon in Fig. (6.9a) the scattering length of the state 2 a_{22} diverges at a Feshbach resonance around $B \sim 35$ G, while the scattering length a_{11} of the state 1 decreases from a positive value to a negative one. In order to better understand the effect of the changing in the scattering length,I have performed a numerical simulation of the evolution of a BEC mixture for different values of the parameter N_1/N_{tot}. The results are shown in Fig. (6.9b). The major effect on a cloud mostly in the state 1 ($N_1/N_{tot} \sim 1$) is a contraction of the size, in agreement with the fact that the scattering length of the majority of the atoms is negative for a long fraction of the evolution time. On the contrary, when the mixture is mainly made by atoms in state 2, a rapid expansion of the cloud is observed, starting at the time corresponding to the crossing of the resonance in the scattering length, where the atoms experience a very strong repulsive interaction. For intermediate values of N_1/N_{tot} as those typical of the droplet there is a compensation of the two effects and we observe only a small variation of the size.

Finally, in Fig. (6.10) I report the simulated size after 80 μs and after 500 μs, for various values of N_1/N_{tot}, and I compare the results of the simulations with the experimental measurements. Despite the numerical simulations are based on a simplified model, neglecting for example density-dependent effects tha could be relevant near the resonance, a qualitative agreement is anyway achieved. We conclude that performing the imaging

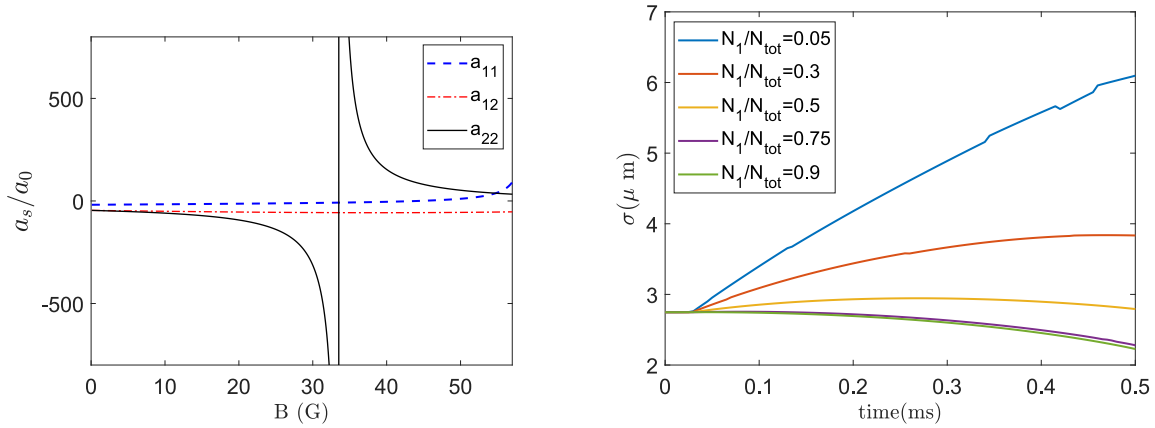

Figure 6.9: a) Scattering lengths in the range of magnetic field that the atoms explore during the switching off. (b) Corresponding evolution of the size of the atomic cloud, for different values of N_1/N_{tot}, as obtained from the simulations.

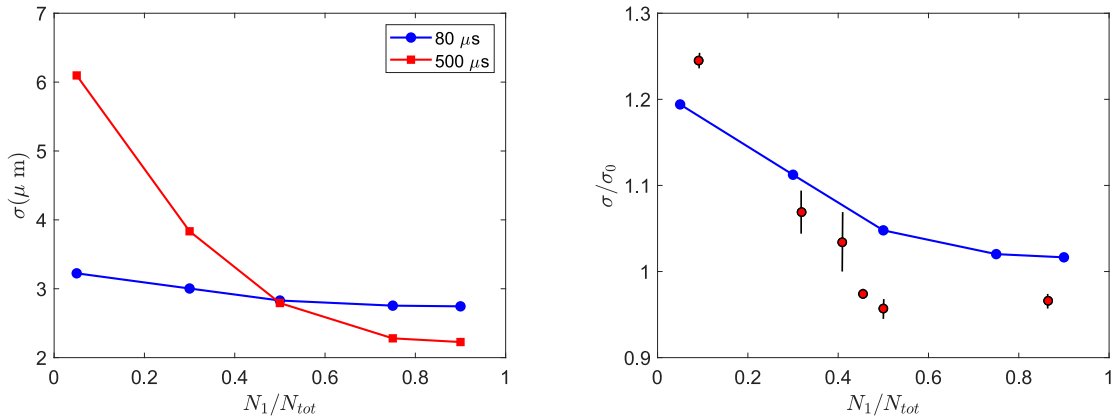

Figure 6.10: a) Simulated size after switching off the magnetic field in 500 μs (red) and 80 μs (blue) as a function of the population imbalance N_1/N_{tot}. b) Experimental data for the same quantity compared to the simulation performed, with $t_{switch} = 80$ μs.

80 μs after switching off the magnetic-field coils introduces a systematic error on the measured size of the atomic cloud, that depends on the fraction of atoms in the mixture. For the imbalance $N_1/N_{tot} \sim 0.4$ typical of the droplet, the two effects almost completely compensate each other and the error can be considered negligible in comparison to the statistical uncertainty.

6.2.4 Time evolution of the droplet

With the experimental methods explained in section (6.2.1) we could observe the time evolution of the mixture in free space. As one can see from Fig. (6.5a) when the system is in the droplet phase the density profile evolves differently from a quantum gases and the size remains constast during the time evolution. It is the first evidence of the self-bound

phase of an atomic mixture in free space. In Fig. (6.11a) the cloud remains in the droplet regime only in the first milliseconds of the evolution. The quick drop of the atom number makes the droplet move vertically in the phase diagram reported in Fig. (6.5). When it reaches the critical value the system undergoes a droplet-to-gas transition, where the cloud starts to expand and the atom number stabilizes to a constant value. The effects responsible for this significant losses of atoms are mainly two.
First, we observe a strong three-body ricombination phenomena [64, 65]. In the mixture there are four channels of losses due to three body recombination that depends on the species of the particles involved in the collision. However the rate of the losses in the state 1 are few orders of magnitude larger that the others. In addition to this, another phenomenon occurs, due to the fact the droplet forms with a fixed ratio N_1/N_2. It can bear only a small deviation from that value and any excess of atoms beyond this threshold is not bound to the droplet and expands away from it. The combination of these two effects leads to the behaviour that we observe in Fig. (6.11a).
In order to extract a value for the equilibrium size we selected the time interval where it does not change and we take the mean of all the values in the plateau. The critical atom number and the equilibrium ratio are instead measured as the mean of the value after the point of the liquid-to-gas transition. We repeat the measurements for different values of the magnetic field and finally we summarize the experimental results in the phase diagram show in Fig. (6.11). We compare our results with the predicted values. The agreement of the experimental data with the theory is very good for all the measured parameters.

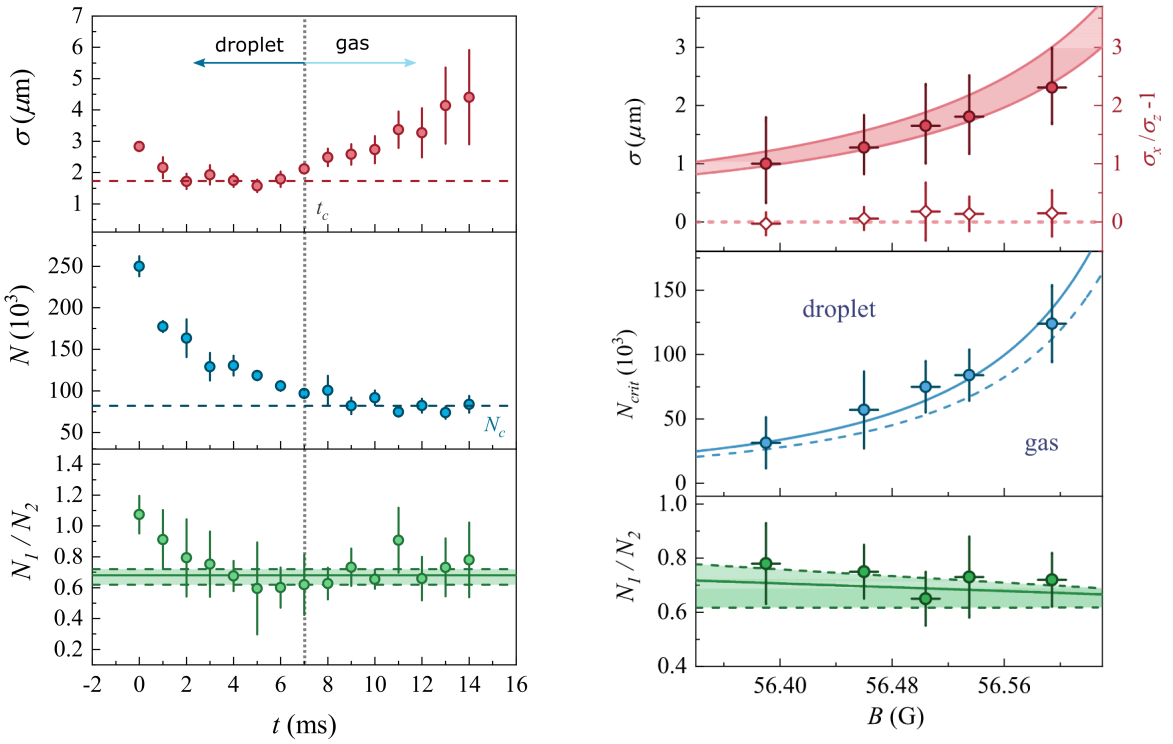

(a) (b)

Figure 6.11: a) Time evolution of the size σ, the total atom number N, and the ratio between the teo component N_1/N_2. The dashed lines are the average of σ on the plateau and the critical atom number N_c, measured as the average of N after the transition. The solid line represents the theoretical equilibrium value of the ratio and the green area between the dashed lines include the allowed deviations. The error bars represent the statistical uncertainty and correspond to the standard deviation. b) Measured values of the three parameters as a function of the magnetic field B. We also report the deviation of the aspect ratio from 1(diamonds). The colored areas in the graph at the top correspond to the theoretical prediction for $N_c \leq N \leq 2N_c$. The curves in the middle graph correspond to the predicted critical atom number for the metastable (dashed) and stable (solid) self-bound solutions. In the graph at the bottom, the theoretical predictions take into account the allowed deviations . The vertical error bars correspond to the statistical uncertainty and the horizzontal one is the uncertainty on the magnetic field.

6.3 Collisions between quantum droplets

The problem of classical droplet collisions has been investigated extensively both theoretically [66] and experimentally [67] in order to get information about the inner properties of the droplets, like for example the surface tension. Analogous studies have been carried out in the context of atomic nuclei to understand the dynamics of nuclear reactions and fission [68, 69, 70].
Once we have characterized the equilibrium properties of quantum droplets, In this section I report our experimental investigation about collisions between two droplets [71]. Due to the presence of three-body losses, the lifetime of the droplets is small but, since the time scales of the collision are smaller, we manage to characterize the collisional dynamics in different regimes. The study of the observed dynamics can be a good candidate to go further in the investigation of the liquid-like properties of quantum droplets.

6.3.1 Experimental realization of two colliding droplets

In order to obtain two separate droplets we create the BEC in the same beam's geometry shown in section (6.2.1) and then we ramp up an additional blue detuned laser beam (with a wavelength of 532 nm) that propagates vertically (Fig. (6.12)). The beam has an elliptical intensity profile with a large waist along y ($w_y \sim 1$ mm) and a tight one along x ($w_x \sim 15$ μm). It produces a repulsive barrier able to split the condensate in two parts along the x direction. In order to give the clouds a finite velocity we develope a procedure shown in Fig. (6.13). We switch off the horizzontal optical trap and the green barrier and switch on the levitating potential, while keeping the droplets for a variable time Δt in the vertical infrared beam that provides an harmonic confinement along the x-direction. By applying the same RF pulse used in the single droplet experiments, we can now create two separate droplets. After Δt we switch off this last beam and let the droplets collide in free space. Changing the intensity of the vertical infrared beam and Δt we can change the momentum provided to the droplets, i.e their relative velocity. Moreover, since three body losses are present, we can change the atom number changing the time when it occurs: it can be done simply changing the initial separation, i.e. the heigth of the central barrier.
In order to have an independent measurement of the relative velocity, where the trajectory followed by each droplet is not influenced by the presence of the other, we use the following strategy (sketched in Fig. 6.13 (b)-(c)). The basic idea is to repeat the sequence, but having one single droplet at a time. In order to load the BEC in a single well, we increase the height of the barrier and then we move its position along the x direction. The minimum of the right/left well is superimposed to that of the corresponding well in the previous configuration (left column of Fig. 6.13). In this way the double-well potential results to be strongly imbalanced and the BEC is loaded only in one of the two wells. At this point, we follow the same procedure as in the measurement with two droplets and the velocity provided to each will be the same as in the collision experiment.

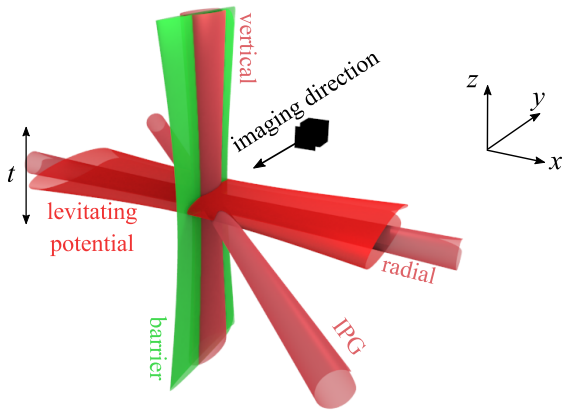

Figure 6.12: Schematic representation of the dipole optical traps plus the green barrier used to split the condensate.

6.3.2 Measurement of the critical velocity

We study the dynamics of the collision for different relative velocities and atom numbers. Depending on these parameters we observe different behaviours. Two examples are reported in Fig. (6.14) where we observe a clear merging and a passing through. In the first case the two droplets remain together in a single large droplet until the total atom number reaches the critical number and the cloud starts to expand. In the second case we observe that the two droplets pass through each other without significant perturbations. In order to probe a large range of parameters, and in particular to reach the regime where the droplet displays a liquid-like uniform bulk density (see Fig. 6.3), we can tune an additional parameter, i.e. the magnetic field B. The reported parameters $\tilde{v}$ and $\tilde{N}$ are riscaled adimensional quantities introduced in [50]. In this way we can change the value of $\tilde{N}$ only by tuning the magnetic field B, without changing the actual atom number N. We acquire a large set of measurements for different values of $\tilde{N}$ and $\tilde{v}$. Then we associate to each measurement the blue or red colour. Blue if the droplets separate after the collision; red if the droplets merge. Reporting the data in Fig. (6.15), we create a sort of phase diagram for the collisional dynamics. We observe that, for small values of $\tilde{N}$ ($\tilde{N} < 130$) the critical velocity increases for increasing $\tilde{N}$, while, for large values of $\tilde{N}$, it starts to decrease. It is a sign that there is a crossover between two different regimes, that I'll explain in more details in the next session.

6.3.3 Discussion on the results and comparison with theory

In order understand the observed behaviour in the physics of the collisions, we have collaborated with a theoretical group (A. Gallemi, A. Recati and S. Stringari, University of

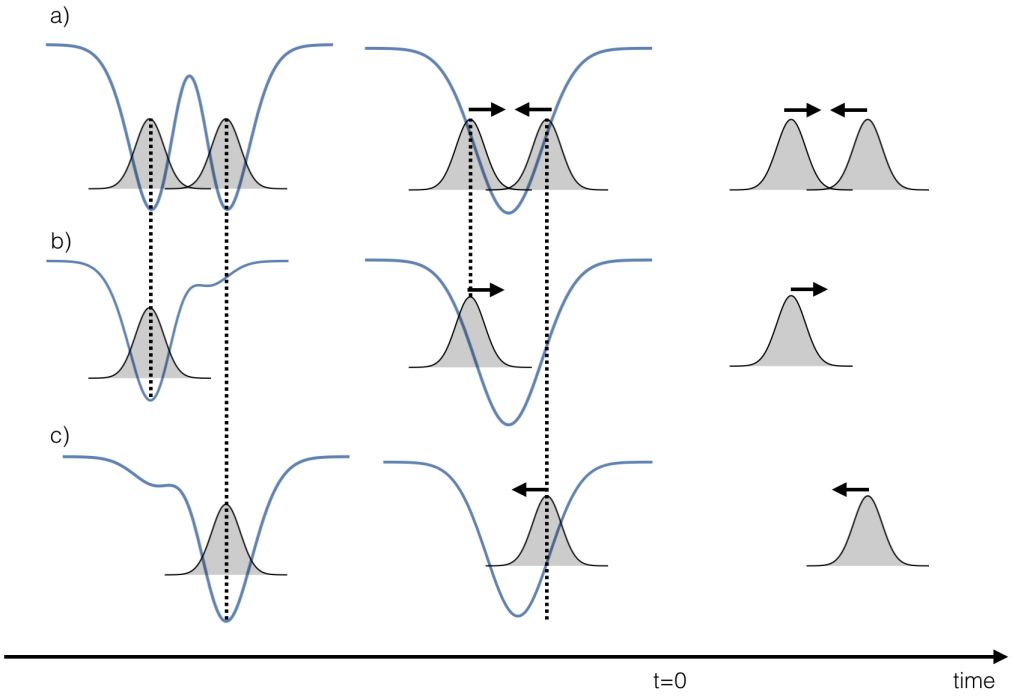

Figure 6.13: Scheme of the experimental sequence used to produce two colliding droplets (a) and to measure their relative velocity (b-c).

Trento) which has performed numerical simulations on a system analogous to the experiment. They simulate numerically the dynamics of the collision by means of a modified Gross-Pitaevskii equation (GPE) (see [27] for details). In order to distinguish between the merging and separation regimes, we compute the fraction of atoms that remain in the center of mass of the collision, that we identify as the merged fraction. A color plot of the merged fraction is reported in (Fig. (6.16). We observe a qualitative agreement with the experimental outcomes of Fig (6.15), but a quantitative difference in the position of the maximum of v_c, which is placed at $\tilde{N} \sim 200$.
In order to understand the origin of this discrepancy, we perform a second set of simulations including the effect of three-body losses (3BL) that, as shwon in the first session of measurements, are significantly strong in our droplets. The results are represented in Fig. (6.16) by the red diamonds and the blu squares, representing correspondently merging and separation. We observe that, while at small $\tilde{N}$ the position of v_c is basically unaffected by losses, at larger $\tilde{N}$, the three body losses shift the maximum to $\tilde{N} \sim 120$, in good agreement with the experimental results.
We can qualitatively understand the two opposite trends and the effect of losses, by drawing a simple argument. The possibility of forming a single droplet during the collision is related to the capability of the resulting merged droplet to absorb the excess kinetic energy $E_{kin} \sim v^2 \tilde{N}$. In the limit of large $\tilde{N}$, as discussed in section (6.1.3), the droplet shows a bulk density entering in a liquid-like regime. We can decompose its energy using

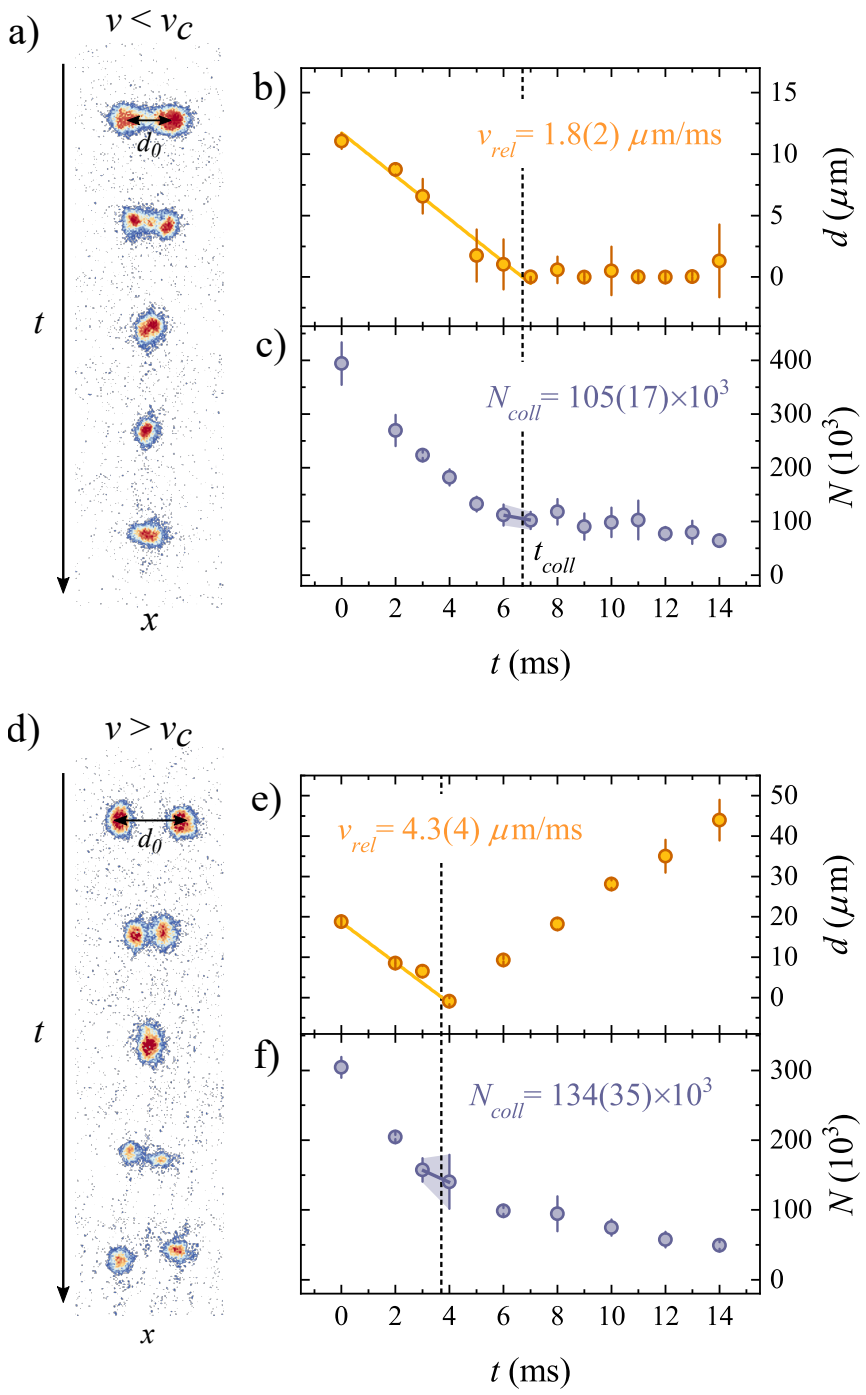

Figure 6.14: Examples of two collision measurements with different outcomes: merging in (a) and separation in (d). In b) and e) we report the corresponding time evolution of the distance d between the droplets and in c) and f) of the total atom number. A linear fit of $d(t)$ before the collision is used to measure the relative velocity and the time of collision. This measurements allows to deduce the atom number at the collision N_{coll}. All the error bars represent the statistical uncertainty and correspond to the standard deviation.

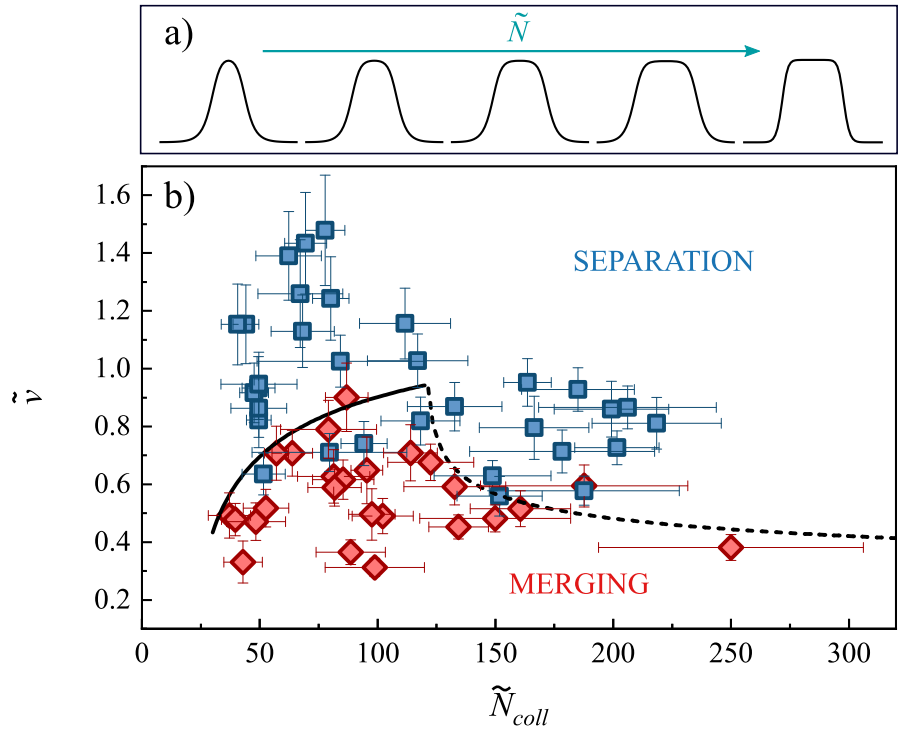

Figure 6.15: Experimental outcome of the collisions as a function of the rescaled velocity $\tilde{v}$ and atom number $\tilde{N}$. Reds corresponds to merging, blue to separation. In a) we draw the droplet wavefunction for increasing values of $\tilde{N}$, which highlights the crossover from compressible to incompressible droplets.

the so-called liquid-drop model [72]:

$$\tilde{E}_{drop} = \tilde{E}_B + \tilde{E}_S \tilde{N}^{-1/3} + \tilde{E}_C \tilde{N}^{-2/3} \tag{6.14}$$

where $\tilde{E}_B$, $\tilde{E}_S$ and $\tilde{E}_C$ are, respectively, the bulk, surface and curvature energy terms. The total energy of the colliding droplets is $2\tilde{E}(\tilde{N}/2)+\tilde{E}_{KIN}$, with $\tilde{N}$ the total atom number. If the outcome of the collision is a merging the final kinetic energy is zero, while the energy of the final state corresponds to the energy of a droplet with $\tilde{N}$ atoms plus some excitations of some surface modes descrived by a term $\tilde{E}_{EXC}$. Requiring energy conservation and considering that in expression (6.14) we can neglect the curvature energy and that the bulk energy (linear in $\tilde{N}$) remains constant, we have to compare the collisional kinetic energy with the surface energy variation and $\tilde{E}_{EXC}$. Imposing $\tilde{E}_{KIN} \sim \tilde{E}_S \tilde{N}^{-2/3}$ we get a critical velocity:

$$v_C \propto \tilde{N}^{-1/6} \tag{6.15}$$

that decreases for increasing $\tilde{N}$.
In the opposite case of small $\tilde{N}$, there is no distinction between the bulk and the surface and we expect that the relevant energy scale is the whole binding energy of the droplet. By imposing $\tilde{E}_{KIN} \sim \tilde{E}_{drop}$ we get a critical velocity:

$$v_C \propto \sqrt{2|E_{drop}|\tilde{N}} \tag{6.16}$$

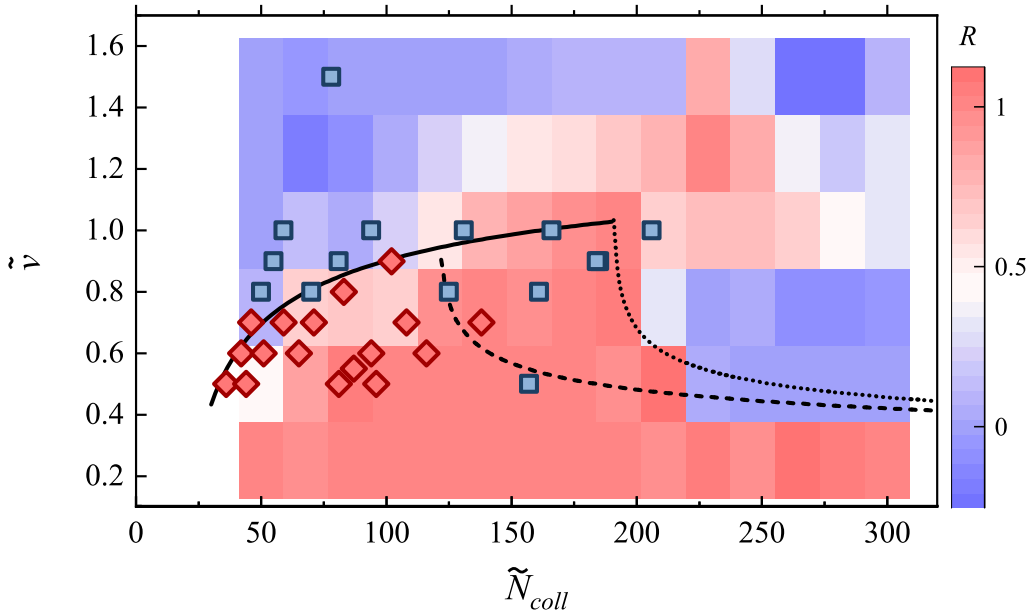

Figure 6.16: Results of simulations in the ideal case without losses. The color plot represents the merging fraction introduced in the text, while the data points represent merging (red diamonds) or separation (blue squares) as otucome of numerical simulations with 3BL. The solid lines represent the expected trend $v_C \propto \sqrt{2|E_{drop}|\tilde{N}}$, while the dotted line correpond to $v_C \propto \tilde{N}^{-1/6}$, which are the two predicted scaling in the different regimes of $\tilde{N}$. The dashed lines correspond to the same $\tilde{N}^{1/6}$ scaling, but in this case it is simply used as a guide to the eye

These two trends of the critical velocity are represented in Fig. (6.16) by the dotted and continous lines and they are compared with the experimental data. We find that these simple energetic considerations qualitatively justify the observed behavior.
In conclusion, using binary collisions as a probe of the dynamical properties of mixture droplets, we have found the first evidences of a crossover from compressible to incompressible regimes driven by $\tilde{N}$. This is highlighted by the different scaling of $\tilde{v}_C$ which is well justified by simple energetic considerations. The results can pave the way to the investigation of phenomena related to the superfluidity of quantum droplets and to its peculiar energy spectrum.

Appendix A

Bloch oscillations in presence of an additional harmonic potential

In this appendix I would like to discuss in more detail the problem of non-interacting atoms in an optical lattice that are subjected not only to an external force, but also to a weak harmonic potential.
In litterature, the motion of atoms in an additional harmonic potential has already been discussed in different regimes [73, 74], but in all of these works the starting condensate is spread over many lattice sites. In this section, I investigate numerically the effect of an additional harmonic potential on a condensate that is initially loaded in a single site, like in our experiment. The results can be interesting in order to check the effect of some inhomogeneities of the force.
The potential felt by the atoms is:

$$V(x) = V_{OL}(x) + Fx + \frac{1}{2}m\omega_{add}^2 x^2 \tag{A.1}$$

The lattice spacing of the optical lattice is 10 μm and, for potassium 39, the harmonic oscillator length $a_{ho} = \sqrt{\hbar/m\omega_{add}}$ for $\omega_{add} = 2\pi\times1$ Hz is 16 μm. In presence of a force F the Bloch frequency is $\nu_B = Fd/\hbar$. In particular, in analogy with the range of parameters that we explored experimentally, I will consider the case of a BL with a depth of 70 nK that provides a tunneling rate of 1.5 Hz.
I investigate the coherent tunneling between neighbouring sites with a variable ω_{add}. I numerically solve the time dependent Schrödinger equation, reproducing the same procedure that we perform experimentally, and I record the populations in the starting site (labbelled by $i = 0$) and in the next neighbours (labelled by $i = \pm1$). Examples of the time evolution of the sum of the populations $N \pm 1$ for different ω_{add} in the case of $\nu_B = 3$ Hz are shown in Fig. (A.1a). For $\omega_{add} \neq 0$ we observe the appearance of a beating between two frequencies and the curves are no longer described by a single sinusoidal function. In order to separate the different components, I calculate the Fourier trasformation of the time traces (see Fig. (A.1b)). For small ω_{add} a clear beating is highlighted by the presence of peaks around half of the sum and the difference of ν_B and $\omega_{add}/2\pi$ (or multiples of these

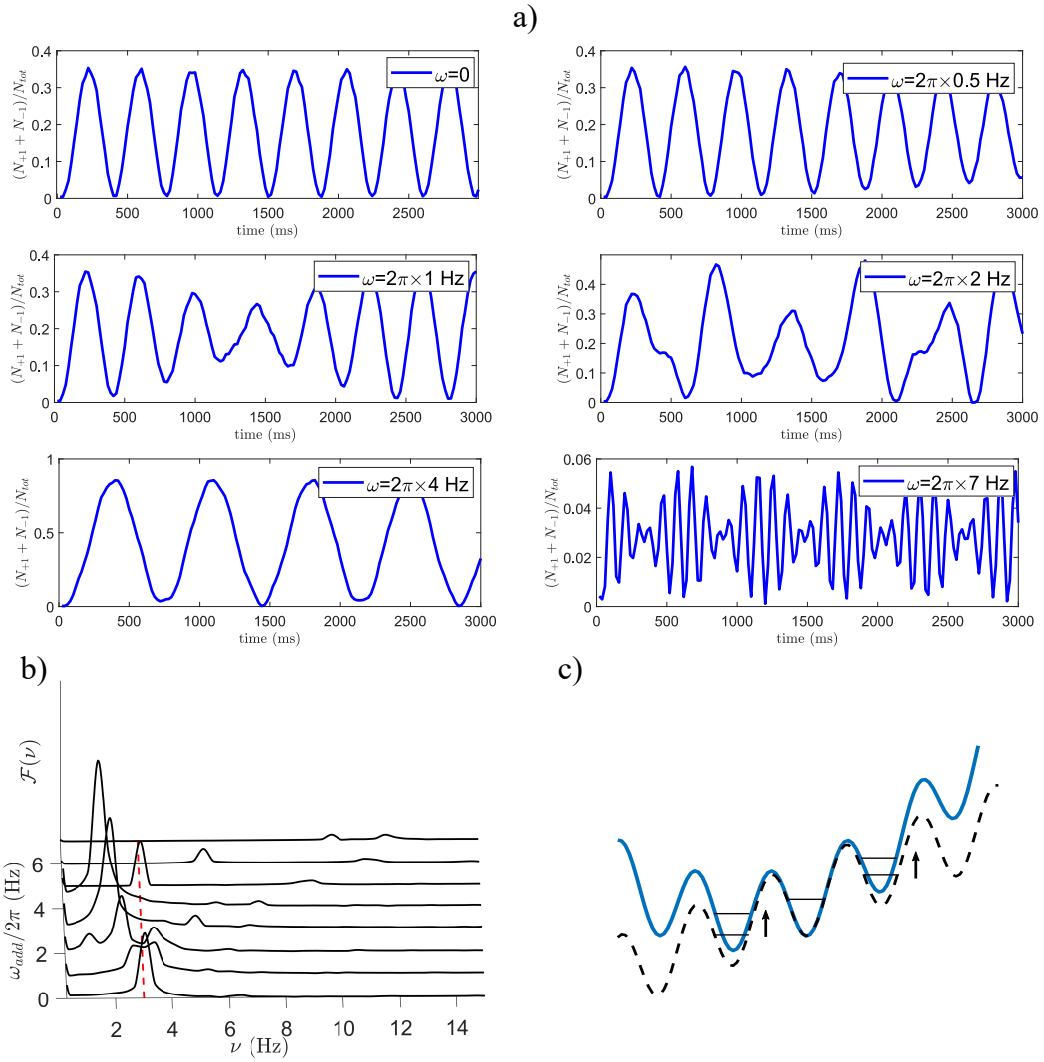

Figure A.1: a) Some examples of the time evolution of the fractional populations in the site ± 1 for the case $\nu_B = 3$ Hz in presence of an additional harmonic potential. b) Fourier spectra as a function of ω_{add} show the appearance of spourious components and the deviation of the largest component respect to ν_B. c) Schematic representation of the effect of an harmonic potential on the tilted lattice.

frequencies). In order to investigate more quantitatively the observed behaviour, I report respectively the value of the largest frequency component ν_{max} in Fig. (A.2a) and the amplitude of the oscillation in Fig. (A.2b) (in terms of fractional populations) extracted by each time trace as a function of ω_{add}. If there is a beating-note, the amplitude of the oscillation is not constant, therefore I report the mean value A_{mean}. I show the numerical results for 3 different values of ν_B.

For a curvature smaller than 4 Hz we observe a slightly variation of ν_{max}. The presence of the curvature shifts the energy levels near the starting site (A.1c). Depending on the side, the curvature increases or decreases the energy difference between them and consequently the tunneling probability changes. From Fig. (A.2a) we observe that the net effect is a decreasing of ν_{max} with a correspondent growing up of the amplitude. For values larger than 4 Hz the harmonic oscillator length starts to become smaller than the

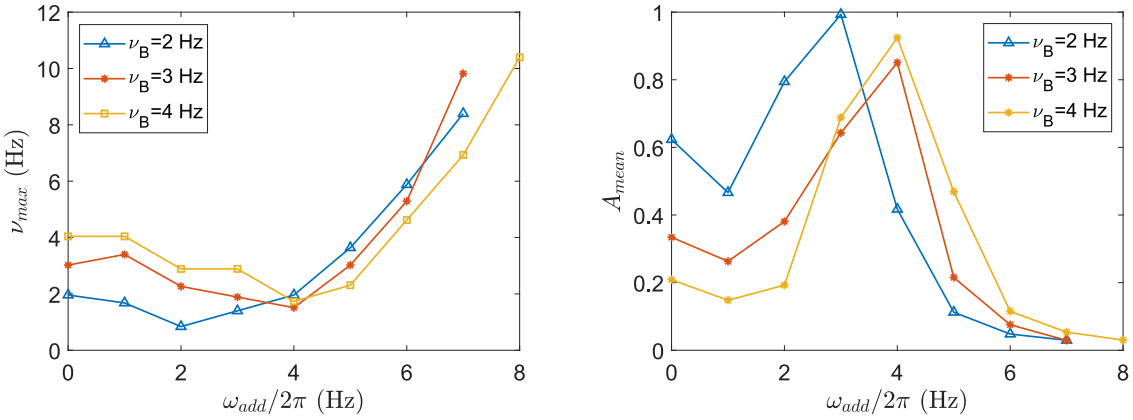

(a) (b)

Figure A.2: a) Numerical prediction of ν_{max} of the frequency respect to the Bloch frequency ν_B as a function of the force for difference values of $\omega_{add}/2\pi$. In (b) I report the relative amplitudes.

lattice spacing and the wavefunction is more and more confined in the starting well. The Bloch dynamics dissappears and we observe a quick drop of the amplitude togheter with a fast increasing of ν_{max}. The measured frequency no longer depends on the applied force F and the dynamics is dominated by ω_{add} and the single site trapping frequency that is of the order of 20-30 Hz.

In the experimental results shown in Chapter 3 we observe a linear behaviour of the frequency as a function of the force and amplitudes that go from 0.3 to 0.5. In conclusion, the experimental data are in agreement with the numerical predictions for $\omega_{add}/2\pi < 2$ Hz, that is comparable with the expected value related to the curvature of the optical potential.

Bibliography

[1] Alexander D Cronin, Jörg Schmiedmayer, and David E Pritchard. Optics and interferometry with atoms and molecules. *Reviews of Modern Physics*, 81(3):1051, 2009.

[2] Achim Peters, Keng Yeow Chung, and Steven Chu. Measurement of gravitational acceleration by dropping atoms. *Nature*, 400(6747):849, 1999.

[3] Jeffrey B Fixler, GT Foster, JM McGuirk, and MA Kasevich. Atom interferometer measurement of the newtonian constant of gravity. *Science*, 315(5808):74–77, 2007.

[4] G Rosi, F Sorrentino, L Cacciapuoti, M Prevedelli, and GM Tino. Precision measurement of the newtonian gravitational constant using cold atoms. *Nature*, 510(7506):518, 2014.

[5] Naceur Gaaloul, H Ahlers, TA Schulze, Y Singh, ST Seidel, W Herr, W Ertmer, E Rasel, et al. Quantum tests of the equivalence principle with atom interferometry. *Acta Astronautica*, 67(9-10):1059–1062, 2010.

[6] Chris Overstreet, Peter Asenbaum, Tim Kovachy, Remy Notermans, Jason M Hogan, and Mark A Kasevich. Effective inertial frame in an atom interferometric test of the equivalence principle. *Physical review letters*, 120(18):183604, 2018.

[7] Andrea Bertoldi, Kai Bongs, Philippe Bouyer, Oliver Buchmueller, Benjamin Canuel, Laurentiu-Ioan Caramete, Maria Luisa Chiofalo, Jonathon Coleman, Albert De Roeck, John Ellis, et al. Aedge: Atomic experiment for dark matter and gravity exploration in space. *arXiv preprint arXiv:1908.00802*, 2019.

[8] T Mazzoni, X Zhang, R Del Aguila, L Salvi, N Poli, and GM Tino. Large-momentum-transfer bragg interferometer with strontium atoms. *Physical Review A*, 92(5):053619, 2015.

[9] Holger Ahlers, H Müntinga, A Wenzlawski, M Krutzik, G Tackmann, S Abend, N Gaaloul, E Giese, A Roura, R Kuhl, et al. Double bragg interferometry. *Physical review letters*, 116(17):173601, 2016.

[10] MR Andrews, CG Townsend, H-J Miesner, DS Durfee, DM Kurn, and W Ketterle. Observation of interference between two bose condensates. *Science*, 275(5300):637–641, 1997.

[11] Tarik Berrada, Sandrine van Frank, Robert Bücker, Thorsten Schumm, J-F Schaff, and Jörg Schmiedmayer. Integrated mach–zehnder interferometer for bose–einstein condensates. *Nature communications*, 4:2077, 2013.

[12] Marco Fattori, B Deissler, C D'ERRICO, Mattia Jona-Lasinio, M Modugno, G Roati, L Santos, A Simoni, M Zaccanti, M Inguscio, et al. Atom interferometry with a weakly interacting bose-einstein condensate. In *Pushing The Frontiers Of Atomic Physics*, pages 251–262. World Scientific, 2009.

[13] G Spagnolli, G Semeghini, L Masi, G Ferioli, A Trenkwalder, S Coop, M Landini, L Pezze, G Modugno, M Inguscio, et al. Crossing over from attractive to repulsive interactions in a tunneling bosonic josephson junction. *Physical review letters*, 118(23):230403, 2017.

[14] Mauro Antezza, Lev P Pitaevskii, Sandro Stringari, and Vitaly B Svetovoy. Casimir-lifshitz force out of thermal equilibrium and asymptotic nonadditivity. *Physical review letters*, 97(22):223203, 2006.

[15] Markus Greiner, Olaf Mandel, Theodor W Hänsch, and Immanuel Bloch. Collapse and revival of the matter wave field of a bose–einstein condensate. *Nature*, 419(6902):51, 2002.

[16] Michael Albiez, Rudolf Gati, Jonas Fölling, Stefan Hunsmann, Matteo Cristiani, and Markus K Oberthaler. Direct observation of tunneling and nonlinear self-trapping in a single bosonic josephson junction. *Physical review letters*, 95(1):010402, 2005.

[17] Tilman Zibold, Eike Nicklas, Christian Gross, and Markus K Oberthaler. Classical bifurcation at the transition from rabi to josephson dynamics. *Physical review letters*, 105(20):204101, 2010.

[18] A Trenkwalder, G Spagnolli, G Semeghini, S Coop, M Landini, P Castilho, L Pezze, G Modugno, M Inguscio, A Smerzi, et al. Quantum phase transitions with parity-symmetry breaking and hysteresis. *Nature physics*, 12(9):826, 2016.

[19] C Bodet, J Esteve, MK Oberthaler, and T Gasenzer. Two-mode bose gas: Beyond classical squeezing. *Physical Review A*, 81(6):063605, 2010.

[20] Sandrine van Frank, Antonio Negretti, Tarik Berrada, Robert Bücker, Simone Montangero, J-F Schaff, Thorsten Schumm, Tommaso Calarco, and Jörg Schmiedmayer. Interferometry with non-classical motional states of a bose–einstein condensate. *Nature communications*, 5:4009, 2014.

[21] L Pezzé, LA Collins, A Smerzi, GP Berman, and AR Bishop. Sub-shot-noise phase sensitivity with a bose-einstein condensate mach-zehnder interferometer. *Physical Review A*, 72(4):043612, 2005.

[22] Luca Pezzè, Augusto Smerzi, Markus K Oberthaler, Roman Schmied, and Philipp Treutlein. Quantum metrology with nonclassical states of atomic ensembles. *Reviews of Modern Physics*, 90(3):035005, 2018.

[23] Philipp M Preiss, Ruichao Ma, M Eric Tai, Alexander Lukin, Matthew Rispoli, Philip Zupancic, Yoav Lahini, Rajibul Islam, and Markus Greiner. Strongly correlated quantum walks in optical lattices. *Science*, 347(6227):1229–1233, 2015.

[24] G Ferrari, N Poli, F Sorrentino, and GM Tino. Long-lived bloch oscillations with bosonic sr atoms and application to gravity measurement at the micrometer scale. *Physical Review Letters*, 97(6):060402, 2006.

[25] N Poli, F-Y Wang, MG Tarallo, A Alberti, M Prevedelli, and GM Tino. Precision measurement of gravity with cold atoms in an optical lattice and comparison with a classical gravimeter. *Physical review letters*, 106(3):038501, 2011.

[26] G Semeghini, G Ferioli, L Masi, C Mazzinghi, L Wolswijk, F Minardi, M Modugno, G Modugno, M Inguscio, and M Fattori. Self-bound quantum droplets of atomic mixtures in free space. *Physical review letters*, 120(23):235301, 2018.

[27] Giovanni Ferioli, Giulia Semeghini, Leonardo Masi, Giovanni Giusti, Giovanni Modugno, Massimo Inguscio, Albert Gallemí, Alessio Recati, and Marco Fattori. Collisions of self-bound quantum droplets. *Physical review letters*, 122(9):090401, 2019.

[28] Rudolf Grimm, Matthias Weidemüller, and Yurii B Ovchinnikov. Optical dipole traps for neutral atoms. In *Advances in atomic, molecular, and optical physics*, volume 42, pages 95–170. Elsevier, 2000.

[29] NW Ashcroft and ND Mermin. Solid state physics int. ed. *Holt-Saunders, Philadelphia*, 16, 1976.

[30] Oliver Morsch and Markus Oberthaler. Dynamics of bose-einstein condensates in optical lattices. *Reviews of modern physics*, 78(1):179, 2006.

[31] Clarence Zener. Non-adiabatic crossing of energy levels. *Proceedings of the Royal Society of London. Series A, Containing Papers of a Mathematical and Physical Character*, 137(833):696–702, 1932.

[32] Maxime Ben Dahan, Ekkehard Peik, Jakob Reichel, Yvan Castin, and Christophe Salomon. Bloch oscillations of atoms in an optical potential. *Physical Review Letters*, 76(24):4508, 1996.

[33] Zachary A Geiger, Kurt M Fujiwara, Kevin Singh, Ruwan Senaratne, Shankari V Rajagopal, Mikhail Lipatov, Toshihiko Shimasaki, Rodislav Driben, Vladimir V Konotop, Torsten Meier, et al. Observation and uses of position-space bloch oscillations in an ultracold gas. *Physical review letters*, 120(21):213201, 2018.

[34] Timo Hartmann, F Keck, HJ Korsch, and S Mossmann. Dynamics of bloch oscillations. *New Journal of Physics*, 6(1):2, 2004.

[35] Andrey R Kolovsky and Hans Jürgen Korsch. Bloch oscillations of cold atoms in optical lattices. *International Journal of Modern Physics B*, 18(09):1235–1260, 2004.

[36] J Zapata, AM Guzmán, MG Moore, and P Meystre. Gravity-induced wannier-stark ladder in an optical lattice. *Physical Review A*, 63(2):023607, 2001.

[37] A Alberti, VV Ivanov, GM Tino, and G Ferrari. Engineering the quantum transport of atomic wavefunctions over macroscopic distances. *Nature Physics*, 5(8):547, 2009.

[38] Elmar Haller, Russell Hart, Manfred J Mark, Johann G Danzl, Lukas Reichsöllner, and Hanns-Christoph Nägerl. Inducing transport in a dissipation-free lattice with super bloch oscillations. *Physical review letters*, 104(20):200403, 2010.

[39] Manuele Landini. *A tunable Bose-Einstein condensate for quantum interferometry*. PhD thesis, University of Trento, 2012.

[40] Manuele Landini, Sanjukta Roy, Giacomo Roati, Andrea Simoni, Massimo Inguscio, Giovanni Modugno, and Marco Fattori. Direct evaporative cooling of 39 k atoms to bose-einstein condensation. *Physical Review A*, 86(3):033421, 2012.

[41] Giacomo Roati, Matteo Zaccanti, C dErrico, Jacopo Catani, Michele Modugno, Andrea Simoni, Massimo Inguscio, and G Modugno. K 39 bose-einstein condensate with tunable interactions. *Physical review letters*, 99(1):010403, 2007.

[42] Chiara d'Errico, Matteo Zaccanti, Marco Fattori, Giacomo Roati, Massimo Inguscio, Giovanni Modugno, and Andrea Simoni. Feshbach resonances in ultracold 39k. *New Journal of physics*, 9(7):223, 2007.

[43] RWP Drever, John L Hall, FV Kowalski, J_ Hough, GM Ford, AJ Munley, and H Ward. Laser phase and frequency stabilization using an optical resonator. *Applied Physics B*, 31(2):97–105, 1983.

[44] Eric D Black. An introduction to pound–drever–hall laser frequency stabilization. *American journal of physics*, 69(1):79–87, 2001.

[45] James I Thorpe, K Numata, and J Livas. Laser frequency stabilization and control through offset sideband locking to optical cavities. *Optics express*, 16(20):15980–15990, 2008.

[46] Gianmaria Milani, Benjamin Rauf, Piero Barbieri, Filippo Bregolin, Marco Pizzocaro, Pierre Thoumany, Filippo Levi, and Davide Calonico. Multiple wavelength stabilization on a single optical cavity using the offset sideband locking technique. *Optics letters*, 42(10):1970–1973, 2017.

[47] Gianni Di Domenico, Stéphane Schilt, and Pierre Thomann. Simple approach to the relation between laser frequency noise and laser line shape. *Applied optics*, 49(25):4801–4807, 2010.

[48] Andrea Trombettoni and Augusto Smerzi. Discrete solitons and breathers with dilute bose-einstein condensates. *Physical Review Letters*, 86(11):2353, 2001.

[49] T Bergeman, Gidon Erez, and Harold J Metcalf. Magnetostatic trapping fields for neutral atoms. *Physical Review A*, 35(4):1535, 1987.

[50] DS Petrov. Quantum mechanical stabilization of a collapsing bose-bose mixture. *Physical review letters*, 115(15):155302, 2015.

[51] L Chomaz, S Baier, D Petter, MJ Mark, F Wächtler, Luis Santos, and F Ferlaino. Quantum-fluctuation-driven crossover from a dilute bose-einstein condensate to a macrodroplet in a dipolar quantum fluid. *Physical Review X*, 6(4):041039, 2016.

[52] Matthias Schmitt, Matthias Wenzel, Fabian Böttcher, Igor Ferrier-Barbut, and Tilman Pfau. Self-bound droplets of a dilute magnetic quantum liquid. *Nature*, 539(7628):259, 2016.

[53] CR Cabrera, L Tanzi, J Sanz, B Naylor, P Thomas, P Cheiney, and L Tarruell. Quantum liquid droplets in a mixture of bose-einstein condensates. *Science*, 359(6373):301–304, 2018.

[54] P Cheiney, CR Cabrera, J Sanz, B Naylor, L Tanzi, and L Tarruell. Bright soliton to quantum droplet transition in a mixture of bose-einstein condensates. *Physical review letters*, 120(13):135301, 2018.

[55] TD Lee and CN Yang. Many-body problem in quantum mechanics and quantum statistical mechanics. *Physical Review*, 105(3):1119, 1957.

[56] Franco Dalfovo, Stefano Giorgini, and P Lev. Pitaevskii, and s. stringari. *Rev. Mod. Phys*, 71:463, 1999.

[57] Alexander L Fetter and John Dirk Walecka. *Quantum theory of many-particle systems*. Courier Corporation, 2012.

[58] Nir Navon, Swann Piatecki, Kenneth Günter, Benno Rem, Trong Canh Nguyen, Frédéric Chevy, Werner Krauth, and Christophe Salomon. Dynamics and thermodynamics of the low-temperature strongly interacting bose gas. *Physical review letters*, 107(13):135301, 2011.

[59] Shina Tan. Energetics of a strongly correlated fermi gas. *Annals of Physics*, 323(12):2952–2970, 2008.

[60] Eric Braaten, Daekyoung Kang, and Lucas Platter. Universal relations for identical bosons from three-body physics. *Physical review letters*, 106(15):153005, 2011.

[61] RJ Wild, P Makotyn, JM Pino, EA Cornell, and DS Jin. Measurements of tans contact in an atomic bose-einstein condensate. *Physical review letters*, 108(14):145305, 2012.

[62] Richard J Fletcher, Raphael Lopes, Jay Man, Nir Navon, Robert P Smith, Martin W Zwierlein, and Zoran Hadzibabic. Two-and three-body contacts in the unitary bose gas. *Science*, 355(6323):377–380, 2017.

[63] Giovanni Ferioli. *Self-bound quantum droplets in Bose-Bose mixture*. PhD thesis, University of Florence, 2012.

[64] Matteo Zaccanti, Benjamin Deissler, Chiara DErrico, Marco Fattori, Mattia Jona-Lasinio, Stefan Müller, Giacomo Roati, Massimo Inguscio, and Giovanni Modugno. Observation of an efimov spectrum in an atomic system. *Nature Physics*, 5(8):586, 2009.

[65] Tino Weber, Jens Herbig, Michael Mark, Hanns-Christoph Nägerl, and Rudolf Grimm. Three-body recombination at large scattering lengths in an ultracold atomic gas. *Physical review letters*, 91(12):123201, 2003.

[66] J Qian and Chung King Law. Regimes of coalescence and separation in droplet collision. *Journal of Fluid Mechanics*, 331:59–80, 1997.

[67] Melissa Orme. Experiments on droplet collisions, bounce, coalescence and disruption. *Progress in Energy and Combustion Science*, 23(1):65–79, 1997.

[68] AN Andreyev, Katsuhisa Nishio, and Karl-Heinz Schmidt. Nuclear fission: a review of experimental advances and phenomenology. *Reports on Progress in Physics*, 81(1):016301, 2017.

[69] Piotr Magierski, Kazuyuki Sekizawa, and Gabriel Wlazłowski. Novel role of superfluidity in low-energy nuclear reactions. *Physical review letters*, 119(4):042501, 2017.

[70] Aurel Bulgac and Shi Jin. Dynamics of fragmented condensates and macroscopic entanglement. *Physical review letters*, 119(5):052501, 2017.

[71] GE Astrakharchik and Boris A Malomed. Dynamics of one-dimensional quantum droplets. *Physical Review A*, 98(1):013631, 2018.

[72] Ivana Bešlić, L Vranješ Markić, and Jordi Boronat. Quantum monte carlo study of large spin-polarized tritium clusters. *The Journal of chemical physics*, 131(24):244506, 2009.

[73] M Krämer, L Pitaevskii, and S Stringari. Macroscopic dynamics of a trapped bose-einstein condensate in the presence of 1d and 2d optical lattices. *Physical review letters*, 88(18):180404, 2002.

[74] Th Anker, M Albiez, R Gati, S Hunsmann, B Eiermann, Andrea Trombettoni, and MK Oberthaler. Nonlinear self-trapping of matter waves in periodic potentials. *Physical review letters*, 94(2):020403, 2005.